General Disclaimer

One or more of the Following Statements may affect this Document

- This document has been reproduced from the best copy furnished by the organizational source. It is being released in the interest of making available as much information as possible.

- This document may contain data, which exceeds the sheet parameters. It was furnished in this condition by the organizational source and is the best copy available.

- This document may contain tone-on-tone or color graphs, charts and/or pictures, which have been reproduced in black and white.

- This document is paginated as submitted by the original source.

- Portions of this document are not fully legible due to the historical nature of some of the material. However, it is the best reproduction available from the original submission.

Aerodynamic Characteristics of a Large-Scale Semispan Model With a Swept Wing and an Augmented Jet Flap With Hypermixing Nozzles

Thomas N. Aiken, Michael D. Falarski, and David G. Koenig

July 1979

NASA

National Aeronautics and
Space Administration

NOTATION

A_3/A_2	ratio of diffuser exit area to augmentor throat area
BLC	boundary layer control
c	wing chord (streamwise), m (ft)
$\bar{c}$	mean aerodynamic chord, m (ft)
C_D	drag coefficient, drag/qS
C_J	augmentor nozzle thrust coefficient, actual nozzle thrust/qS
C_{J_I}	isentropic augmentor nozzle thrust coefficient, isentropic nozzle thrust/qS
C_L	lift coefficient, lift/qS
$C_{L_{aero}}$	aerodynamic lift coefficient, lift minus reaction lift/qS (see data reduction section)
C_M	pitching moment coefficient, pitching moment/$qS\bar{c}$
C_{μ_A}	aileron BLC isentropic blowing coefficient, isentropic thrust/qS
C_{μ_D}	door BLC isentropic blowing coefficient, isentropic thrust/qS
$C_{\mu_{EP}}$	end plate BLC isentropic blowing coefficient, isentropic thrust/qS
C_{μ_F}	flap BLC isentropic blowing coefficient, isentropic thrust/qS
C_{μ_I}	inlet BLC isentropic blowing coefficient, isentropic thrust/qS
$C_{\mu_{LE}}$	leading edge BLC isentropic blowing coefficient, isentropic thrust/qS
$C_{\mu_{UF}}$	upper flap BLC isentropic blowing coefficient, isentropic thrust/qS

iii

m_s/m_p	mass flow ratio, augmentor secondary mass flow/augmentor nozzle mass flow
NAR	nozzle aspect ratio, hypermixing segment length/gap
NPR	nozzle pressure ratio, total pressure/freestream static pressure
q	freestream dynamic pressure, N/sq m (lb/sq ft)
S	wing planform area, sq m (sq ft)
t	airfoil thickness, m (ft)
V_{J_I}	isentropic jet velocity, expanded to freestream static pressure, m/sec (ft/sec)
V_∞	freestream velocity, m/sec (ft/sec)
α	angle of attack, referenced to fuselage datum, deg
ϕ_G	gross augmentation ratio, actual augmentor static thrust/actual nozzle thrust
δ_a	aileron deflection angle, referenced to wing chord plane, training edge down, deg
δ_f	flap deflection angle (see figure 2(e)), deg
δ_s	slat deflection angle (see figure 2(g)), deg

Subscripts

a,A	aileron, aileron BLC
D	door BLC
EP	end plate BLC
f,F	flap, flap BLC
G	gross
I	inlet BLC, isentropic
LE	leading edge BLC

iv

s	slat
u	uncorrected
!F	upper flap BLC
∞	freestream

AERODYNAMIC CHARACTERISTICS OF A LARGE-SCALE SEMISPAN MODEL WITH A SWEPT WING AND AN AUGMENTED JET FLAP WITH HYPERMIXING NOZZLES

Thomas N. Aiken, Michael D. Falarski, and David G. Koenig

Ames Research Center

SUMMARY

This report presents results and analysis from an investigation of the aerodynamic characteristics of the augmentor wing concept with hypermixing primary nozzles. The investigation was made using a large-scale semispan model in the Ames 40- by 80-Foot Wind Tunnel and Static Test Facility.

The trailing edge, augmentor flap system occupied 65% of the span and consisted of two, fixed pivot flaps. The nozzle system consisted of hypermixing, lobe primary nozzles, and BLC slot nozzles at the forward inlet, both sides and ends of the throat and at the aft flap. The entire wing leading edge was fitted with a 10% chord slat and a blowing slot. Outboard of the flap was a blown aileron.

The model was tested statically and at forward speed. Primary parameters and their ranges included angle of attack from -12 to 32 degrees, flap angles of 20, 30, 45, 60 and 70 degrees deflection and diffuser area ratios from 1.16 to 2.22. Thrust coefficients ranged from 0 to 2.73 while nozzle pressure ratios varied from 1.0 to 2.34. Reynolds number per foot varied from 0 to 1.4 million.

Analysis of the data indicated a maximum static, gross augmentation of 1.53 at a flap angle of 45 degrees. Analysis also indicated that the configuration was an efficient powered lift device and that

the net thrust was comparable with augmentor wings of similar static performance. Performance at forward speed was best at a diffuser area ratio of 1.37.

INTRODUCTION

The augmentor wing concept is being studied as a means of attaining STOL performance in a turbofan powered aircraft. Reference 1 shows the characteristics of an augmentor wing configuration with an approximate, gross augmentation of 1.3.

Reference 2 indicates the potential of gross augmentations above 2.0 by using hypermixing, lobe nozzles and extensive boundary layer control (BLC) nozzles. This technology was applied to a STOL augmentor design and the results of a model test reported in reference 3. The results indicated that a gross augmentation ratio of 1.7 was attainable. To investigate this configuration on a more realistic model, a trailing-edge augmentor system was installed on an Ames large-scale semispan model. The model was then tested statically at the Ames Static Test Facility and at forward speed in the Ames 40- by 80-Foot Wind Tunnel.

The tests were performed in cooperation with the Bell Aerospace Company and the Flight Dynamics Laboratory of the Department of the Air Force.

MODEL AND APPARATUS

Figures 1(a) through 1(c) show the model installed in the Ames 40- by 80-Foot Wind Tunnel.

Basic Model

Table I gives geometric data for the model. Sketches of the model are shown in figure 2. A three-view of the model installed in the wind tunnel is shown in figure 2(a). The reflection plane and fairing are isolated from the wing and half-fuselage which are on the wind tunnel balance. Figure 2(b) shows the general arrangement of the static test. During the static test, the wing alone was attached to a pendulum type platform which was restrained by 3 single-axis load cells, 2 in the lift direction and 1 in the drag direction. A typical wing section is shown in figure 2(c).

Blowing System

The model was supplied with compressed air from a remote, J-85 Viper turbocompressor unit shown schematically in figure 2(d). In both the static and wind tunnel test, the compressed air was ducted approximately 30 meters to a bellows-type isolation gland and into the hollow wing spar shown in figure 2(c).

3

Figure 2(e) shows a typical augmentor section. The dimensions of the various nozzles are given in Table II. The hypermixing lobe nozzles are shown in detail in figure 2(f). The height of the lobes varies from 14 centimeters (5.5 inches) at the root to 7.6 centimeters (3 inches) at the augmentor tip. The nozzles are spaced 2.5 inches apart.

The flap supply tube shown in figure 2(e) was end-fed with compressed air from the ducting just below the wing root. The tube was equipped with a shut off valve. The door, flap, or upper flap BLC slots could be sealed with a foam rubber gasket.

Both ends of the augmentor were equipped with fixed end plates that sealed the ends of the door-flap combination at all flap angles. Also, both end plates were equipped with blowing slots at the augmentor throat.

The wing was equipped with a full-span leading edge slat and blowing slot. Figure 2(g) shows their details. Figure 2(h) shows details of the blown aileron. Both the leading edge blowing slot and the aileron blowing nozzles were supplied with compressed air through the hollow wing spar.

Instrumentation

The wing forward of the 50% chord was equipped with surface pressure taps at 27, 57, and 88 percent semispan. Augmentor exit rakes were located at 19, 33, 47, 59, and 77 percent semispan. The

4

rakes consisted of from 6 to 10 pitot-static probes. The blowing system internal pressure and temperature were measured at several locations; 5 places on the augmentor, 2 places in the flap supply tube, 3 places in the leading edge, and 2 places in the aileron. Mass flow measuring stations were located in the duct from the turbo-compressor and the flap supply tube. The stations measured static and total pressure and temperature and were calibrated with conical nozzles prior to testing.

TESTS

The tare force of the isolation gland was calibrated in the lift and drag directions by testing a conical nozzle in opposite directions and assuming that the difference was the tare. The augmentor nozzles were calibrated by removing the door, flap, and flap supply tube and measuring the force at nozzle pressure ratios from 1.3 to 2.4, with and without the door BLC nozzle plugged.

Static Test

At each flap angle of 20, 30, 45, 60, and 70 degrees, four diffuser area ratios (door positions), ranging from 1.37 to 2.22 depending on flap angle were tested. The inlet and end plate BLC nozzles were always open and the upper flap BLC nozzle was always closed. The door BLC nozzle was usually closed for flap angles of 20, 30, and 45 degrees and open for 60 and 70 degrees. The flap BLC nozzle was usually open for flap angles of 20, 30, and 45 degrees and closed for 60 and 70 degrees. At each geometric position, test data were taken at nozzle pressure ratios from 1.28 to 2.40.

Two different hypermixing lobe nozzles were investigated. The difference between the two was the aspect ratio of the hypermixing segments, 5.5 and 11 respectively.

Wind Tunnel Test

The entire wind tunnel test was performed using hypermixing nozzles of aspect ratio 5.5. The aileron angle was 15 degrees and the leading edge slat angle was 60 degrees throughout the test.

The optimum diffuser area ratio at forward speed was chosen for each flap angle by running short polars at two values of thrust coefficient for each diffuser area ratio used in the static test. The selection criteria was maximum thrust for flap angles of 20, 30, and 45 degrees and maximum lift at 60 and 70 degrees.

Most of the test consisted of angle of attack polars at the optimum diffuser area ratios and selected other diffuser area ratios. The angle of attack range was usually from -12 degrees to 32 degrees. The thrust coefficient was held constant over a polar by holding nozzle pressure ratio and wind tunnel dynamic pressure constant. Both were varied to give a range of augmentor thrust coefficients from 0 to 2.73. The nozzle pressure ratio range was from 1.0 to 2.34. Wind tunnel dynamic pressure varied from 1805 N/sq m (37.7 lb/sq ft) to 182 N/sq m (3.8 lb/sq ft). The Reynolds number ranged to 1.4 million per foot. Static data were taken at the optimum diffuser area ratios.

The inlet and end plate BLC nozzles were open throughout the test. At 20 and 30 degrees flap angle, the flap BLC was open and the door and upper flap BLC closed. At 45 degrees, both flap BLC nozzles were open and at 60 and 70 degrees, the door and upper flap BLC nozzles were open and the flap BLC nozzles closed.

DATA ACQUISITION AND REDUCTION

Static Test

One-component force data were acquired from each of the three single-axis load cells. Pressure data from the internal ducts, rakes and mass flow measuring stations were acquired via scanivalve and pressure transducer. Temperature data from internal ducts and mass flow stations were acquired via thermocouples. All analog signals were electronically digitized and punched on paper tape for reduction by computer.

The isentropic thrust is the product of the isentropic velocity, V_I, and the actual mass flow. For each nozzle (hypermixing, inlet, door, flap, upper flap, end plate, leading edge and aileron), V_I was the average of the velocities from the appropriate duct pressures and temperatures. The total mass flow was calculated using a prior calibration with a conical nozzle. The mass flow apportioned to each nozzle was weighted for area and velocity.

The augmentor forces were extracted from the total forces by subtracting the estimated forces of the leading edge, aileron, and upper flap BLC. These forces were estimated to be 85 percent of their isentropic values.

The gross augmentation ratio is the ratio of the measured augmentor force to the augmentor nozzle force. The augmentor nozzle forces are the sum of measured forces from the nozzle calibration with the flap

8

and flap tube removed and the door BLC closed, and 85 percent of the flap BLC isentropic force for 20, 30, and 45 degrees flap angle, and the measured force with the door BLC open for 60 and 70 degrees. The augmentor nozzle force is approximately a straight line function of nozzle pressure ratio.

The rake data was stepwise integrated for mass flow and momentum at each rake station and stepwise integrated over the span.

Wind Tunnel Test

Data acquisition for the wind tunnel test was similar to that of the static test with two additions. The force data was six-component force and moment data from the wind tunnel balance system. Also, pressure data was acquired from the surface pressure taps on the forward wing surface. Of the six components, only lift, drag, and pitching moment were calculated. The reference moment center was at the one-quarter chord of the mean aerodynamic chord. The drag and angle of attack were corrected using standard wall corrections and the "aerodynamic lift coefficient" as follows:

$$C_D = C_{D_u} + .0032 \; C_{L_{aero}}^2$$

$$\alpha = \alpha_u + .1813 \; C_{L_{aero}} \qquad \text{(deg)}$$

where

$$C_{L_{aero}} = C_L - .85 \; [C_{J_I} \sin (\alpha_u + \delta_f) + C_{\mu_A} \sin (\alpha_u + \delta_a) + C_{\mu_{LE}} \sin \alpha_u].$$

9

RESULTS AND DISCUSSION

Figure 3 presents the results of the augmentor nozzle calibration for both nozzle aspect ratios. Results for the aspect ratio 5.5 nozzles are from the wind tunnel force data, while results for aspect ratio 11 nozzles are from the static test. The isentropic thrust is given for each calibration. Figure 4 shows the flap BLC nozzle isentropic thrust, 85 percent of which is added to the nozzle calibration thrust for flap angles of 20, 30, and 45 degrees.

Figure 5 gives the values of isentropic blowing coefficient, C_μ, for all of the BLC nozzles as a function of augmentor thrust coefficient, C_J, for all configurations.

Figure 6 shows the gross augmentation values achieved in the wind tunnel at the optimum diffuser area for each flap angle. The maximum was at 45 degrees flap angle even though the nozzle axis was aligned with the augmentor axis at 60 degrees.

Figures 7 and 8 show gross augmentation levels achieved at the Static Test Facility for nozzle aspect ratios 5.5 and 11 respectively. Note that some of the data differs from wind tunnel data in figure 6. The discrepancies are in the static test data and are believed due to wind, inaccuracies in the load cell measuring system and differences in the augmentor root end plate. Therefore, the static test force data should be viewed as showing trends only, not absolute data. The aspect ratio 5.5 nozzles were chosen for the wind tunnel test based on their apparent higher augmentation at most flap angles.

Figures 9 through 13 give augmentor exit velocity profiles at five spanwise stations for each flap angle. The data are for the optimum area ratios used in the wind tunnel test. Data are given for the wind-off case for each flap angle and six forward velocities at 30 degrees flap angle.

Results of an analysis of exit rake data at 30 degrees flap angle are summarized in figures 14, 15, and 16. Figure 14 shows a comparison of direct force measurement and integration of exit velocity profiles. The integration follows, although exaggerates, the force changes with pressure ratio.

The mass flow ratio is also shown in figure 14 and is fairly constant with pressure ratio. Figure 15 shows the effect of velocity ratio on mass flow ratio at several pressure ratios and diffuser area ratios. Note that the nozzle pressure ratio has little effect while increasing area ratio has substantial effect.

Figure 16 shows the effect of velocity ratio on the integrated gross and net thrust ratios at several pressure ratios and diffuser area ratios. The static nozzle thrust is used as the reference and the difference between gross and net thrust is the ram drag of the secondary mass flow. The gross thrust increases and the net thrust decreases with velocity ratio.

The gross and net thrust are highest at an area ratio of 1.37 and a nozzle pressure ratio of 2.32. Lowering the pressure ratio lowers the net thrust. Increasing the area ratio lowers gross thrust

and increases the ram drag (mass flow), hence lowering the net thrust substantially. Decreasing the area ratio lowers ram drag (mass flow), but the decrease in gross thrust causes the net thrust to be lower than that of the optimum configuration.

Figures 17 through 21 show force data results from the wind tunnel tests. A limited summary is presented in figures 22 through 25. Figure 22 summarizes the lift performance at zero angle of attack. Forward speed and nozzle pressure ratio have little effect on correlation of the lift data except in the form of the thrust coefficient, C_J.

Figures 23 and 24 show net drag at a constant lift coefficient for various area ratios, forward speeds, and pressure ratios for 20 and 30 degrees flap angle, respectively. The force results shown in figure 24 generally agree with the rake data of figure 16 except that the trend with nozzle pressure ratio is reversed. The force data indicates that the lower pressure ratio gives the highest net thrust.

Figure 25 is a comparison of the best thrust data from the test and similar data from an augmentor wing and an internally blown flap of reference 4. The data indicates that augmentors give significant thrust improvements at high thrust coefficients (low forward velocity and low ram drag), but lose this advantage at low thrust coefficients (high forward velocity and high ram drag).

Although the model demonstrated good lift and thrust performance at forward speed, it failed to achieve the static thrust augmentation values shown in reference 3. There are several possible explanations for this failure. First, it was obvious from the augmentor exit rake data and, most importantly, from feeling the exit flow field by hand, that there was a significant "hole" or area of lower velocity in the middle 20 percent of the augmentor span. The cause of this "hole" was not evident. One possible cause was a small strut which held the flap tube to the main wing structure.

A second possible explanation was the apparent lack of effective BLC on the door. There are two indications of this. First, the augmentation values peaked at a lower value of diffuser area ratio than the data of reference 3 indicating a BLC problem. Second, the augmentation was much lower for 60 and 70 degrees of flap angle than for 20, 30 and 40 degrees indicating the lack of BLC was on the door side of the throat.

A third explanation was the possible lack of "hypermixing" from the primary nozzles. There was no indication of change in flow direction from feeling the primary exhaust by hand. This deficit could also explain the failure of the higher aspect ratio hypermixing segment to increase the augmentation ratio as suggested in reference 2.

13

REFERENCES

1. Falarski, M. D. and Koenig, D. G.: Longitudinal and Lateral
    Stability and Control Characteristics of a Large-Scale Model
    with a Swept Wing and Augmented Jet Flap. NASA TM X-62,145,
    April 1972.

2. Bevilaqua, P. M.: An Analytic Description of Hypermixing and
    Test of an Improved Nozzle. AIAA Paper 74-1190, October 1974.

3. Streiff, H. G. and Henderson, C.: Ejector Thrust Augmentation
    for STOL Aircraft Applications. AIAA Paper 74-1192, October
    1974.

4. Koenig, D. G. and Falarski, M. D.: Wind Tunnel Investigation
    of the Thrust Augmentor Performance of a Large-Scale Swept Wing
    Model. NASA TM X-73,239, July 1977.

TABLE I.- MODEL REFERENCE DIMENSIONS

Wing

Area, sq m (sq ft) (half-span)	6.13 (65.95)
Aspect ratio	8.0
Taper ratio	.372
Semispan, m (ft)	4.95 (16.25)
Root chord, m (ft)	1.80 (5.92)
Tip chord, m (ft)	.67 (2.20)
Mean aerodynamic chord, m (ft)	1.32 (4.34)
Sweep at ¼ chord, deg	25
Incidence to fuselage, deg	2
Twist, deg	0
Airfoil section	.17 t/c Supercritical (modified)

TABLE II.- BLOWING NOZZLE DIMENSIONS

Nozzle	Gap		Area	
	cm	(in)	sq cm	(sq in)
Hypermixing	.37	(.146)	200.0	(31.0)
Inlet BLC	.048	(.019)	16.4	(2.5)
Door BLC	.102	(.040)	34.6	(5.4)
Flap BLC	.127	(.050)	42.6	(6.6)
Upper Flap BLC	.127	(.050)	42.6	(6.6)
End Wall BLC	.18	(.07)	2.7	(.4)
Leading Edge BLC	.043 to .056	(.017 to .022)	22.6	(3.5)
Aileron BLC	.102	(.040)	9.7	(1.5)
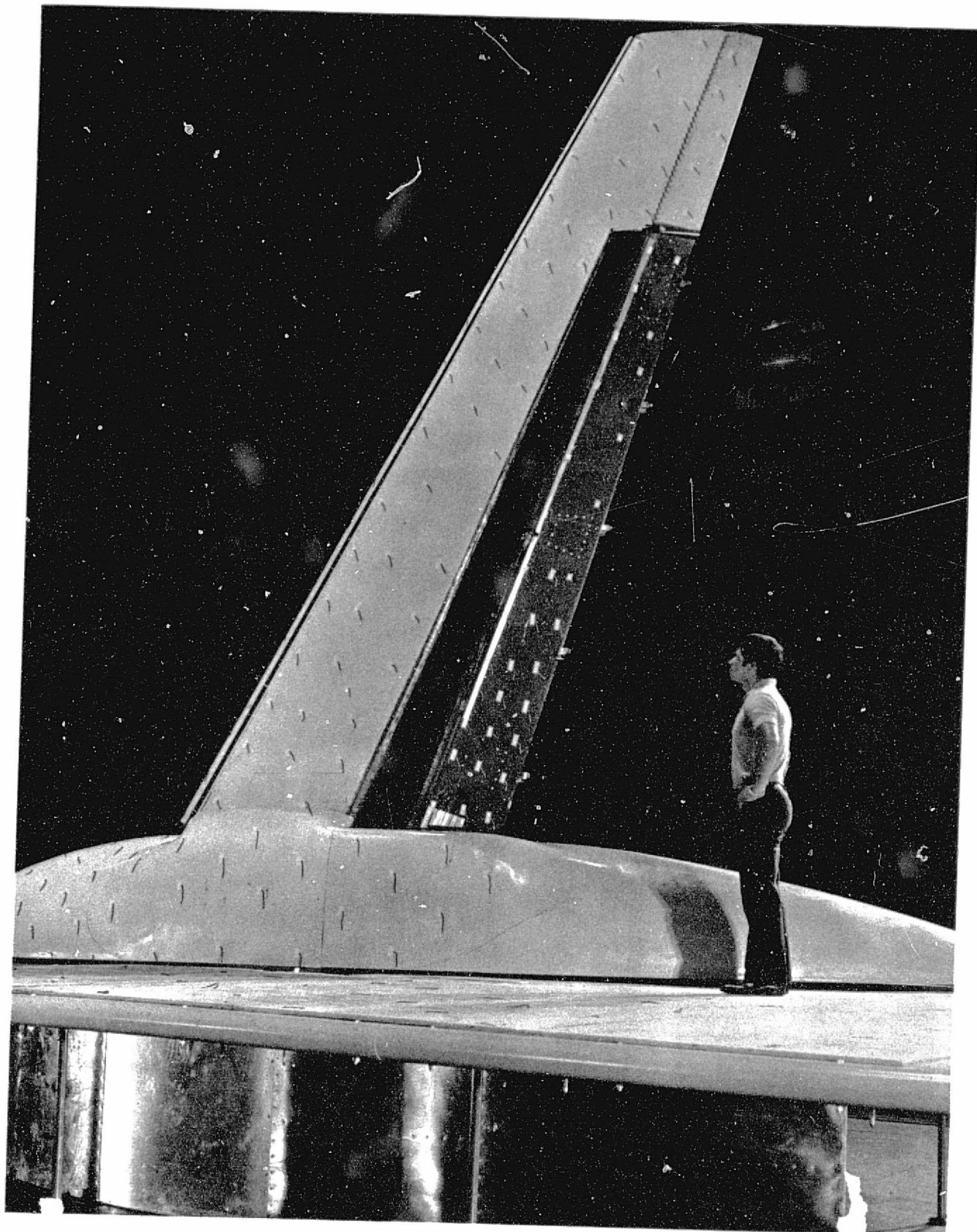
(a) View of wing top surface.

Figure 1.- Views of model installed in wind tunnel.
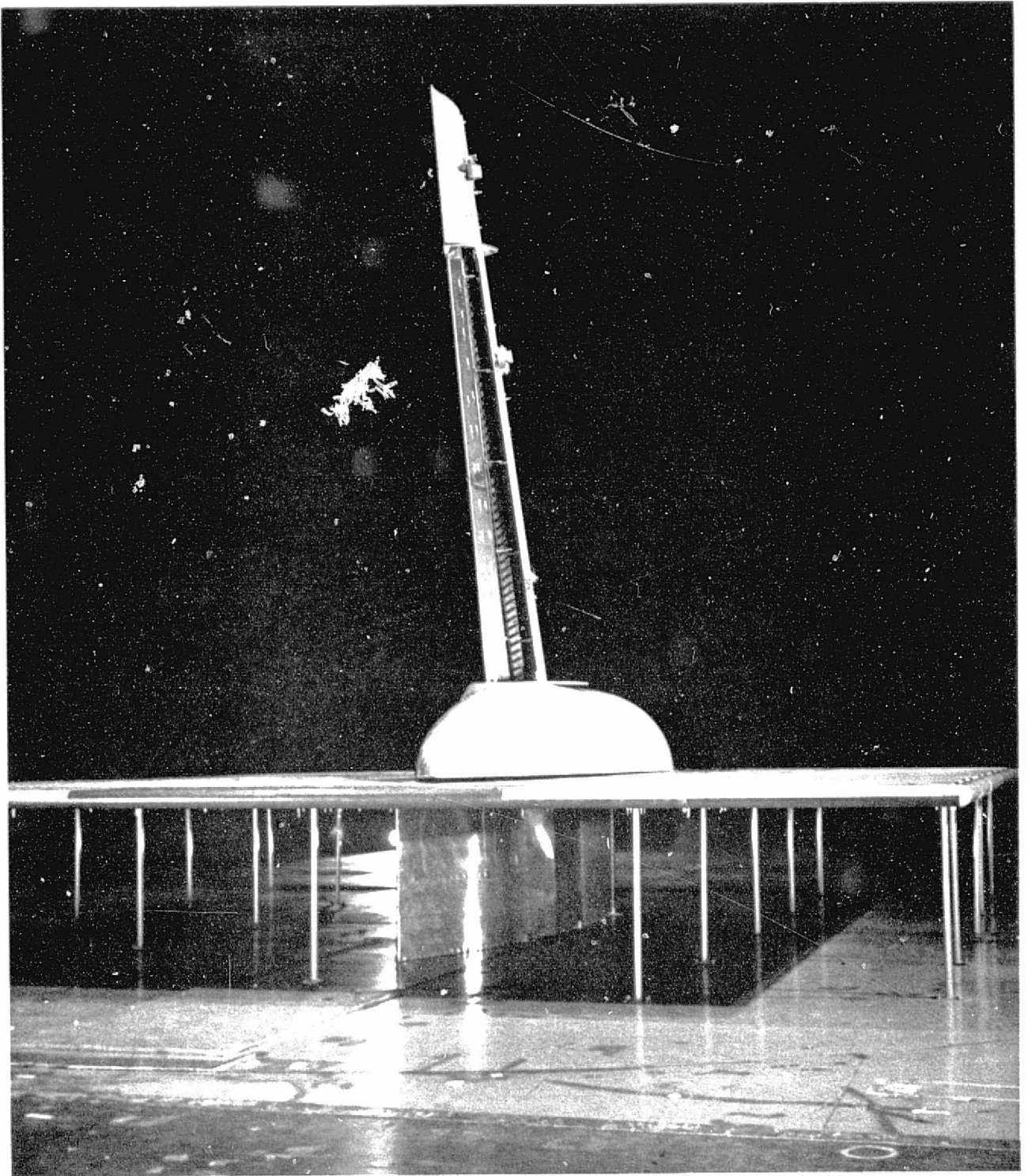
(b) Rear view of model.

Figure 1.- Continued.

18

(c) View of bottom of wing.

Figure 1.- Concluded.

7.62
(25.00)

8.53
(28.00)

.17
(.55)

25°

1.07
(3.50)

.23
(.75)

4.95
(16.25)

C̄

1.32
(4.34)

2.10
(6.89)

.102
(.333)

.69
(2.25)

1.17
(3.83)

WIND TUNNEL FLOOR

C/4

1.19
(3.92)

1.22
(4.00)

1.22
(4.00)

5.03
(16.5)

6.10
(20.00)
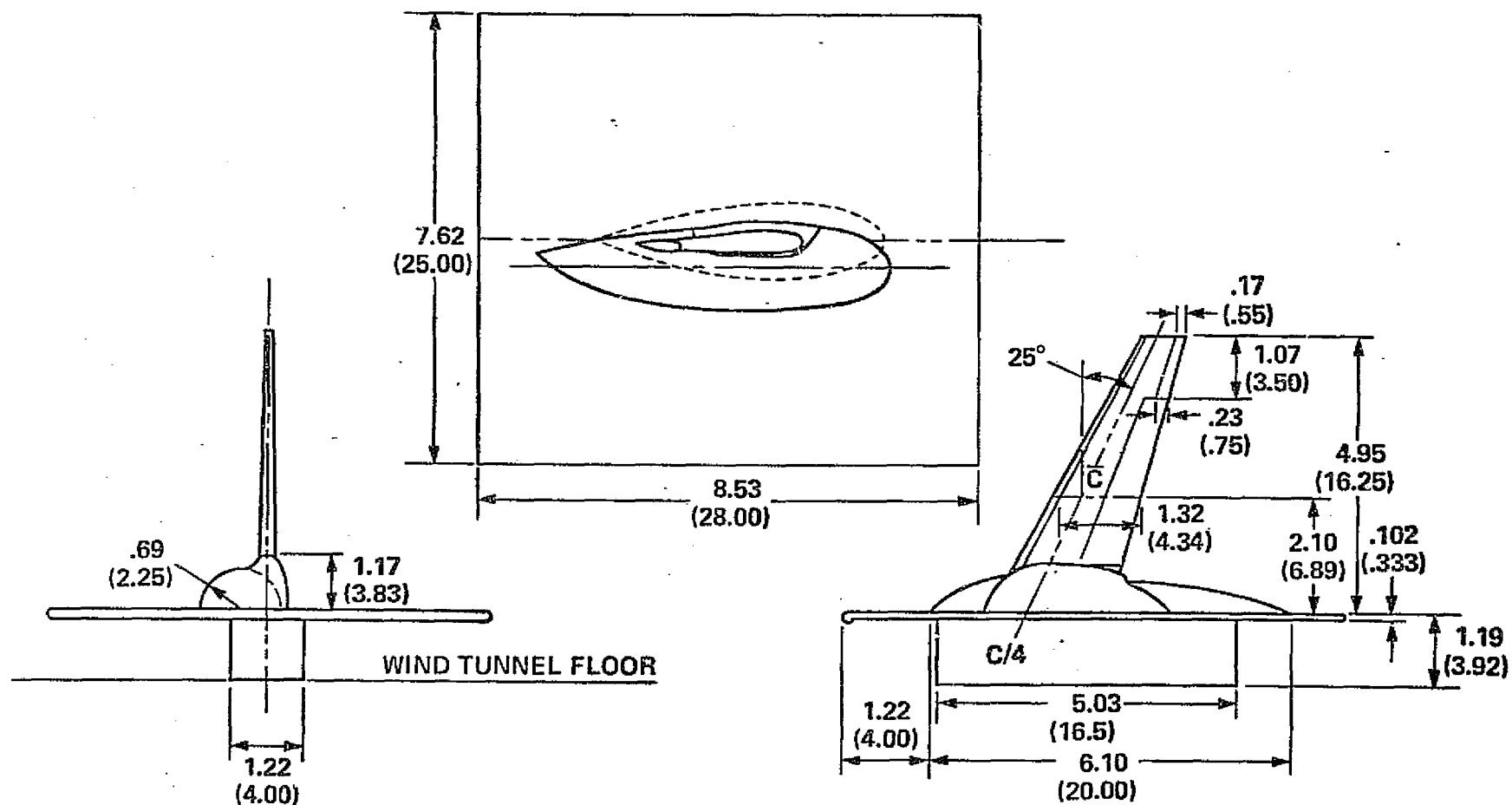
(a) Three-view sketch of the model.

Figure 2.- Geometric details of the model.

J–85/VIPER LOAD
COMPRESSOR WITH
INLET & EXHAUST
SUPPRESSORS

COMPRESSOR ENCLOSURE

30.5 cm (12 in.) DUCTING

EXPANSION BELLOWS

DUCTING SUPPORT

4.36 m
(14.3 ft)

SEMISPAN AUGMENTOR
WING MODEL

EXPANSION BELLOWS

SEMISPAN AUGMENTOR
WING PEDESTAL

FORCE ISOLATION GLAND
LOAD CELL PLATFORM
STATIC TEST STAND

2.19 m
(7.17 ft)

~ 30 m (100 ft)

CONCRETE & ASPHALT SURFACE
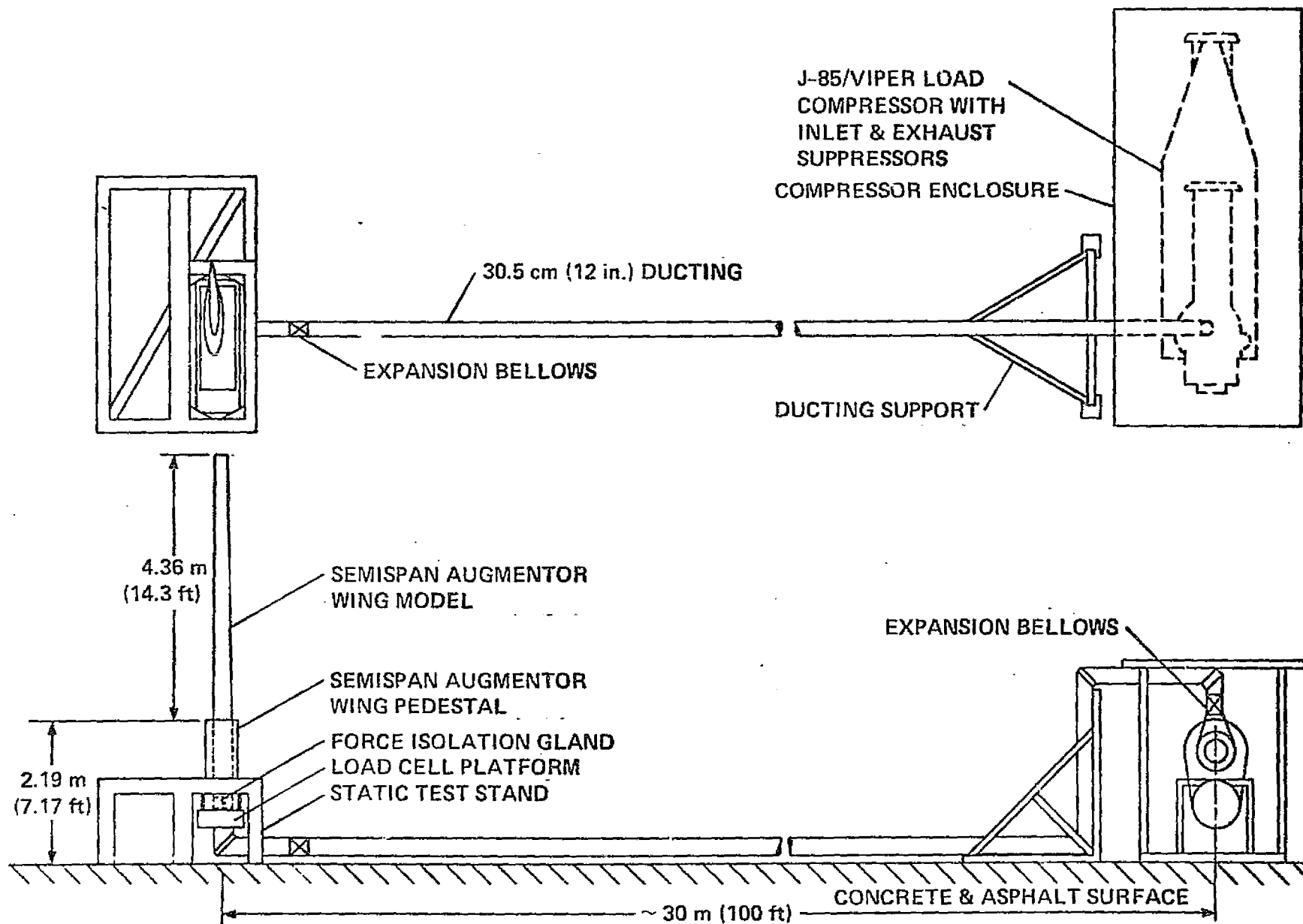
(b) General arrangement of the static test.

50%C

δ_s

δ_f
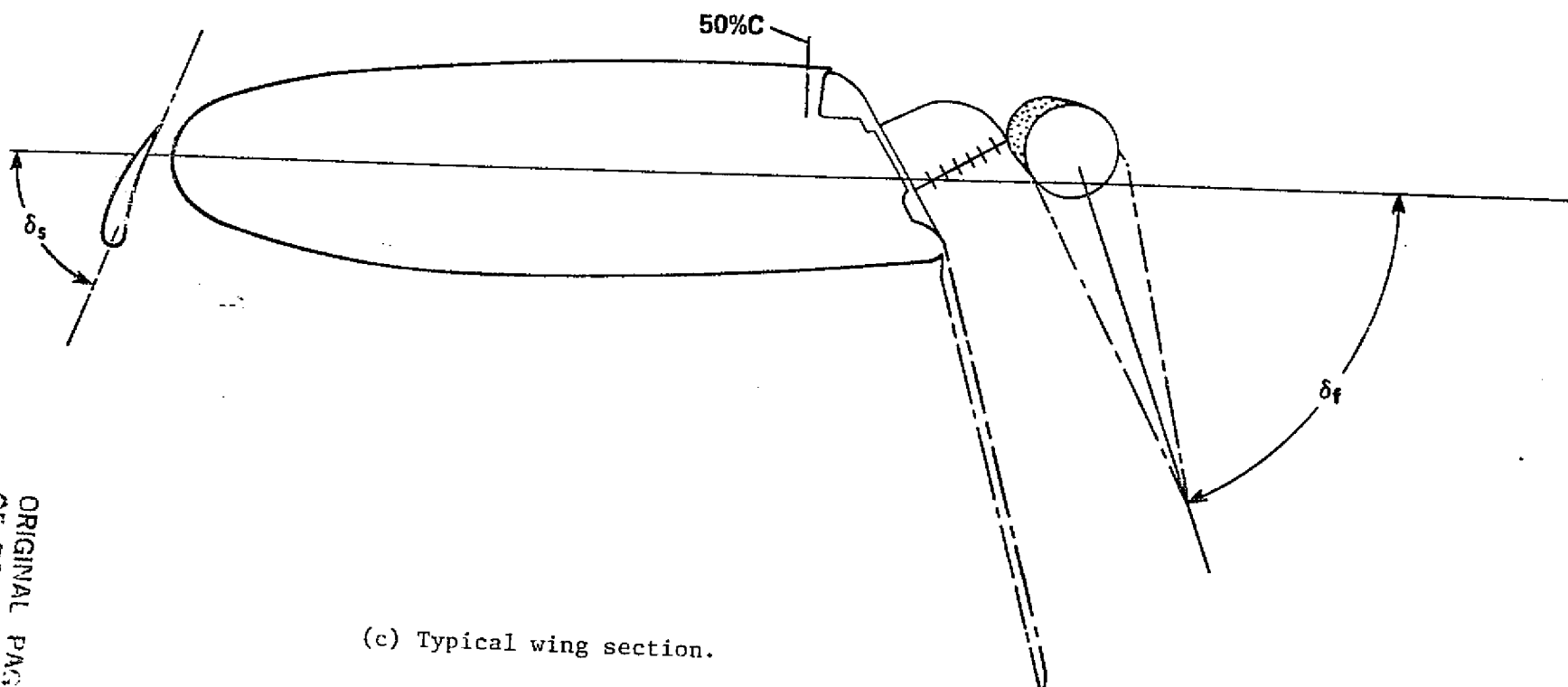
(c) Typical wing section.

Figure 2.- Continued.

VIPER COMPRESSOR
OUTPUT

J-85, VIPER EXHAUST

1.96
(6.45)

1.35
(4.45)

.52
(1.70)

.27
(.89)

J-85

4.23
(13.90)

1.27
(4.16)
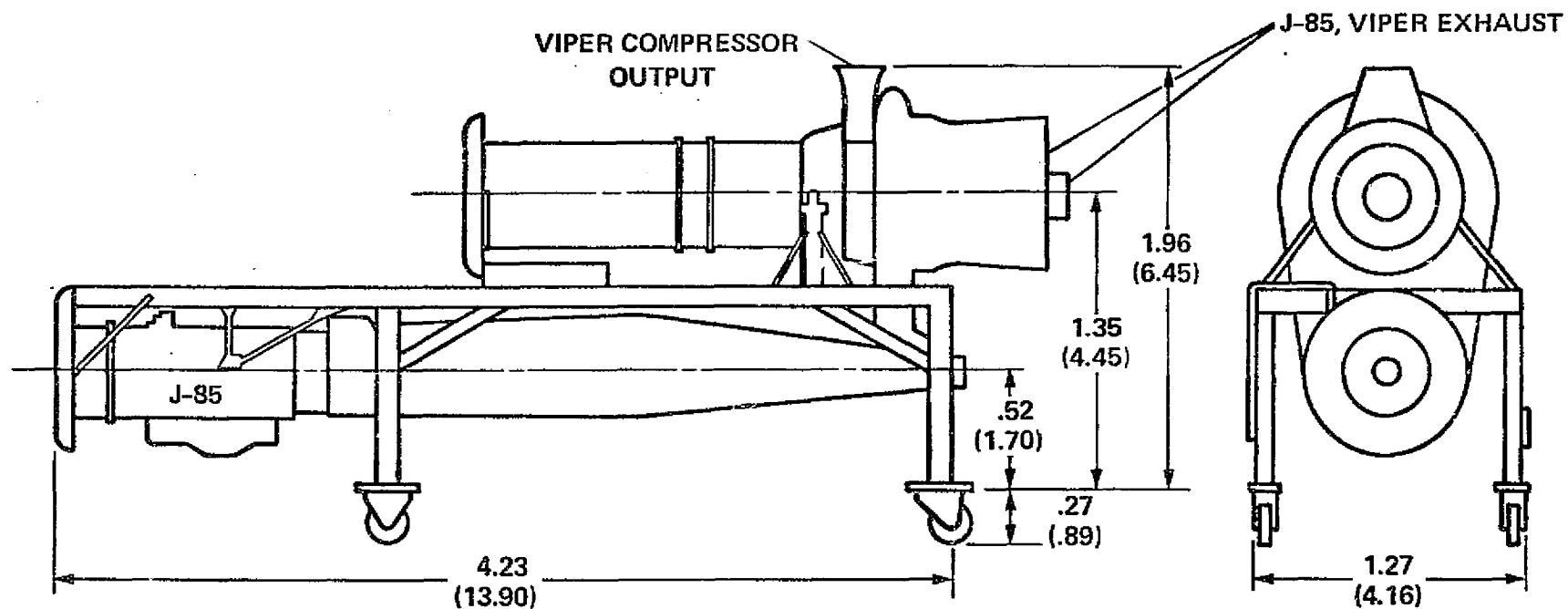
(d) Schematic of turbocompressor.

Figure 2.- Continued.

INLET BLC NOZZLE

NOZZLE PLENUM

HYPERMIXING LOBE NOZZLE

UPPER FLAP BLC NOZZLE

FLAP SUPPLY TUBE

FLAP

50%C

DOOR

WING CHORD PLANE

DOOR BLC NOZZLE

FLAP BLC NOZZLE

63%C

δ_f
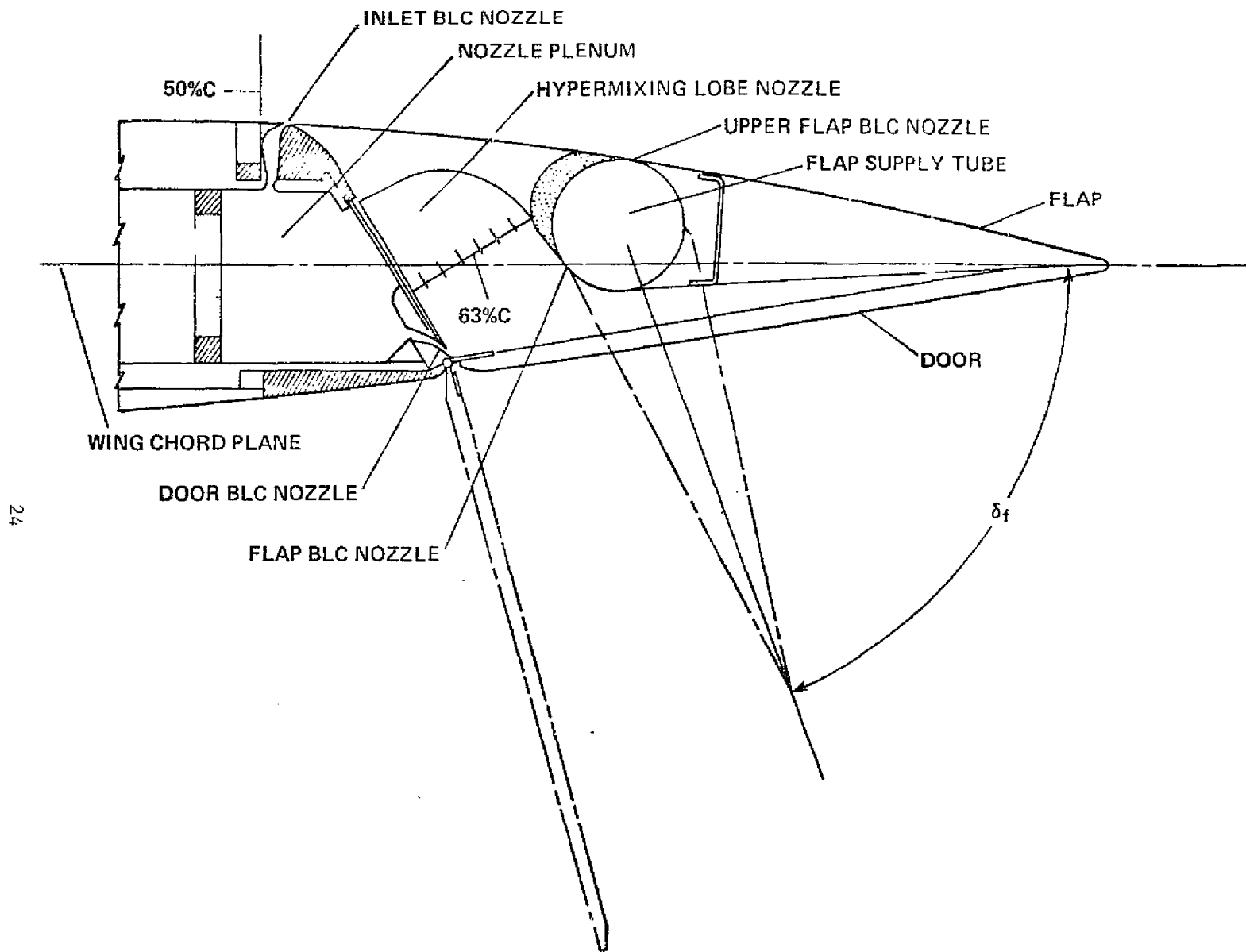
(e) Augmentor geometry.

Figure 2.- Continued.

24

HYPERMIXING SEGMENTS
(5 ON INNER 17 NOZZLES
 4 ON MIDDLE 17 NOZZLES
 3 ON OUTER 16 NOZZLES)

NON-HYPERMIXING SEGMENT

9.88 (3.89) — INNER 25 NOZZLES
7.49 (2.95) — OUTER 25 NOZZLES

A

14 (5.5) AT ROOT

2.03 (.80)

A

7.6 (3) AT TIP

NOTE
1. EVERY SEGMENT ALTERNATES
   DIRECTION FOR NAR = 5.5,
   EVERY 2 SEGMENT ALTERNATES
   DIRECTION FOR NAR = 11

2. DIMENSIONS IN cm (in.)

8.5°
(TYP)

GAP
.37 (.146)

.29 (.114)

.28 (.112)

SECTION A-A
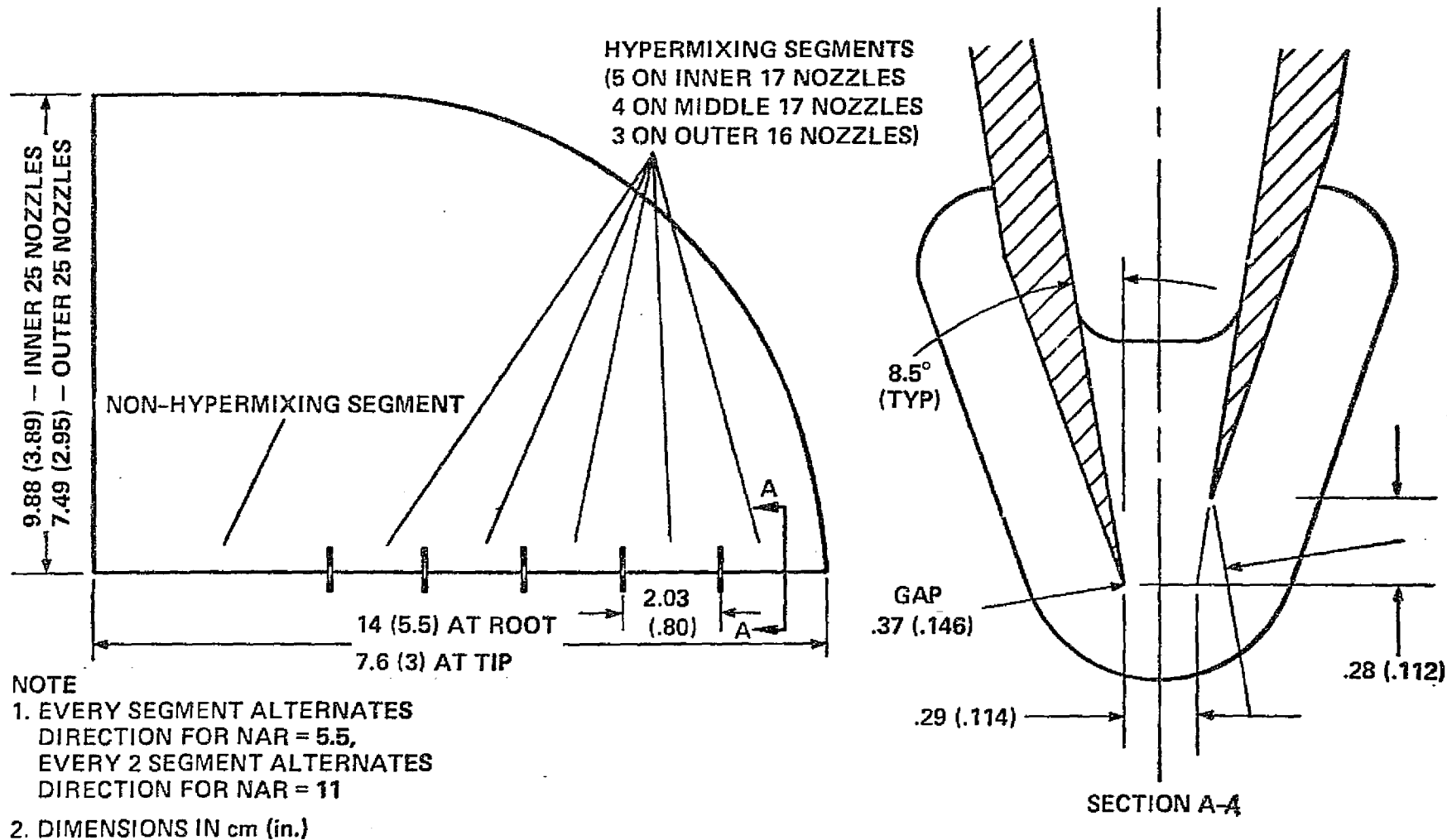
(f) Hypermixing lobe geometry.

Figure 2.- Continued.

25

LEADING EDGE BLOWING SLOT
ROOT — .056 cm (.022 in.)
TIP   — .038 cm (.015 in.)

1.5%C

20°

WING CHORD PLANE

4.28%C

δ_s

10%C

ST. CYR SLAT

26
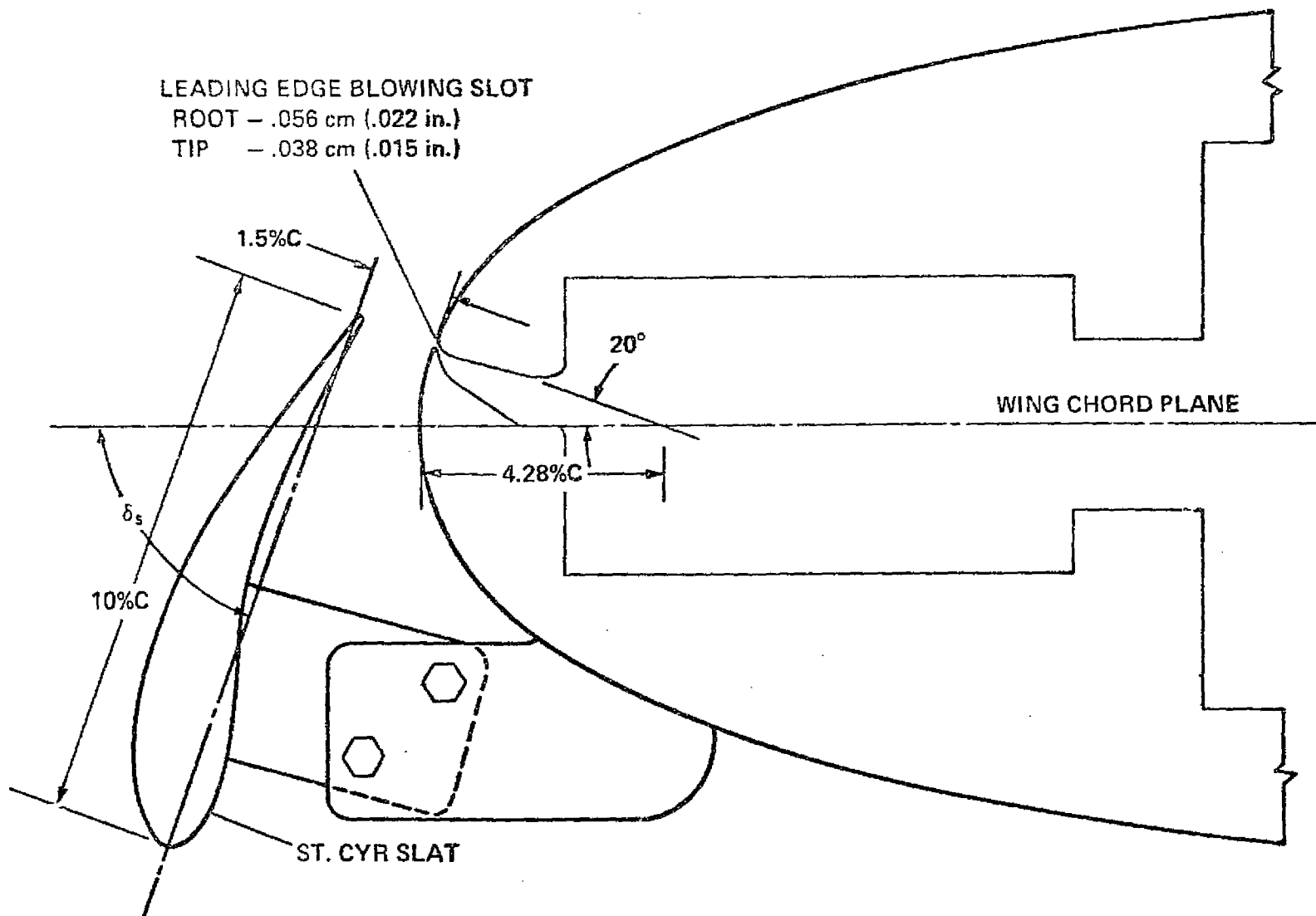
(g) Leading edge slat and blowing slot geometry.

Figure 2.- Continued.

35 – 2.86 cm x .10 cm (1.13 in. x .04 in.)
BLOWING SLOTS

8.9%C

WING CHORD PLANE

50%C

HINGE
75%C
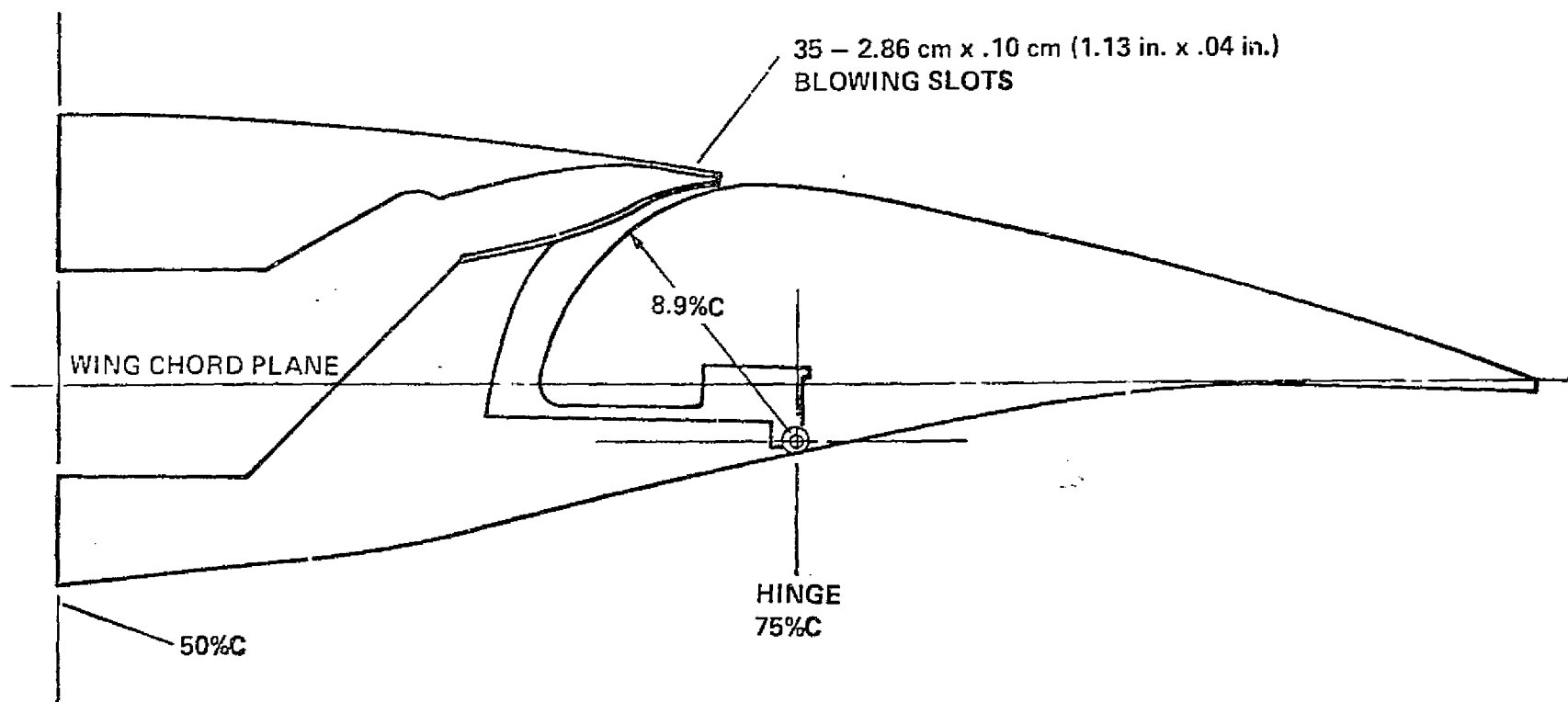
(h) Aileron geometry.

Figure 2.- Concluded.
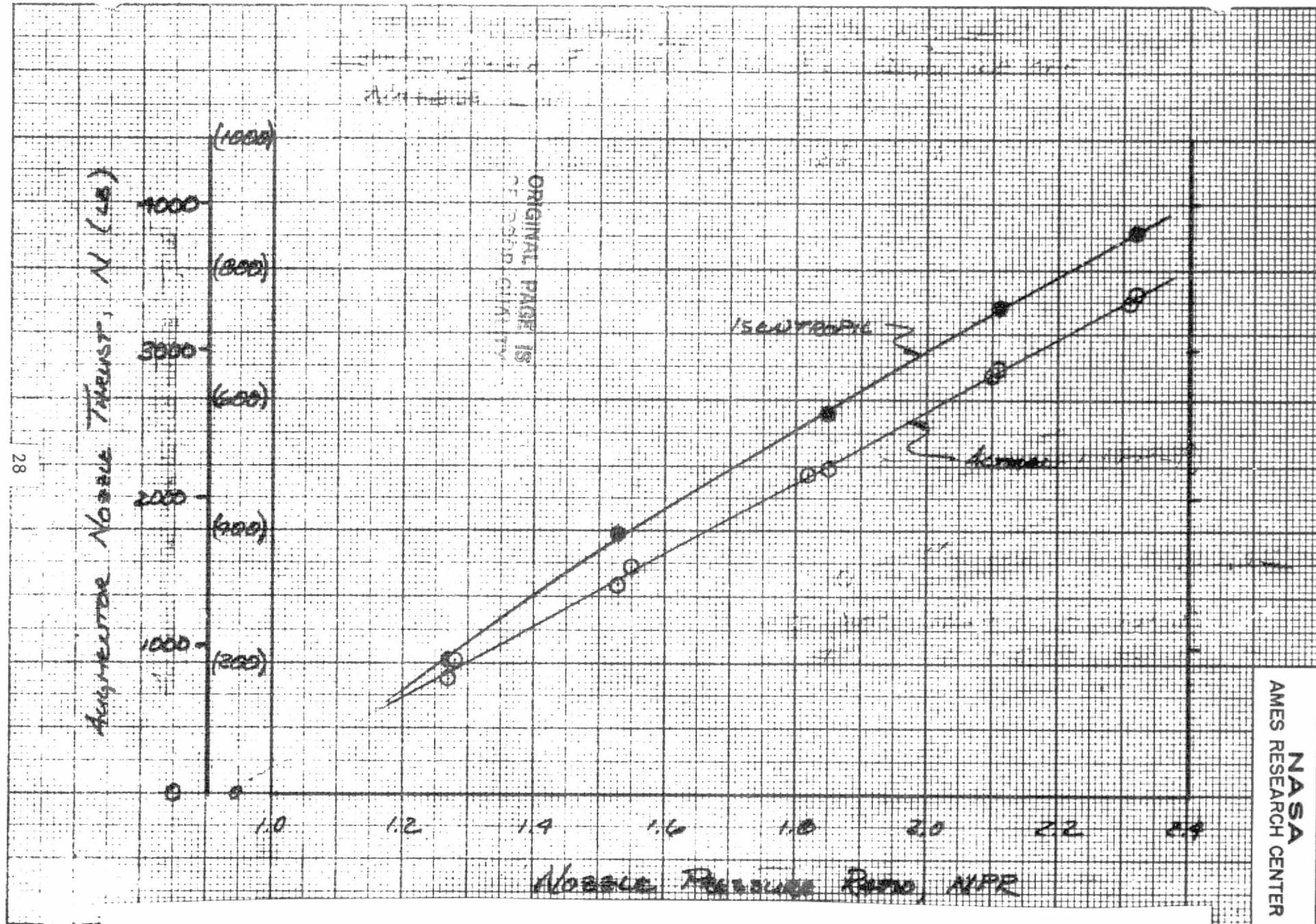
(a) Wind tunnel data, NAR = 5.5, door BLC closed, flap BLC off.

Figure 3.- The effect of nozzle pressure ratio on augmentor nozzle thrust.
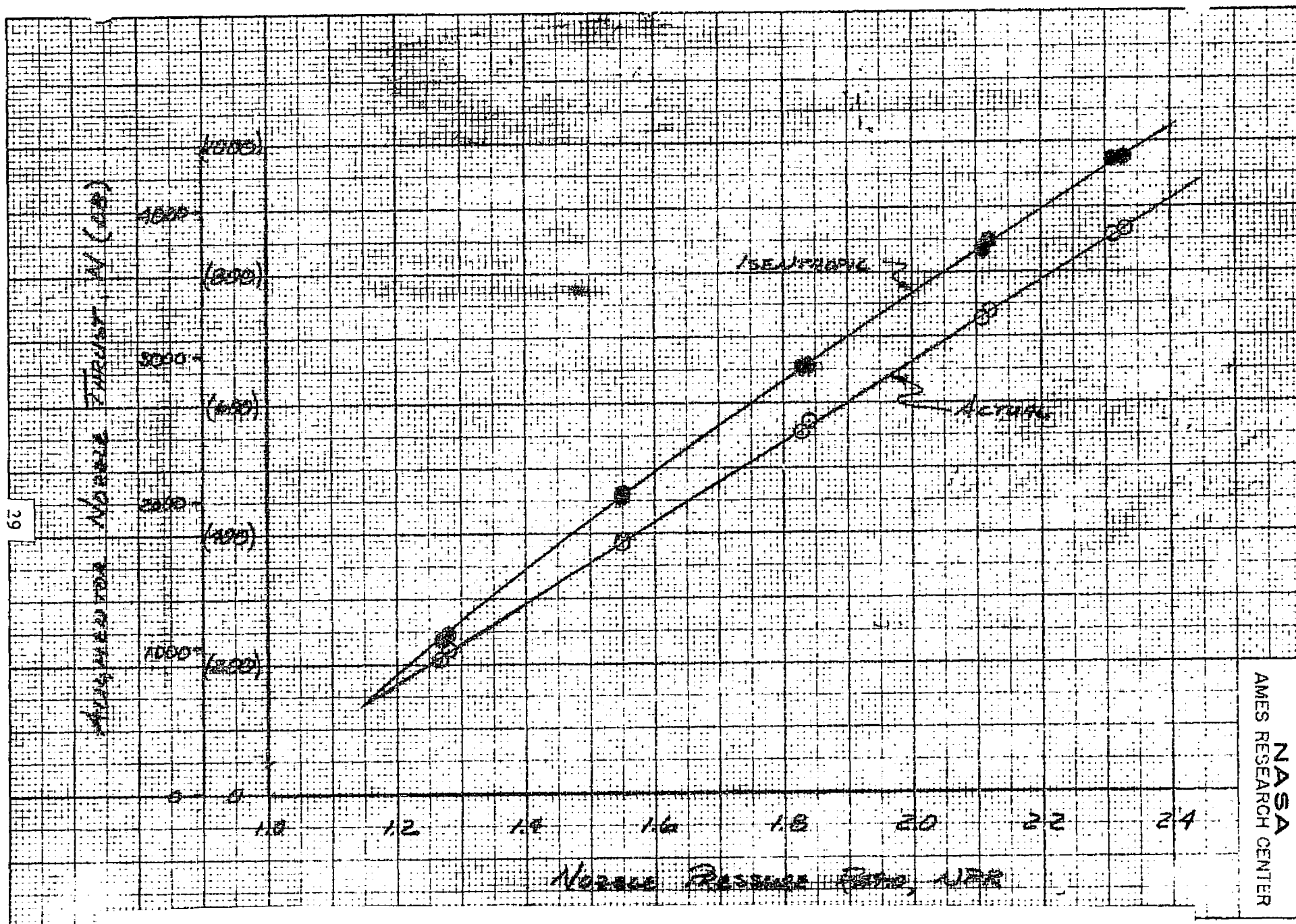
(b) Wind tunnel data, NAR = 5.5, door BLC open, flap tube off.
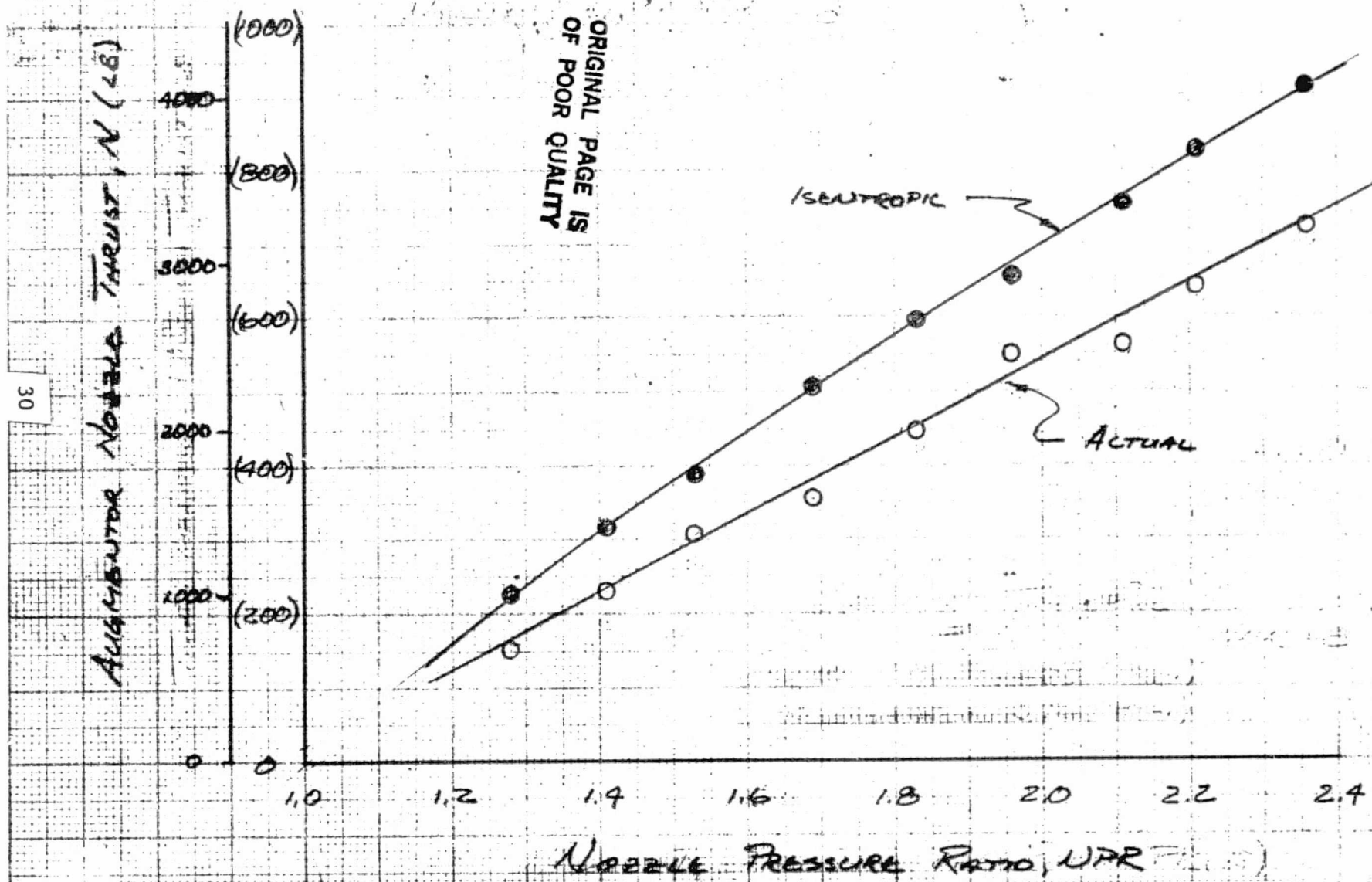
Figure 3.- Continued.

(c) Static data, NAR = 11, door BLC closed, flap tube off.

Figure 3.- Continued.
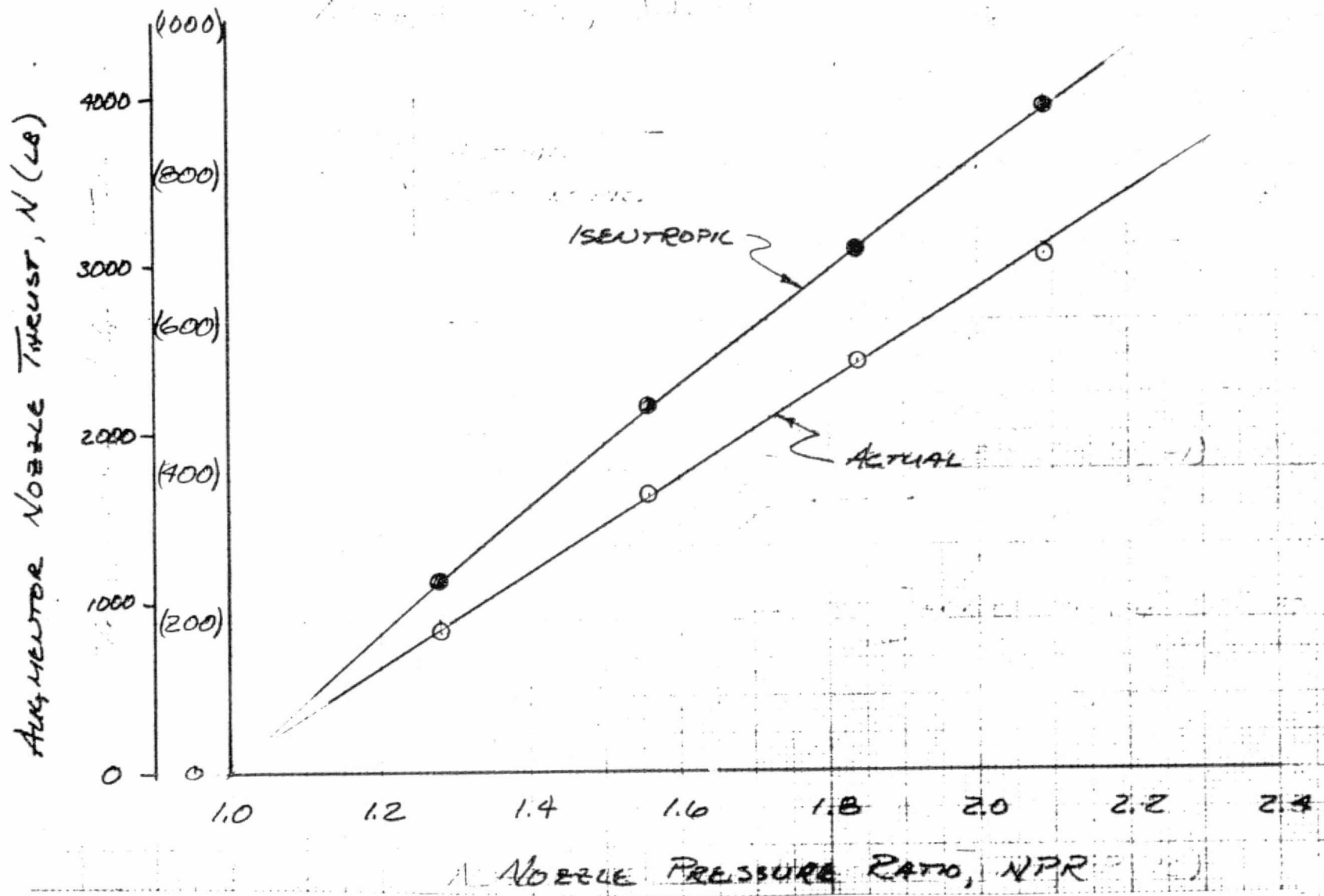
(d) Static data, NAR = 11, door BLC open, flap tube off.

Figure 3.– Concluded.
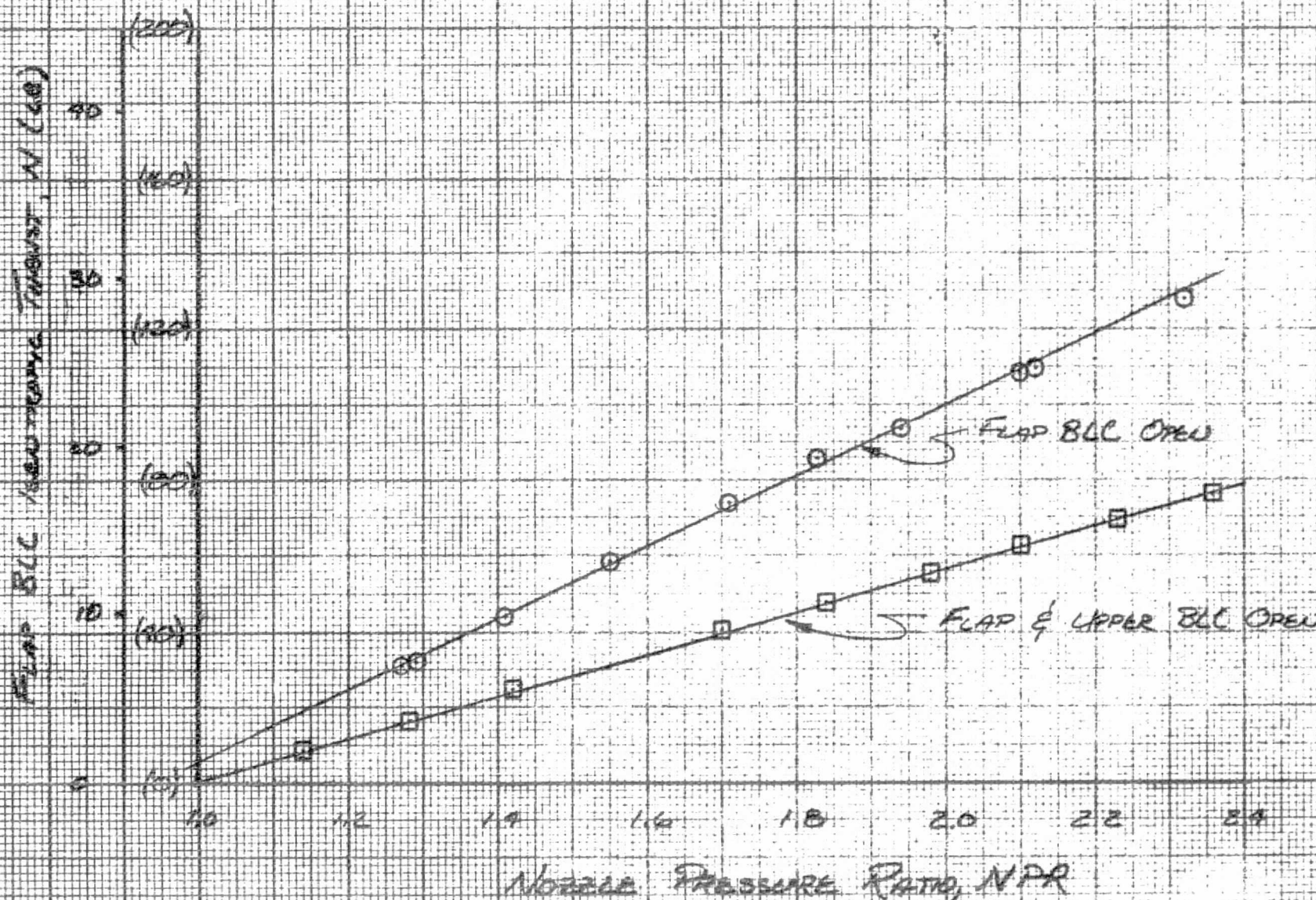
Figure 4.- The effect of nozzle pressure ratio on the flap BLC nozzle
isentropic thrust.

(a) δ_f = 20, 30 deg.

Figure 5.- Values of isentropic thrust coefficients.
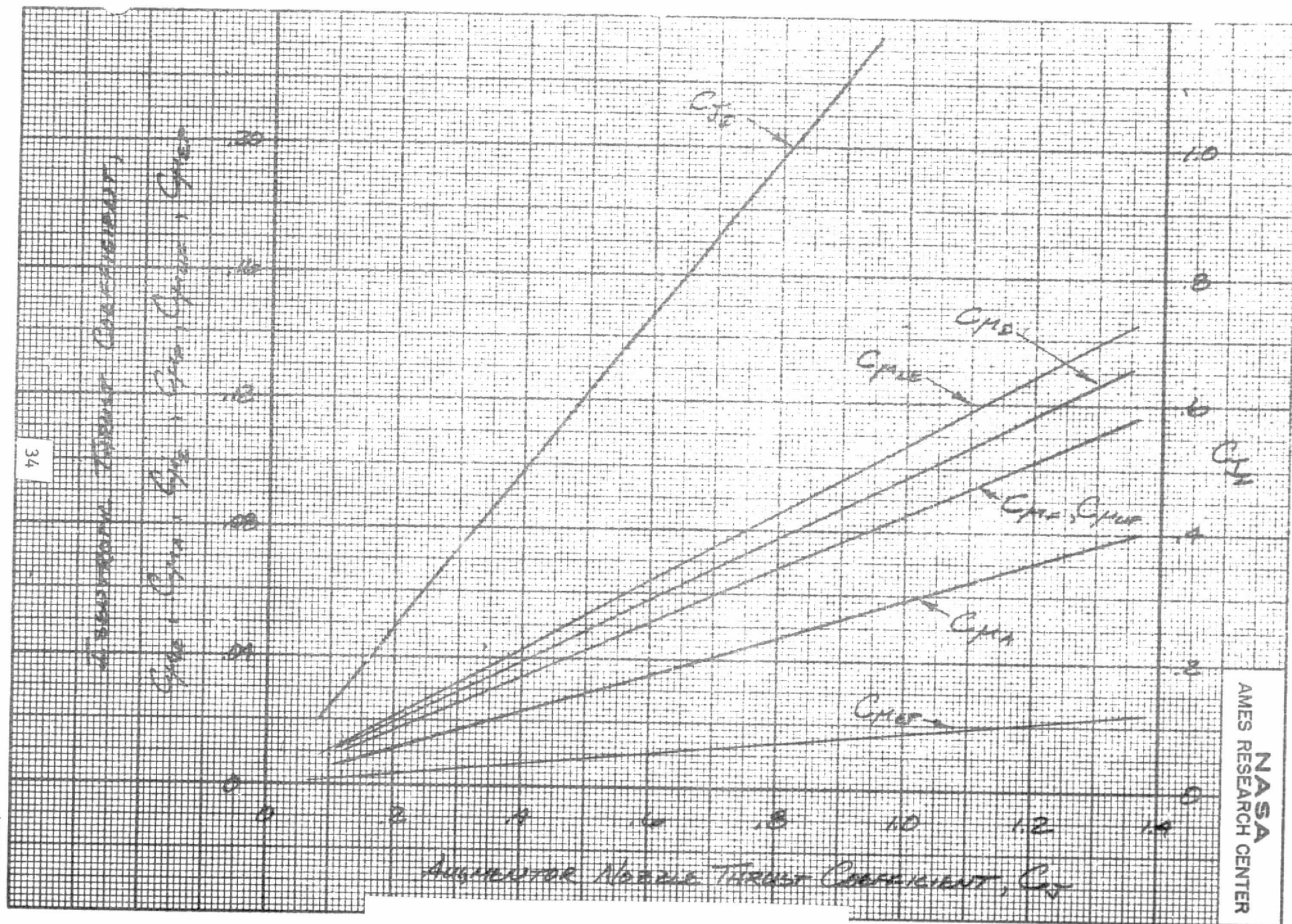
(b) δ_f = 45 deg.

Figure 5.- Continued.
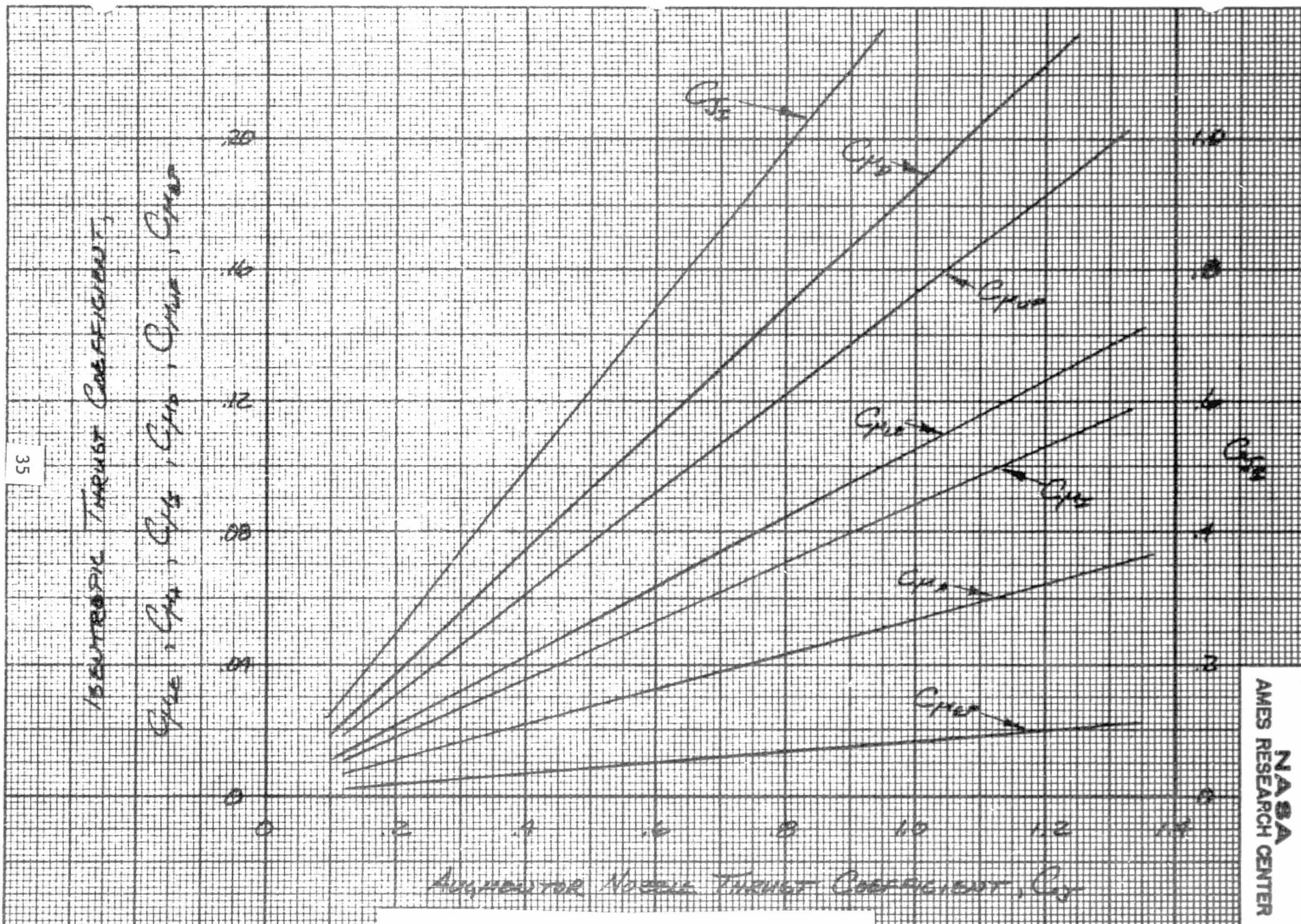
(c) δ_f = 60, 70 deg.

Figure 5.- Concluded.

35
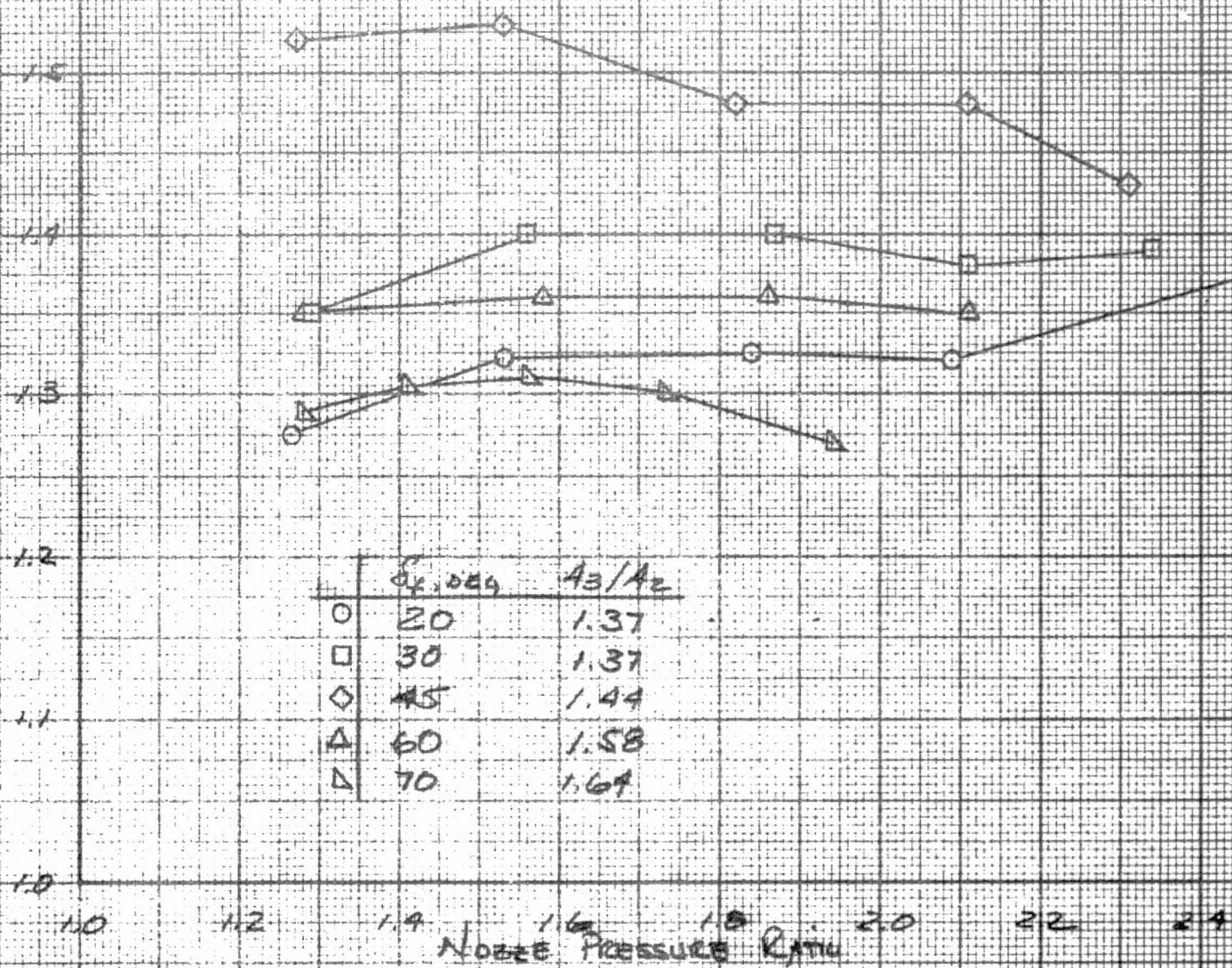
Figure 6.- The effect of flap angle on the gross augmentation ratio,
wind tunnel data, NAR = 5.5.
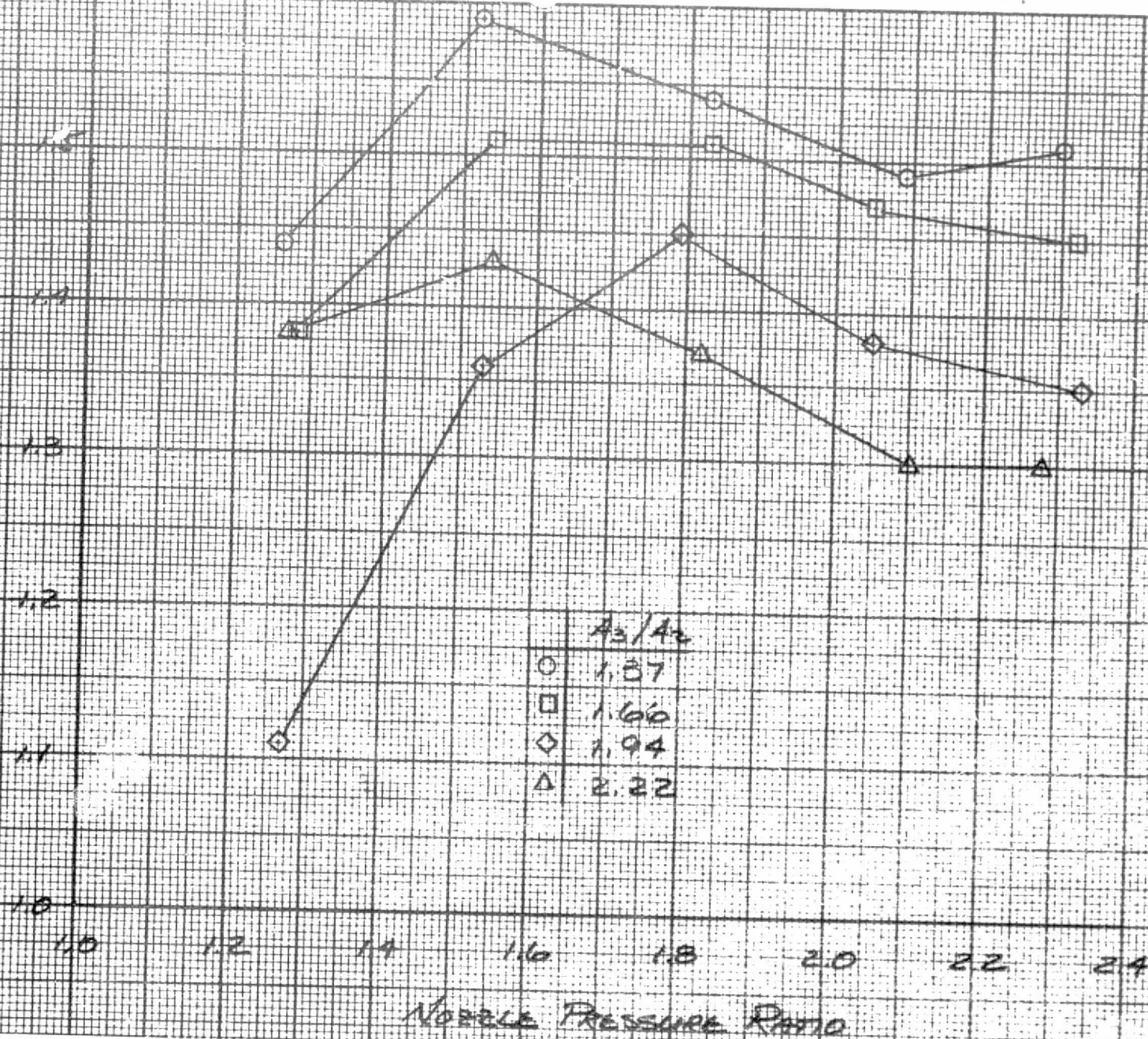
(a) $\delta_f = 20°$.

Figure 7.- The effect of diffuser area ratio on the gross augmentation
ratio, static data, NAR = 5.5.

38

NASA
AMES RESEARCH CENTER

(b) $\delta_f = 30°$.

Figure 7.- Continued.

(c) $\delta_f = 45°$.

Figure 7.- Continued.
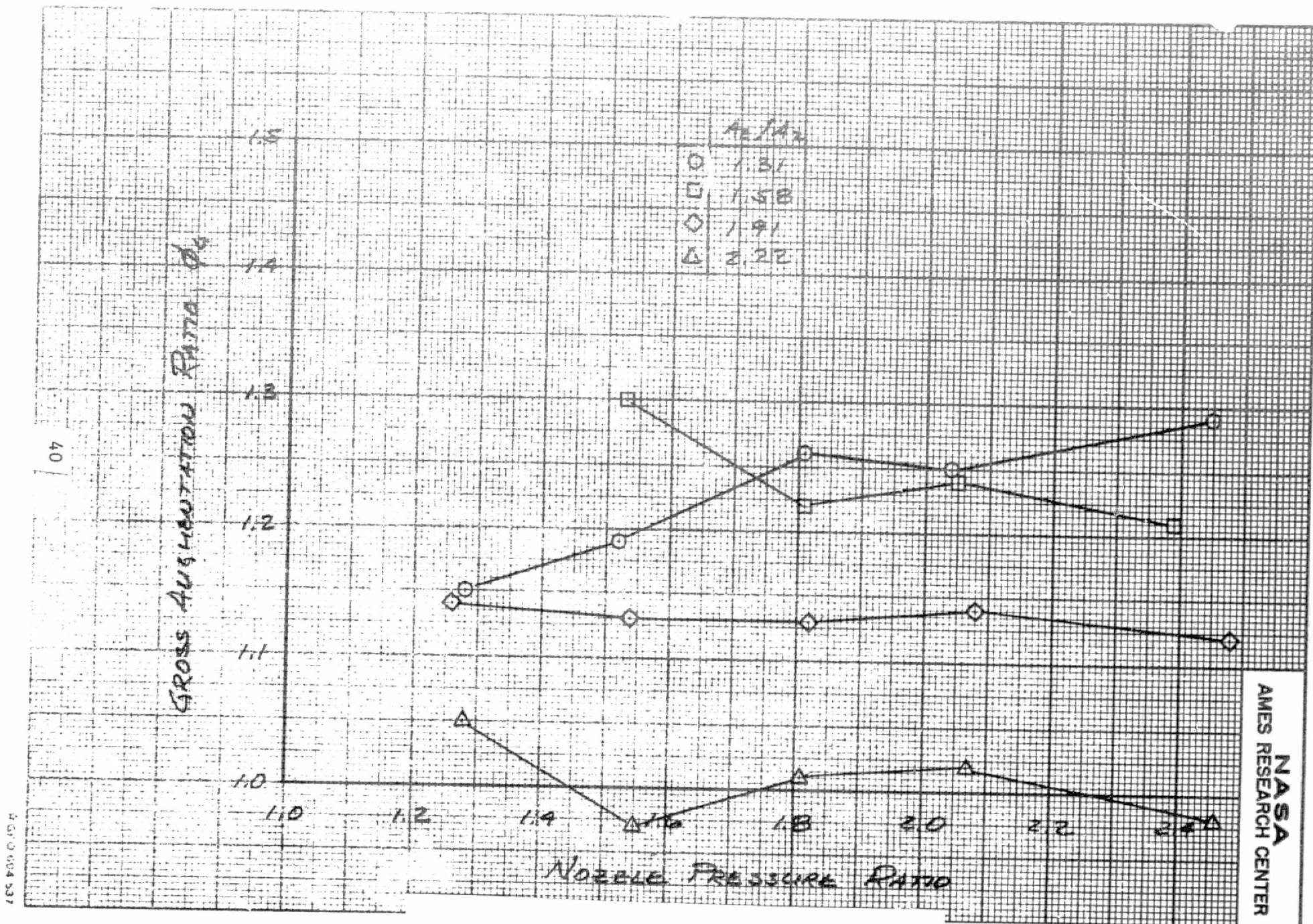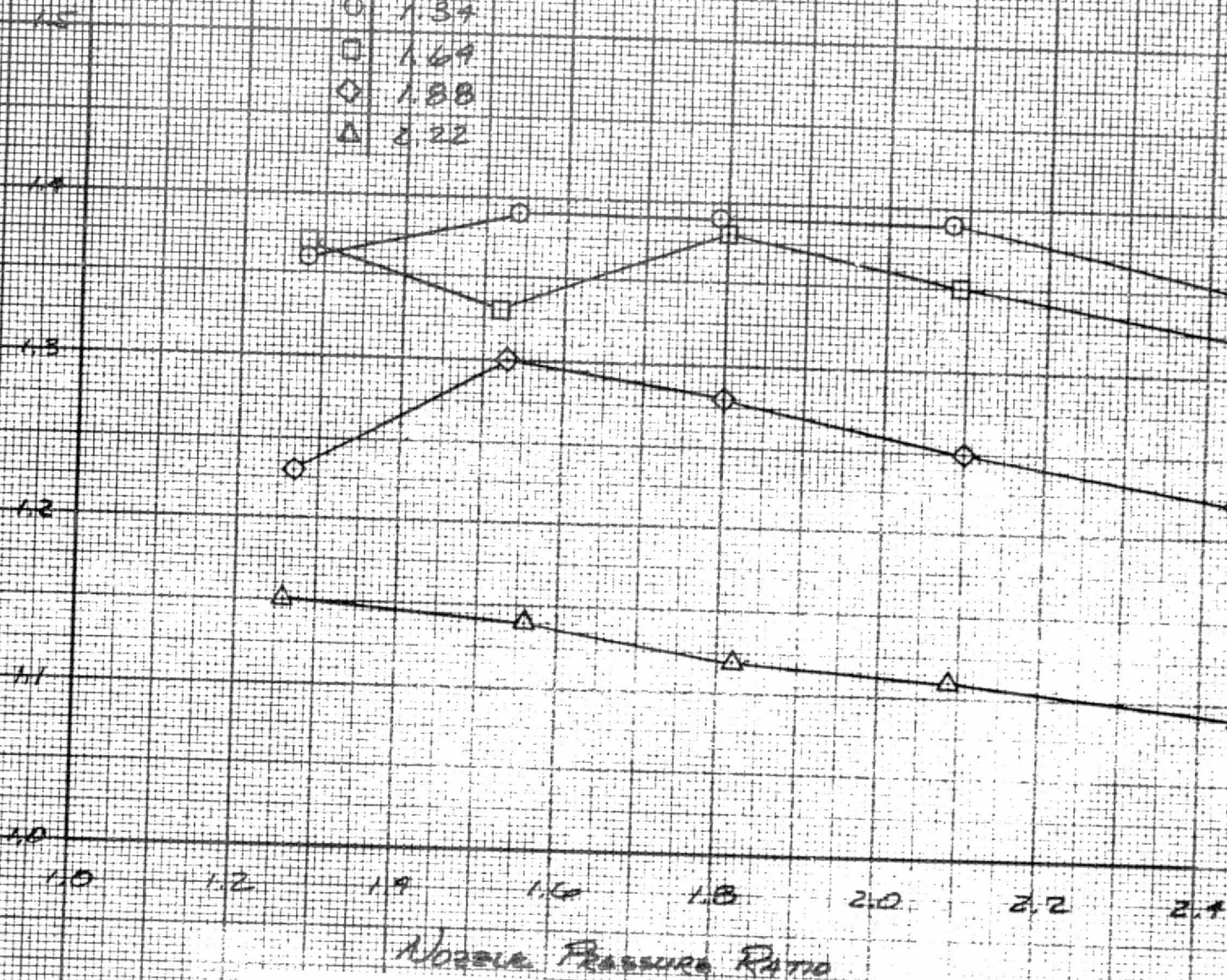
(d) $\delta_f = 60°$.

Figure 7.- Continued.

(e) $\delta_f = 70°$.

Figure 7.- Concluded.

(a) $\delta_f = 20°$.

Figure 8.- The effect of diffuser area ratio on the gross augmentation
ratio, static data, NAR = 11.
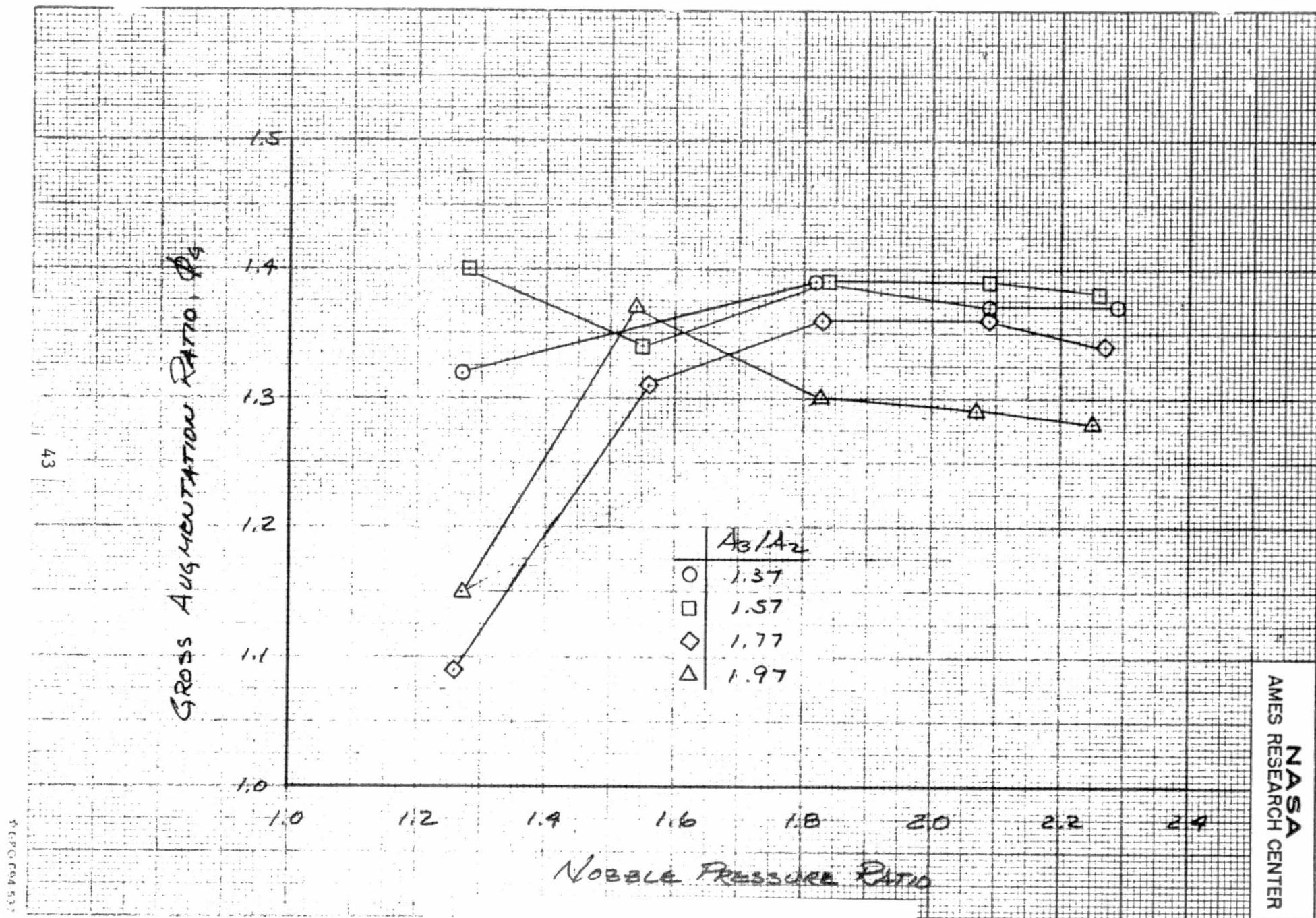
(b) $\delta_f = 30°$.

Figure 8.- Continued.
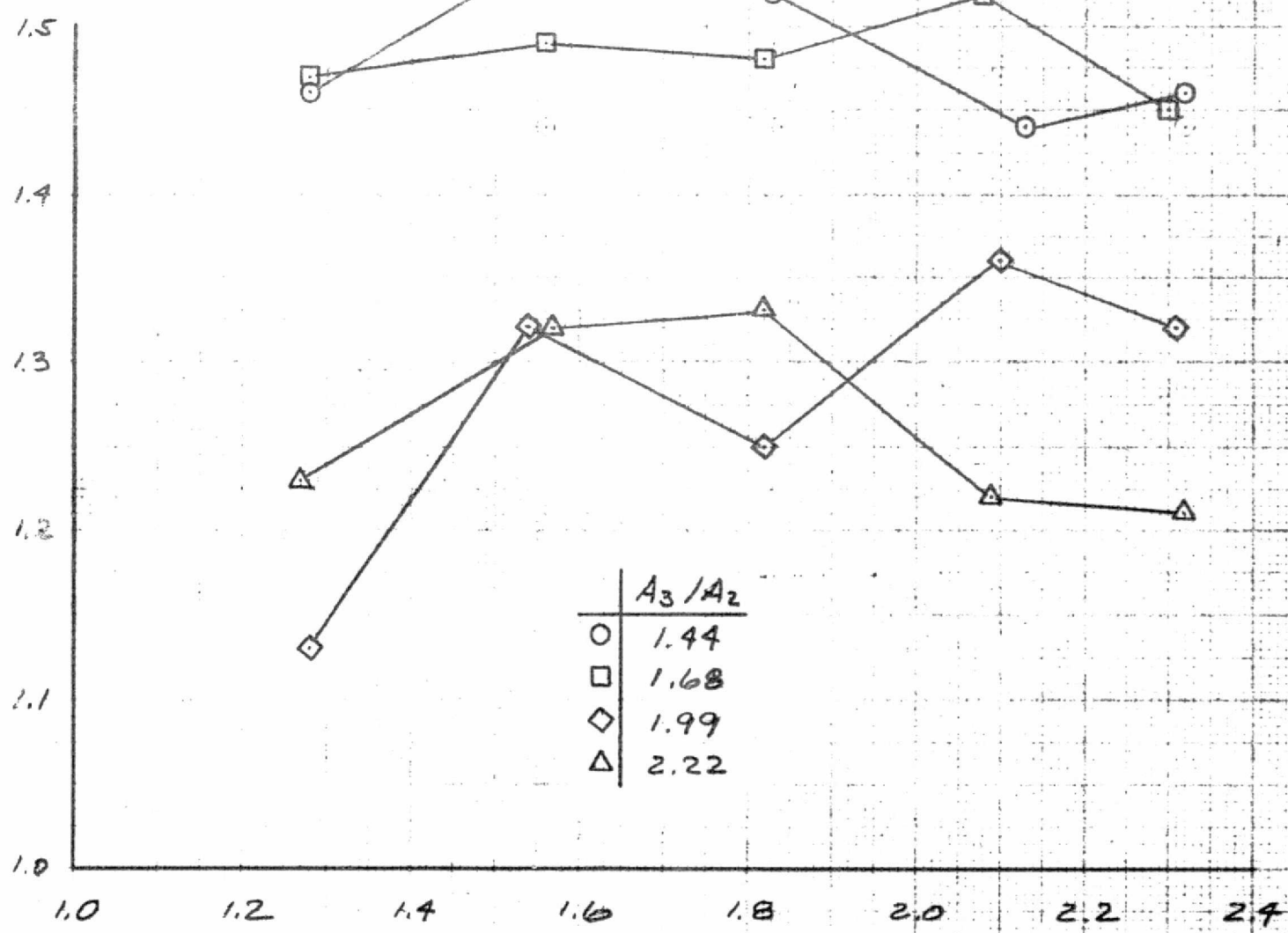
(c) $\delta_f = 45°$.
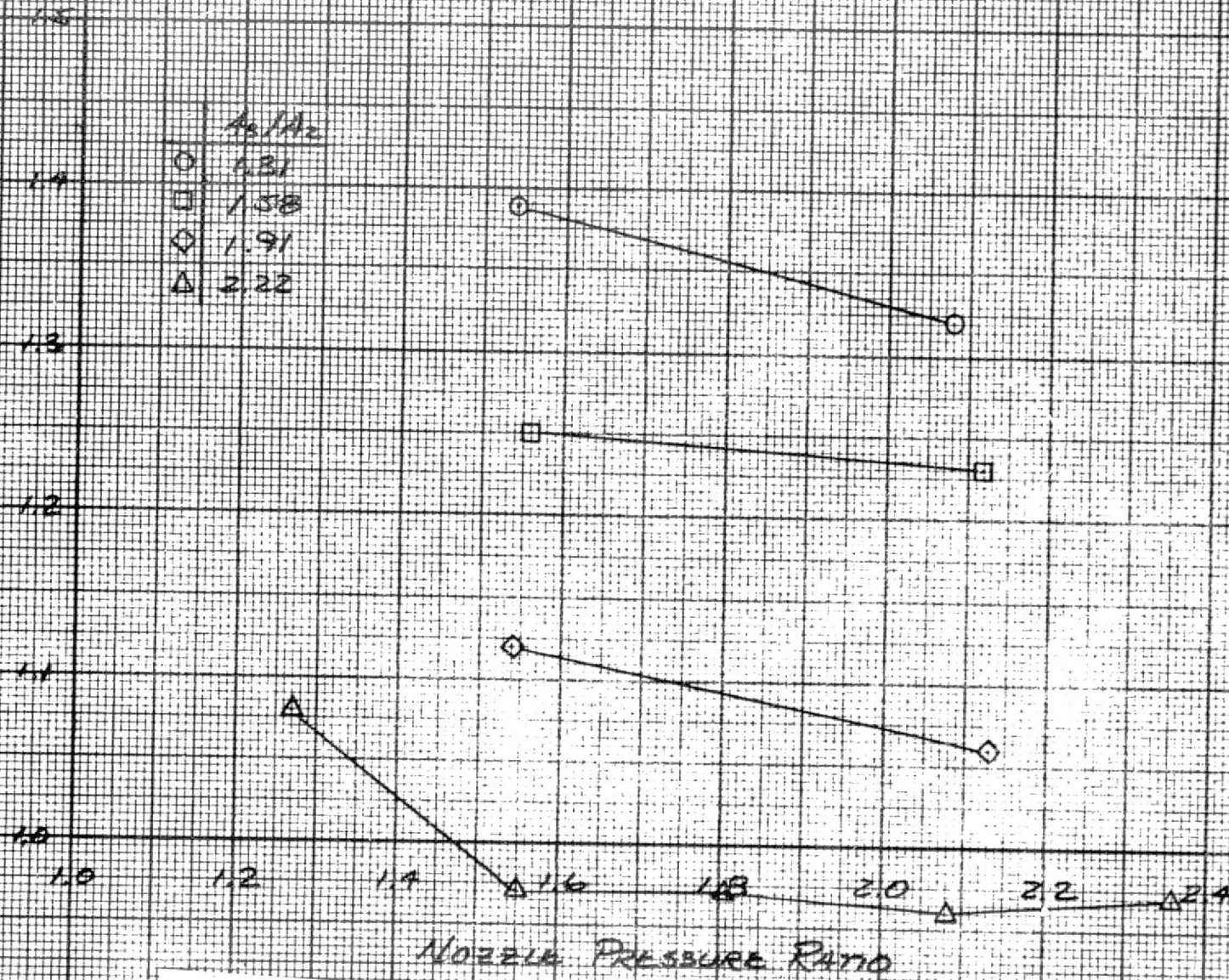
Figure 8.– Continued.

(d) $\delta_f = 60°$.

Figure 8.- Continued.
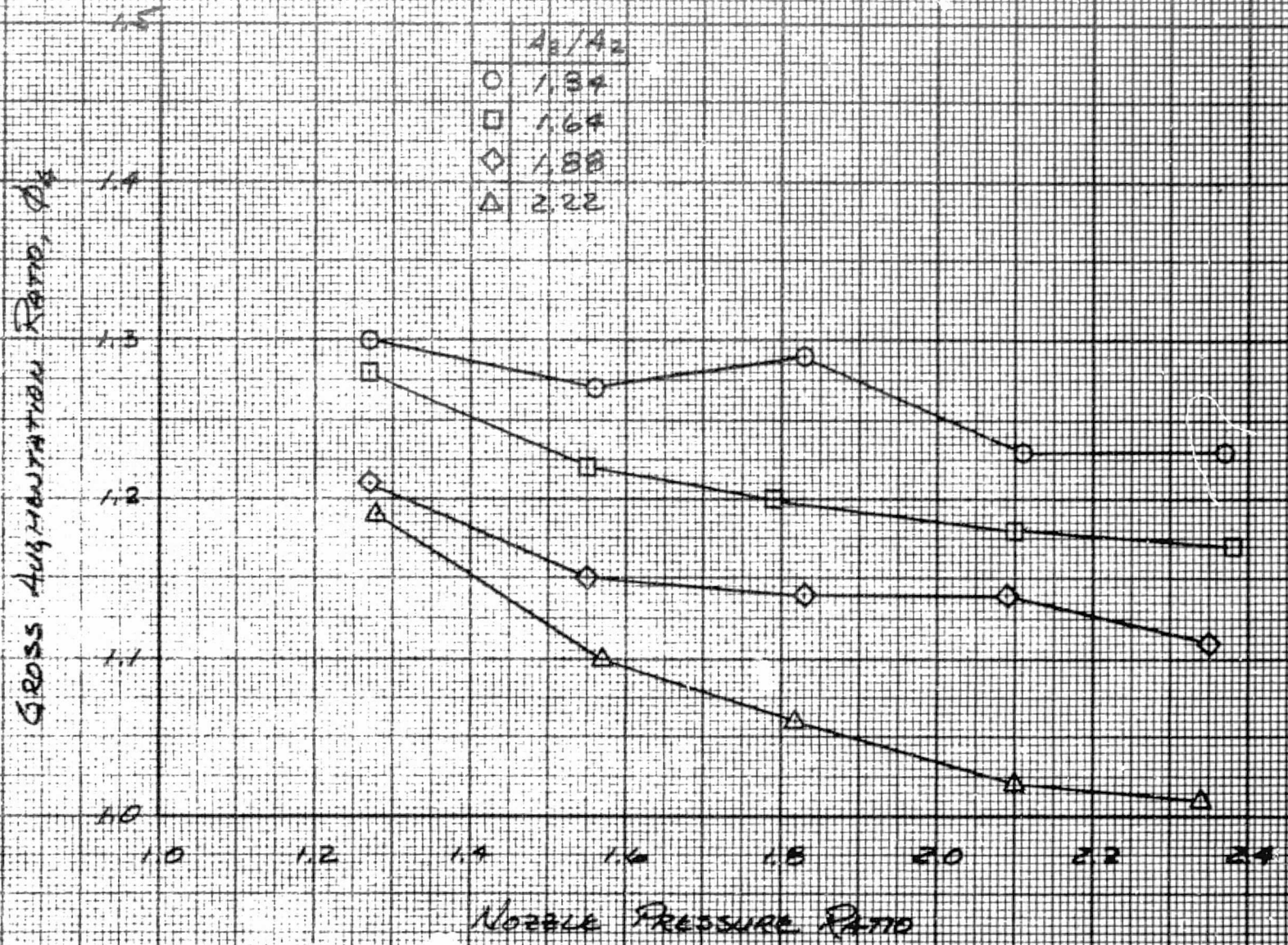
(e) $\delta_f = 70°$.

Figure 8.- Concluded.
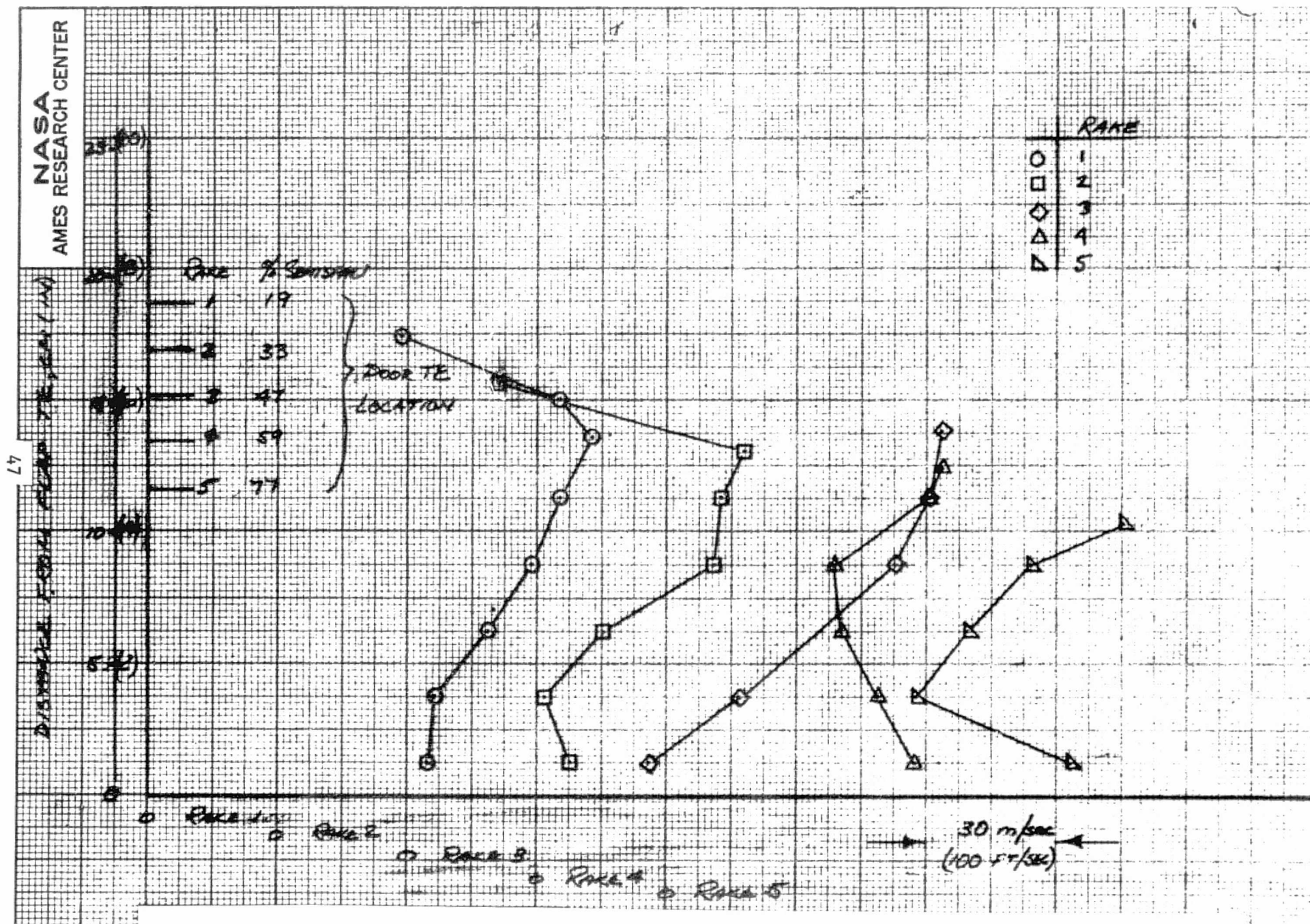
Figure 9.- Augmentor exit velocity profiles at 5 spanwise loactions,
$\delta_f = 20°$, $V_\infty = 0$, $A_3/A_2 = 1.37$, NPR = 2.12, NAR = 5.5.
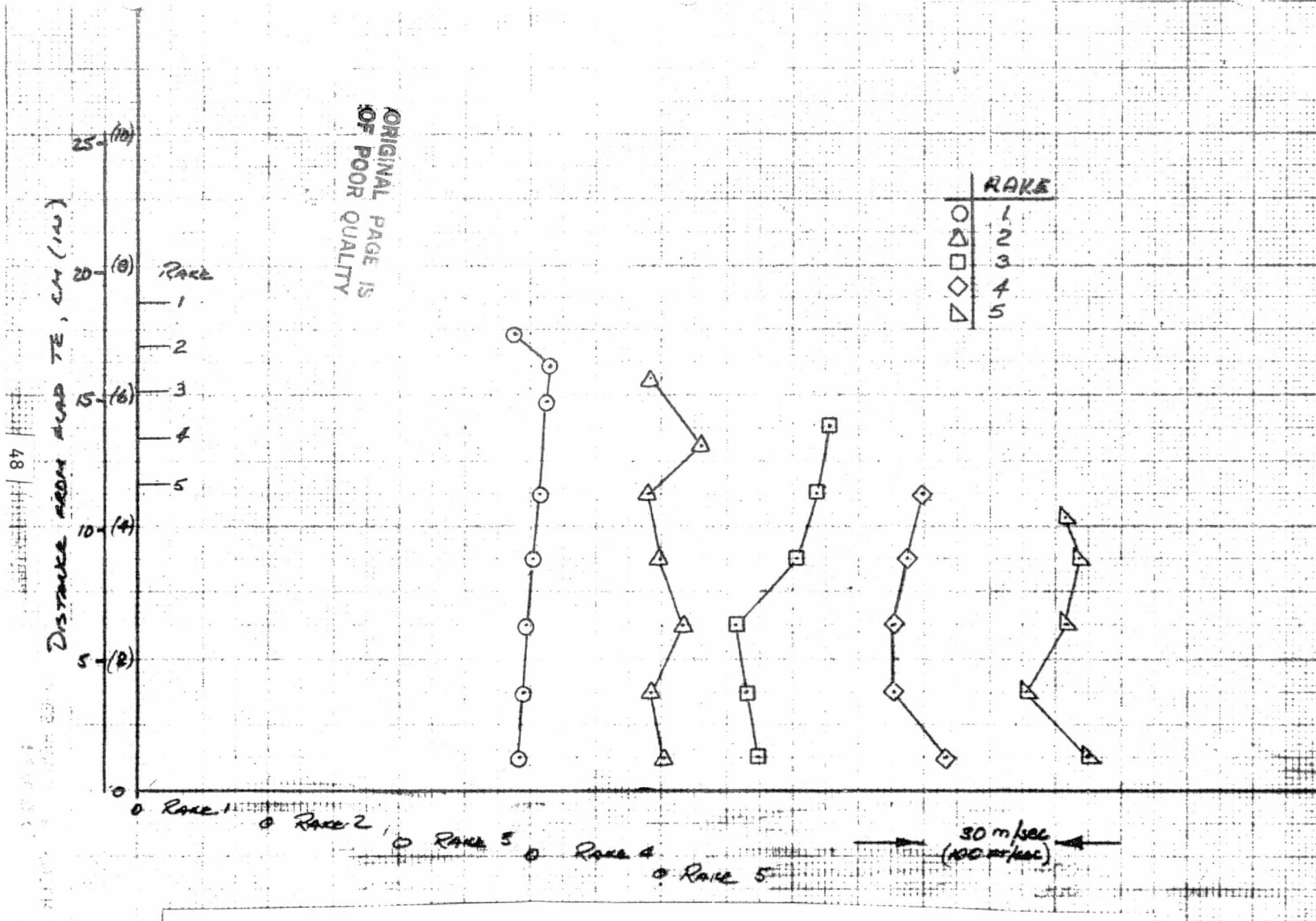
(a) $V_\infty = 0.$

Figure 10.– Augmentor exit velocity profiles at 5 spanwise locations, $\delta_f = 30°$, $A_3/A_2 = 1.37$, NPR = 2.12, NAR = 5.5.
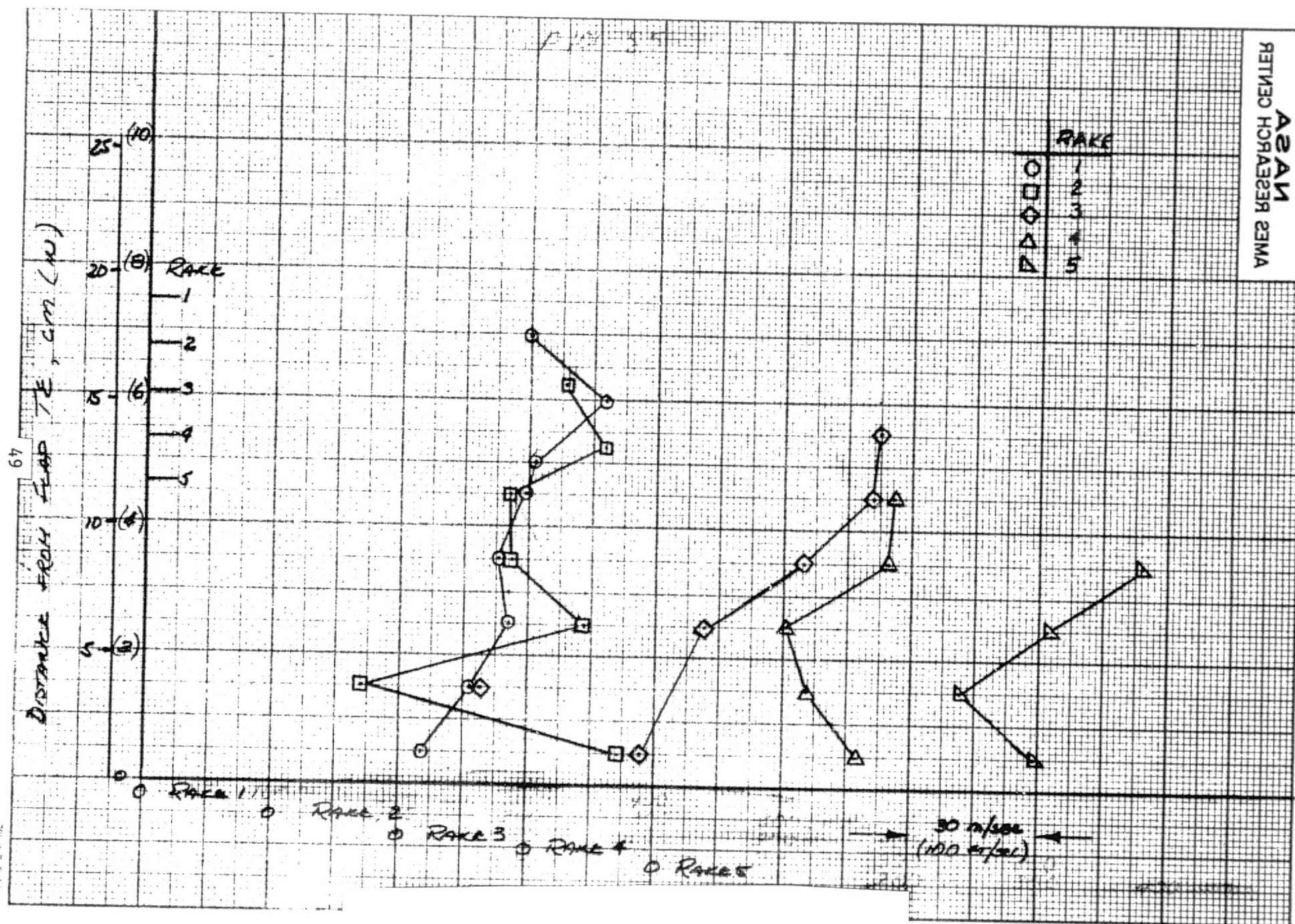
(b) V_∞ = 20 m/sec (65 ft/sec).

Figure 10.- Continued.

(c) V_∞ = 28 m/sec (91 ft/sec).
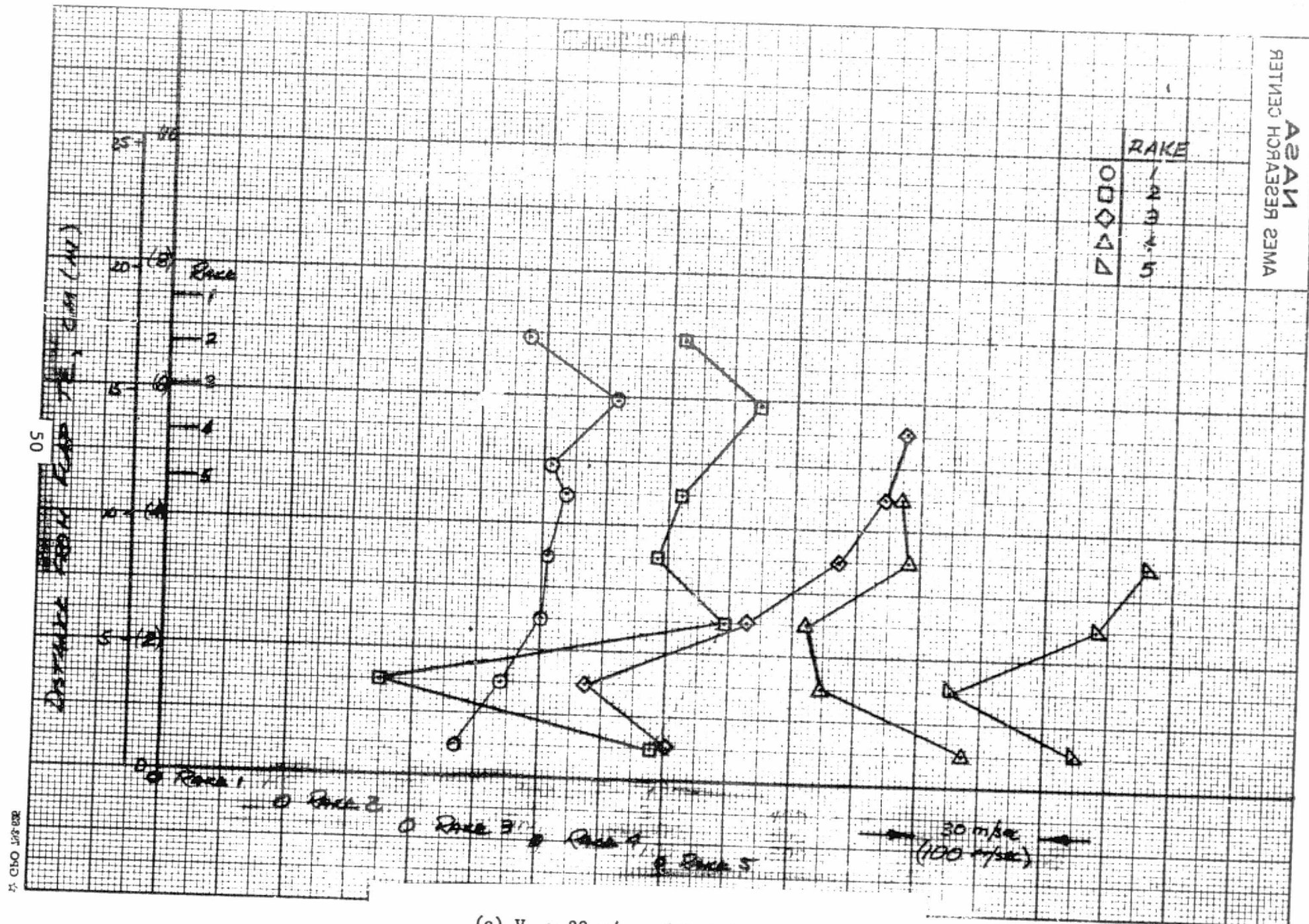
Figure 10.- Continued.
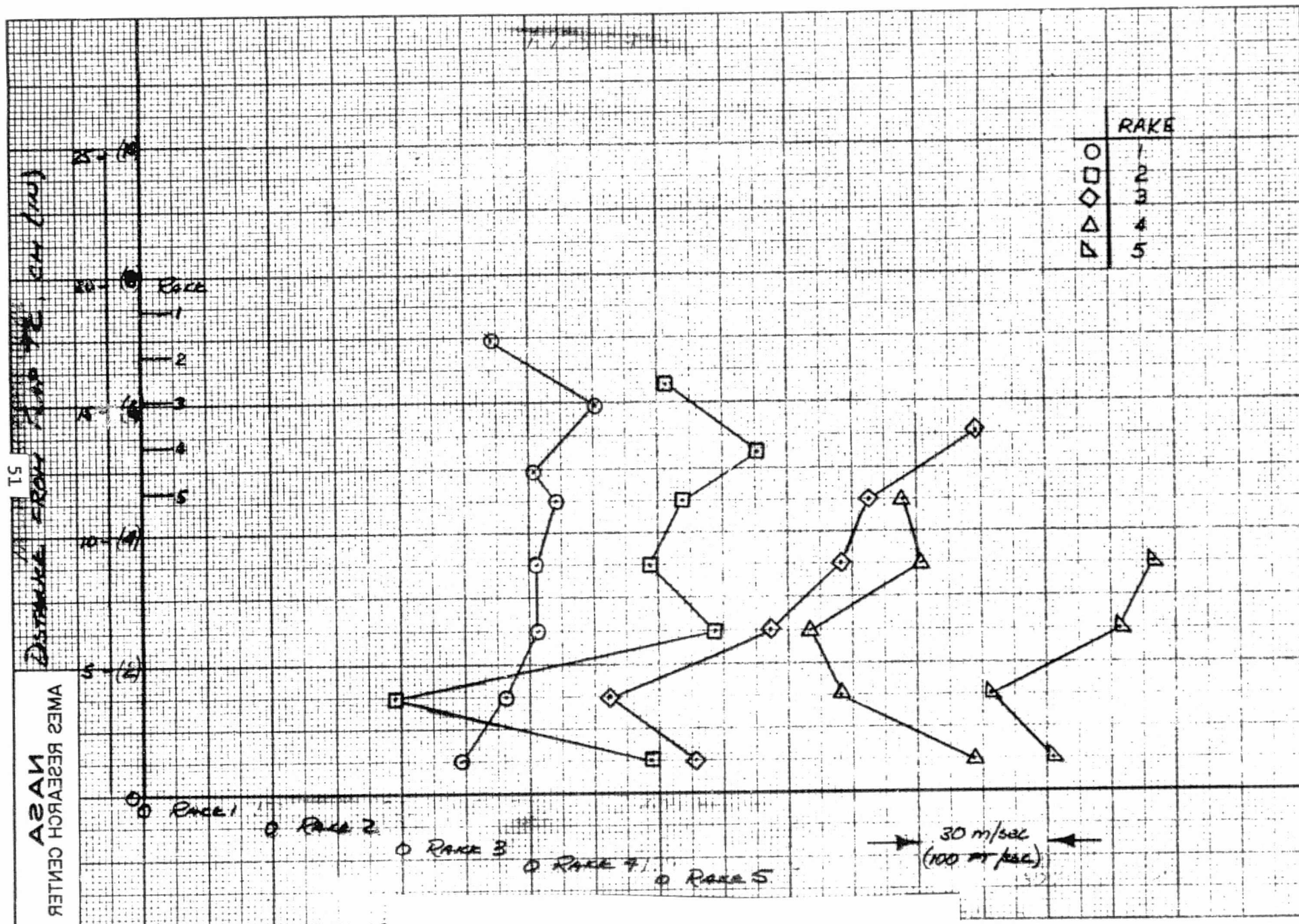
(d) V_∞ = 34 m/sec (11 ft/sec).

Figure 10.- Continued.

(e) V_∞ = 39 m/sec (129 ft/sec).
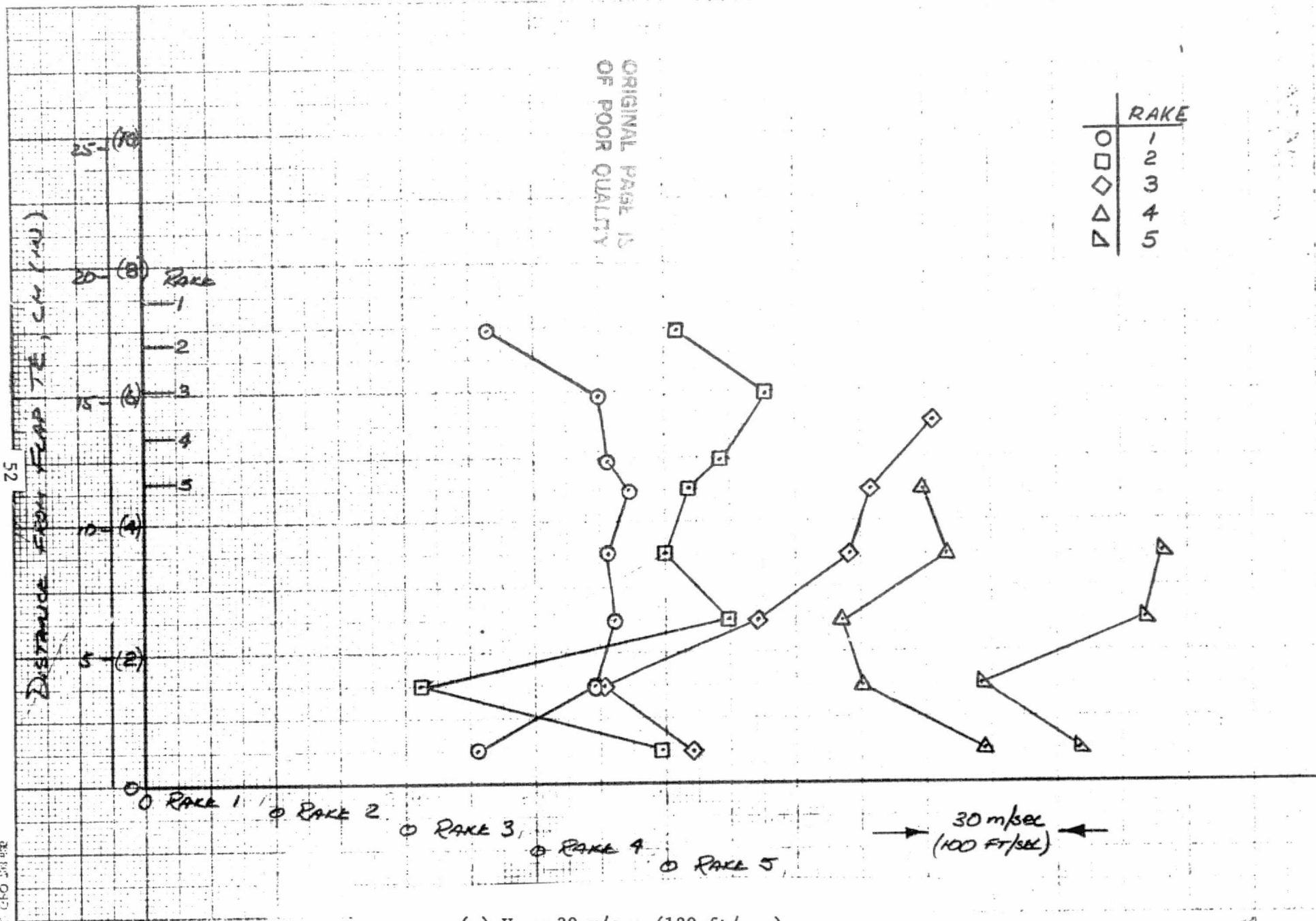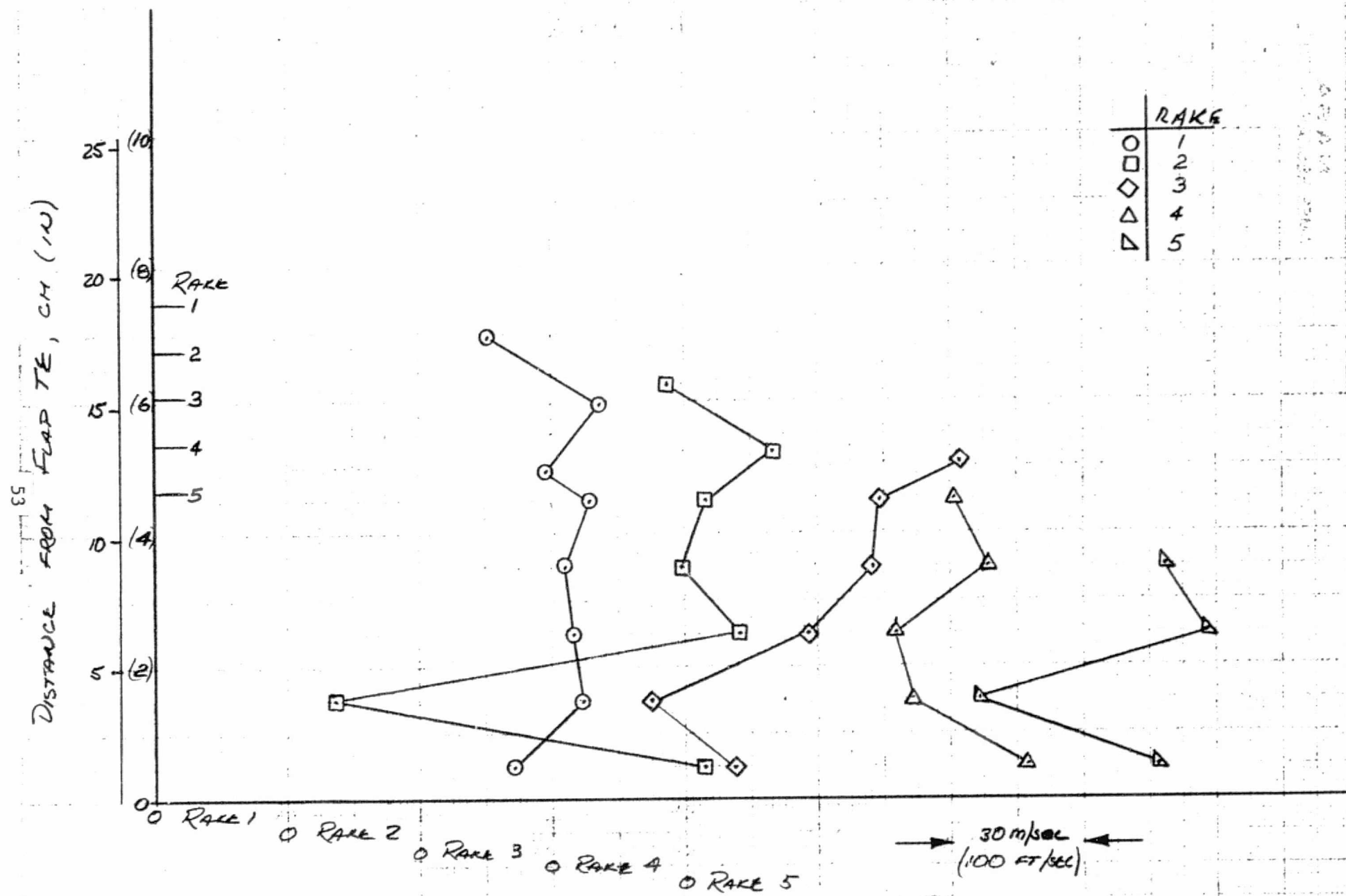
Fig. 10.- Continued.

(f) V_∞ = 48 m/sec (158 ft/sec).

Figure 10.- Continued.
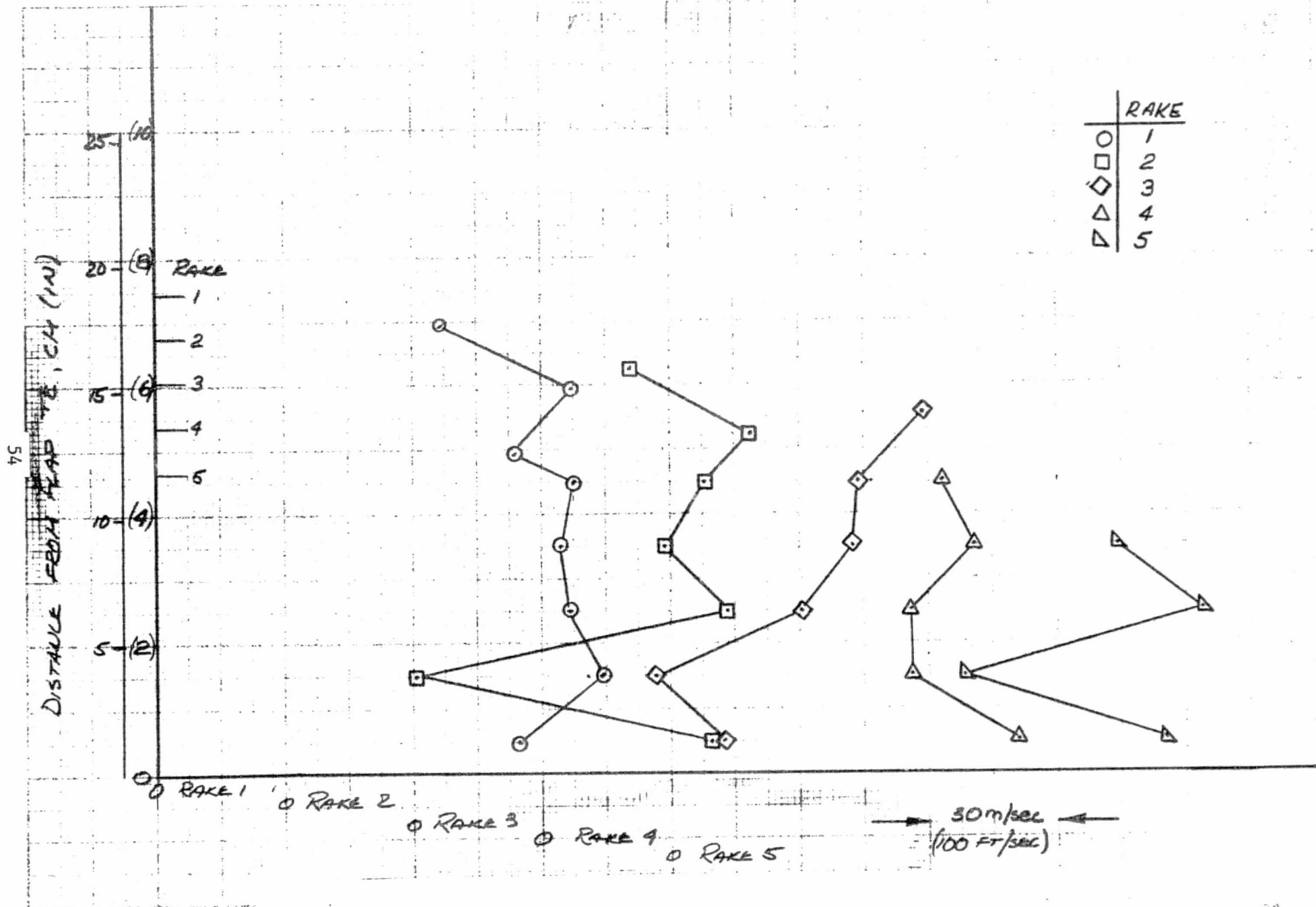
(g) V_∞ = 56 m/sec (183 ft/sec).

Figure 10.- Concluded.
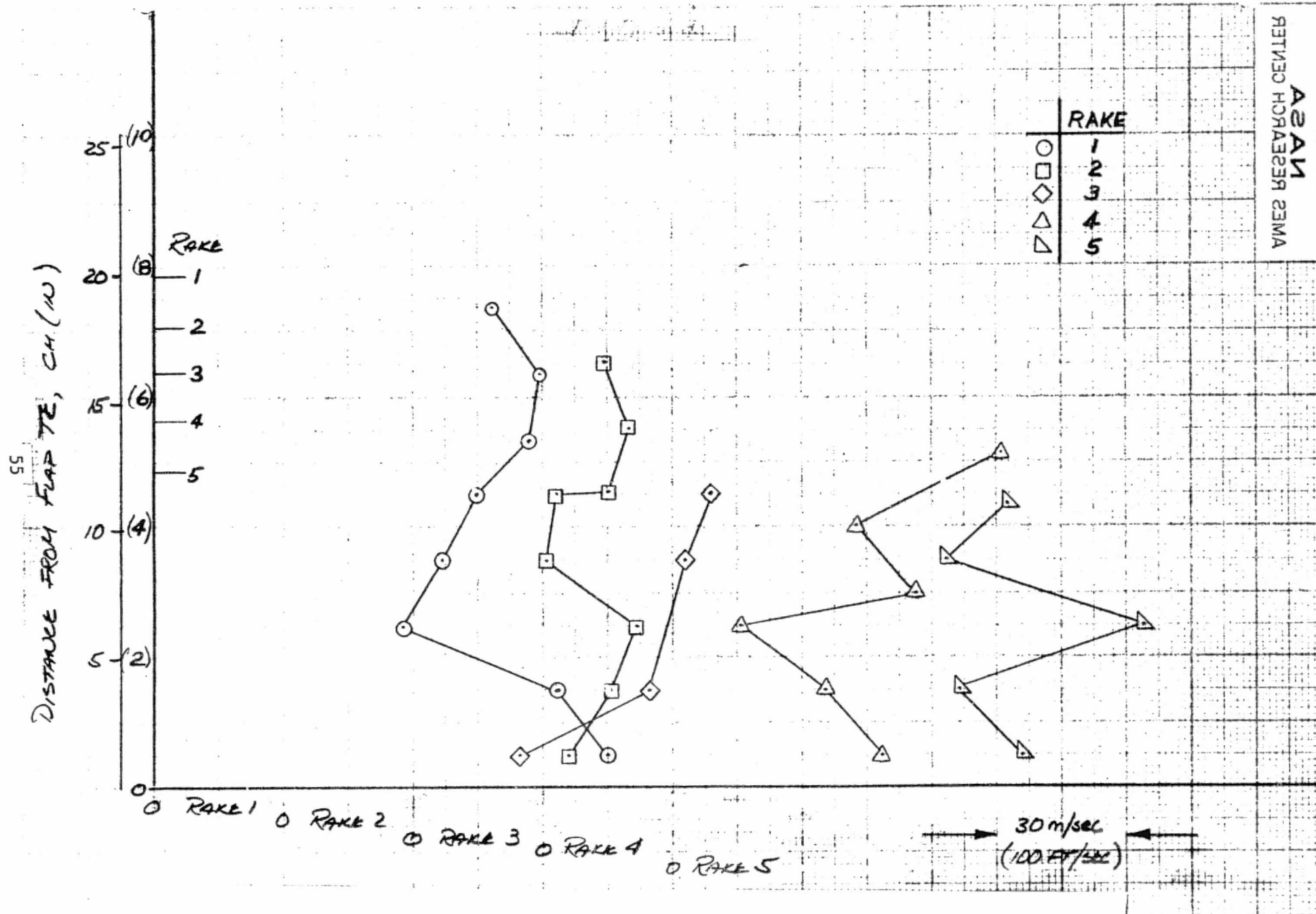
Figure 11.- Augmentor exit velocity profiles at 5 spanwise locations, $\delta_f = 45°$, $V_\infty = 0$, $A_3/A_2 = 1.44$, NPR = 2.10, NAR = 5.5.
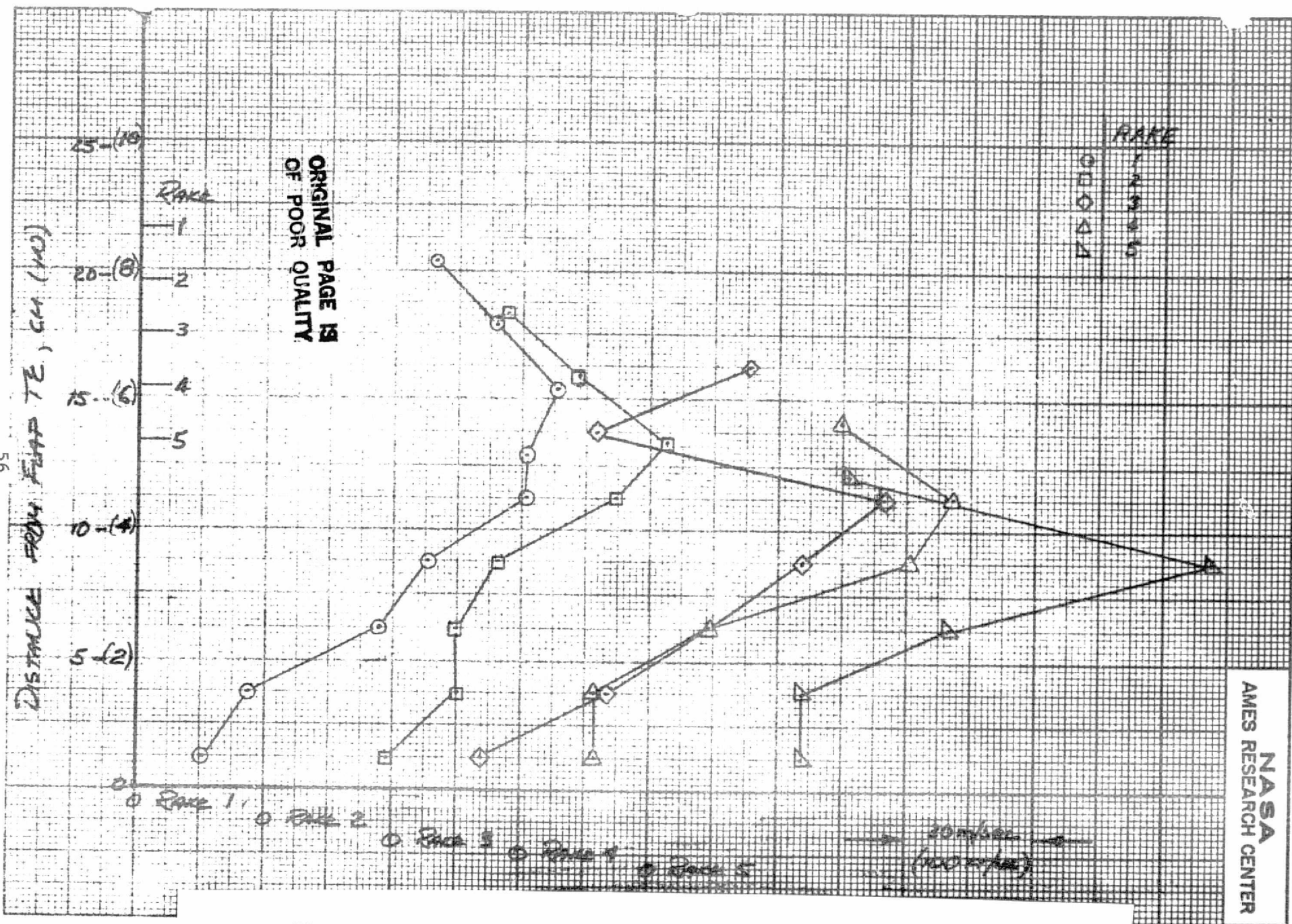
Figure 12.- Augmentor exit velocity profiles at 5 spanwise loactions,
$\delta_f = 60^c$, $V_\infty = 0$, $A_3/A_2 = 1.58$, NPR = 2.10, NAR = 5.5.
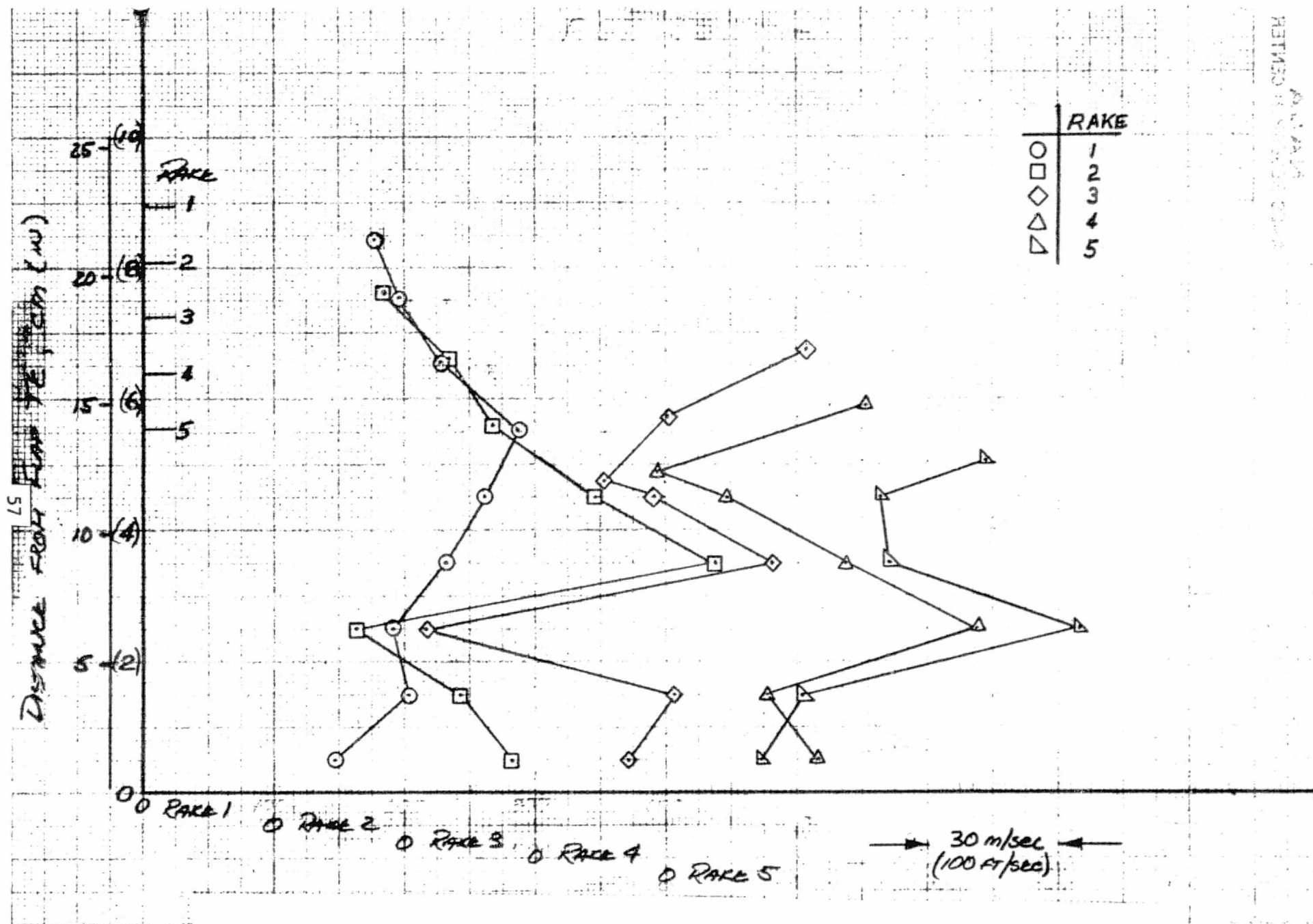
Figure 13.- Augmentor exit velocity profiles at 5 spanwise locations, $\delta_f = 70°$, $V_\infty = 0$, $A_3/A_2 = 1.64$, NPR = 1.94, NAR = 5.5.
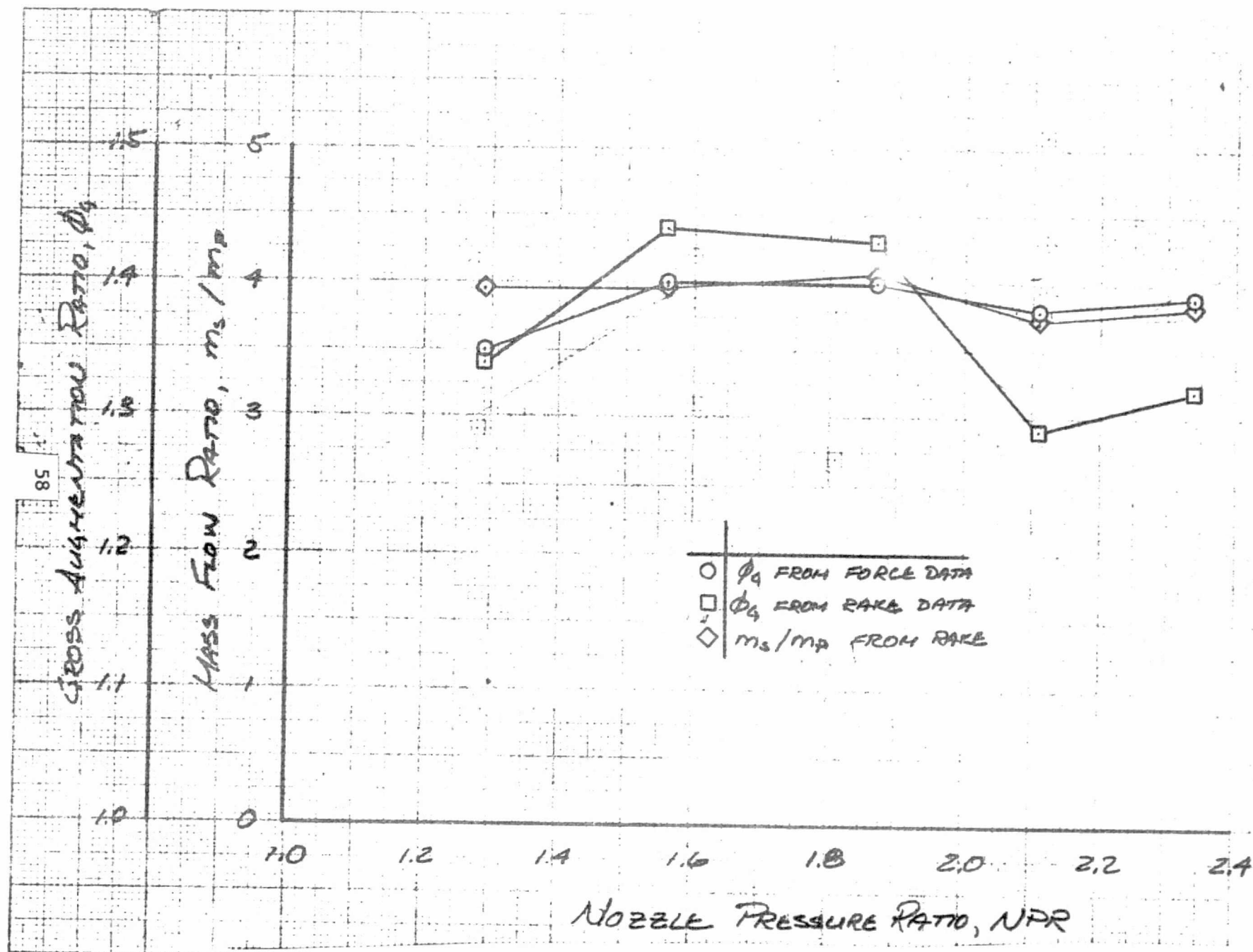
Figure 14.– Gross augmentation ratio and mass flow ratio characteristics
at $\delta_f = 30°$, $A_3/A_2 = 1.37$, $V_\infty = 0$.
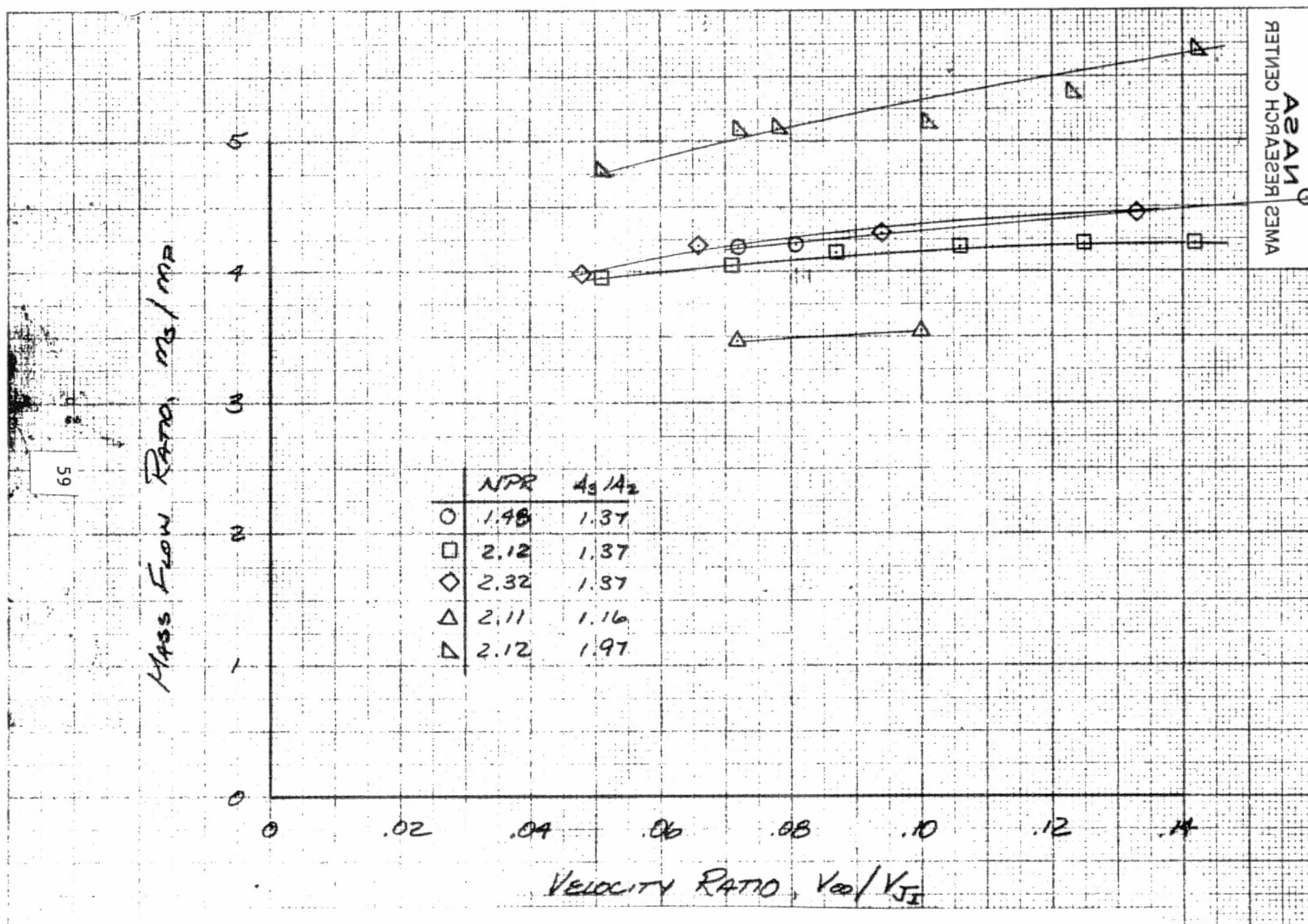
Figure 15.- The effect of velocity ratio on mass flow ratio, $\delta_f = 30°$.
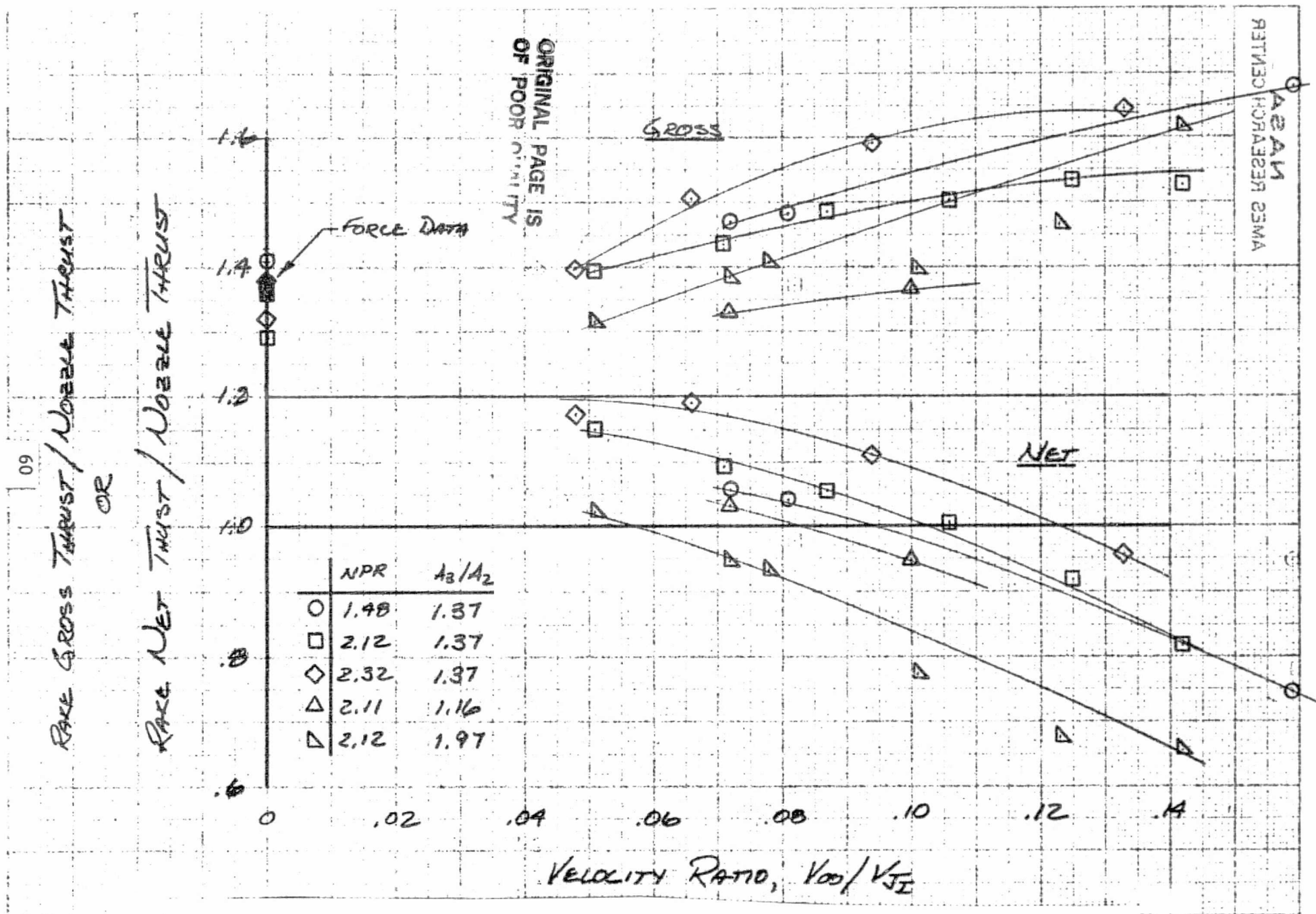
Figure 16.- The effect of velocity ratio on the gross and net thrust ratios, $\delta_f = 30°$.

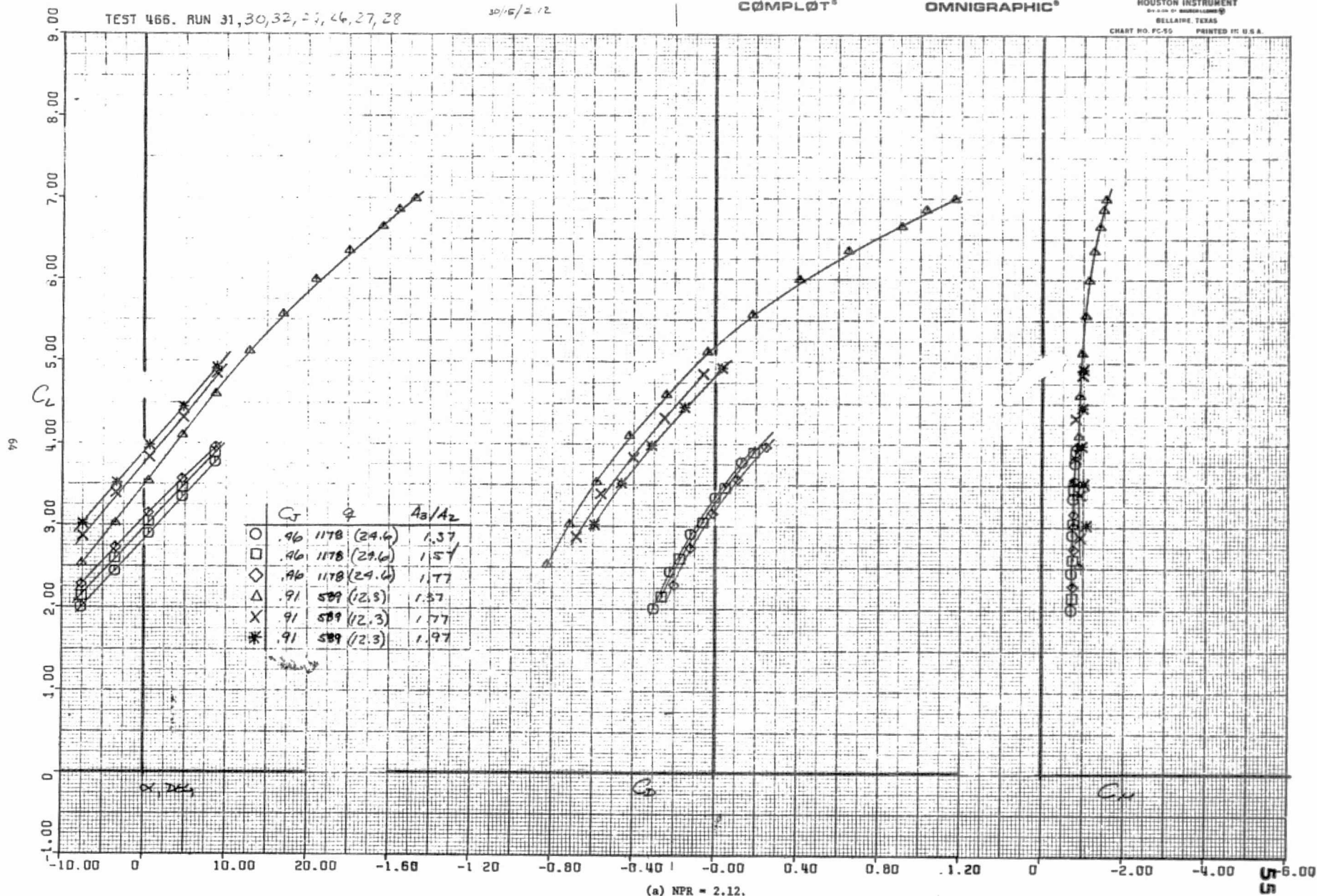| C_J	q	A_3/A_2
○	.46	1173 (24.5)	1.37
□	.46	1173 (24.5)	1.94
◇	.91	589 (12.3)	1.37
△	.91	589 (12.3)	1.66
⬡	.91	589 (12.3)	1.94

(a) NPR = 2.12.
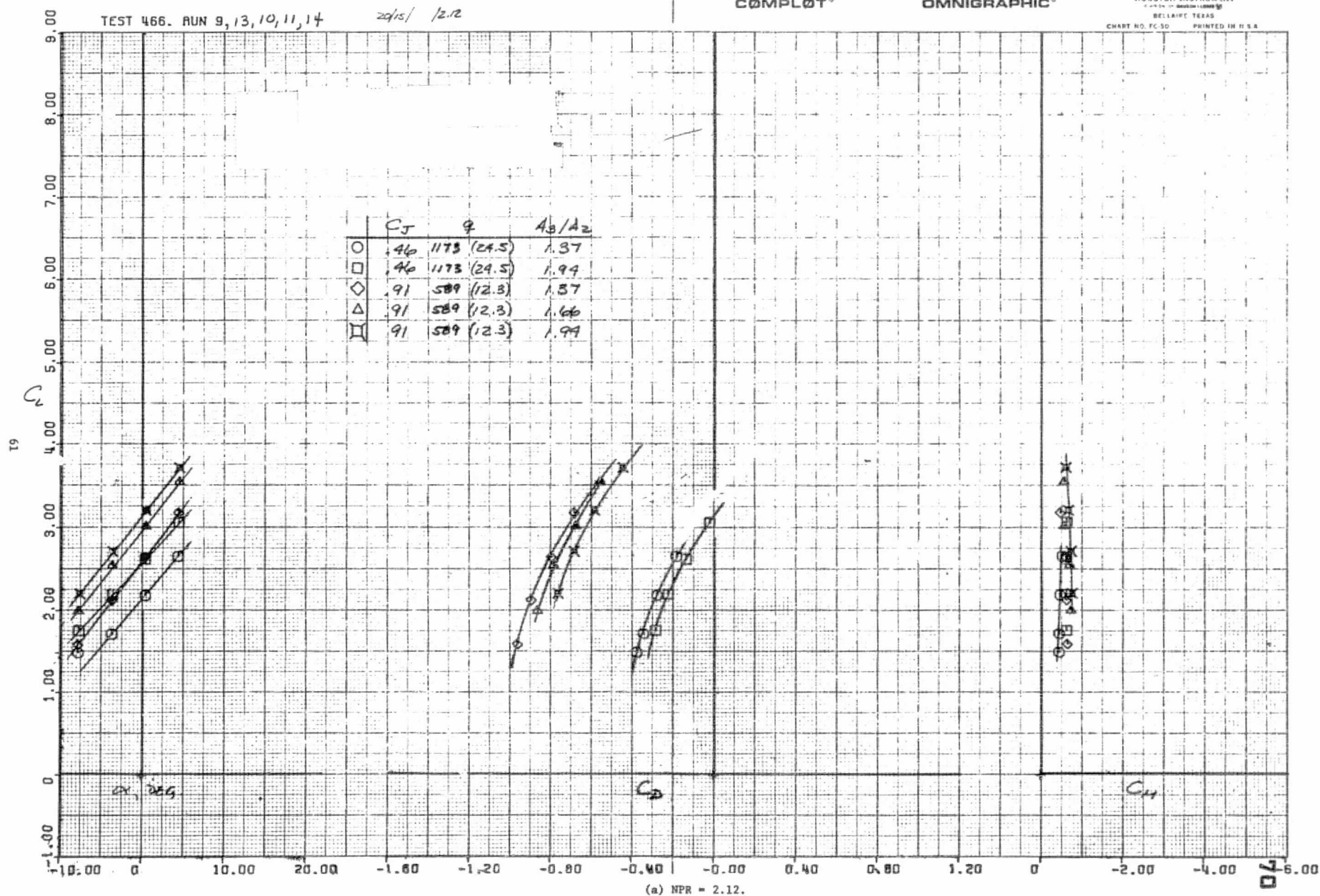
Figure 17.- The effect of C_γ on the longitudinal characteristics of the model, $\delta_f = 20°$.

(b) NPR = 1.48, A_3/A_2 = 1.37.

Figure 17.– Continued.

(c) q = 455 N/m² (9.5 lb/ft²).

Figure 17.- Concluded.

C_J	ϕ	A_3/A_2
○	.96	1178 (24.6)	1.37
□	.96	1178 (24.6)	1.57
◇	.96	1178 (24.6)	1.77
△	.91	589 (12.3)	1.57
✕	.91	589 (12.3)	1.77
✳	.91	589 (12.3)	1.97

(a) NPR = 2.12.
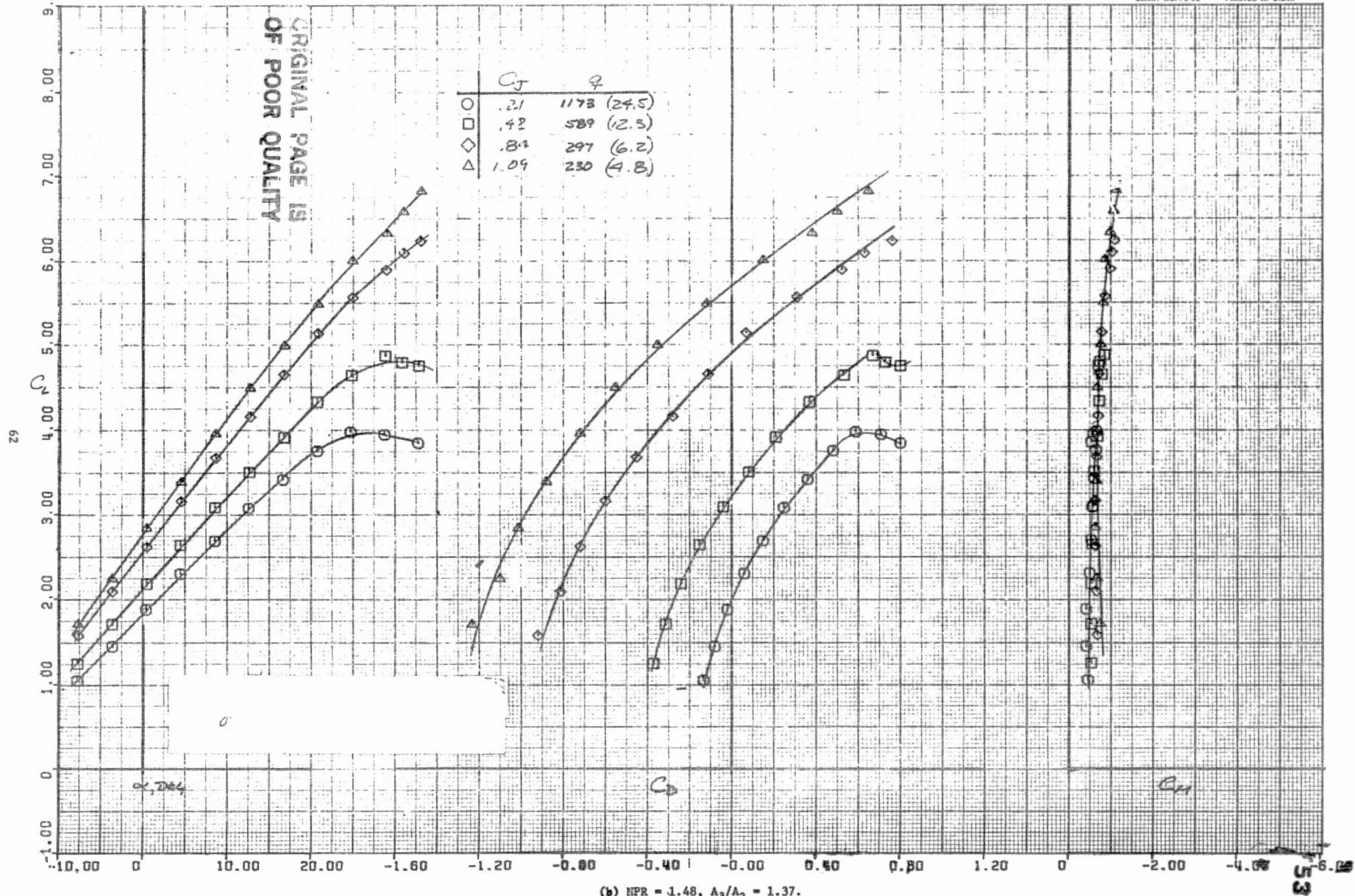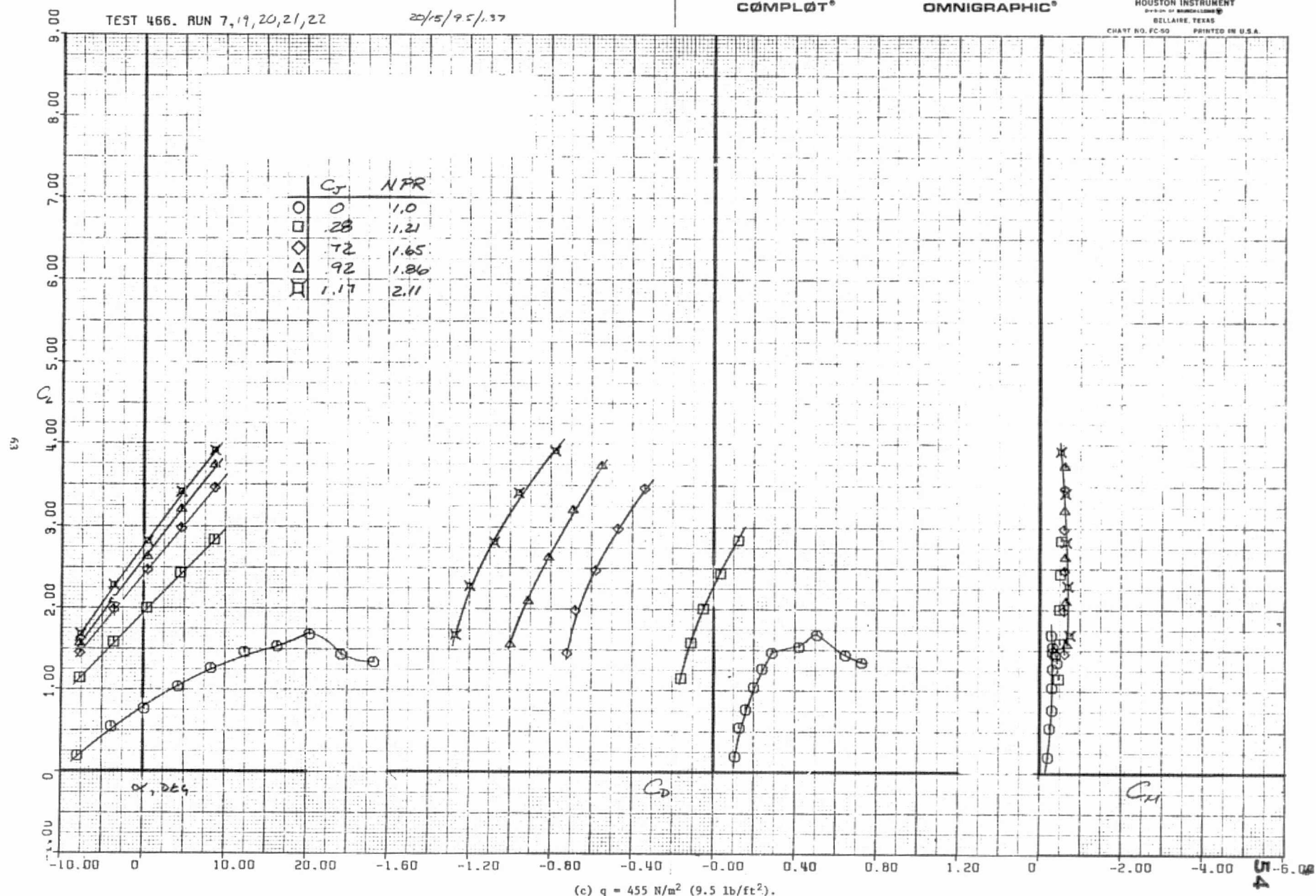
Figure 18.- The effect of C_J on the longitudinal characteristics of the model, $\delta_f = 30°$.
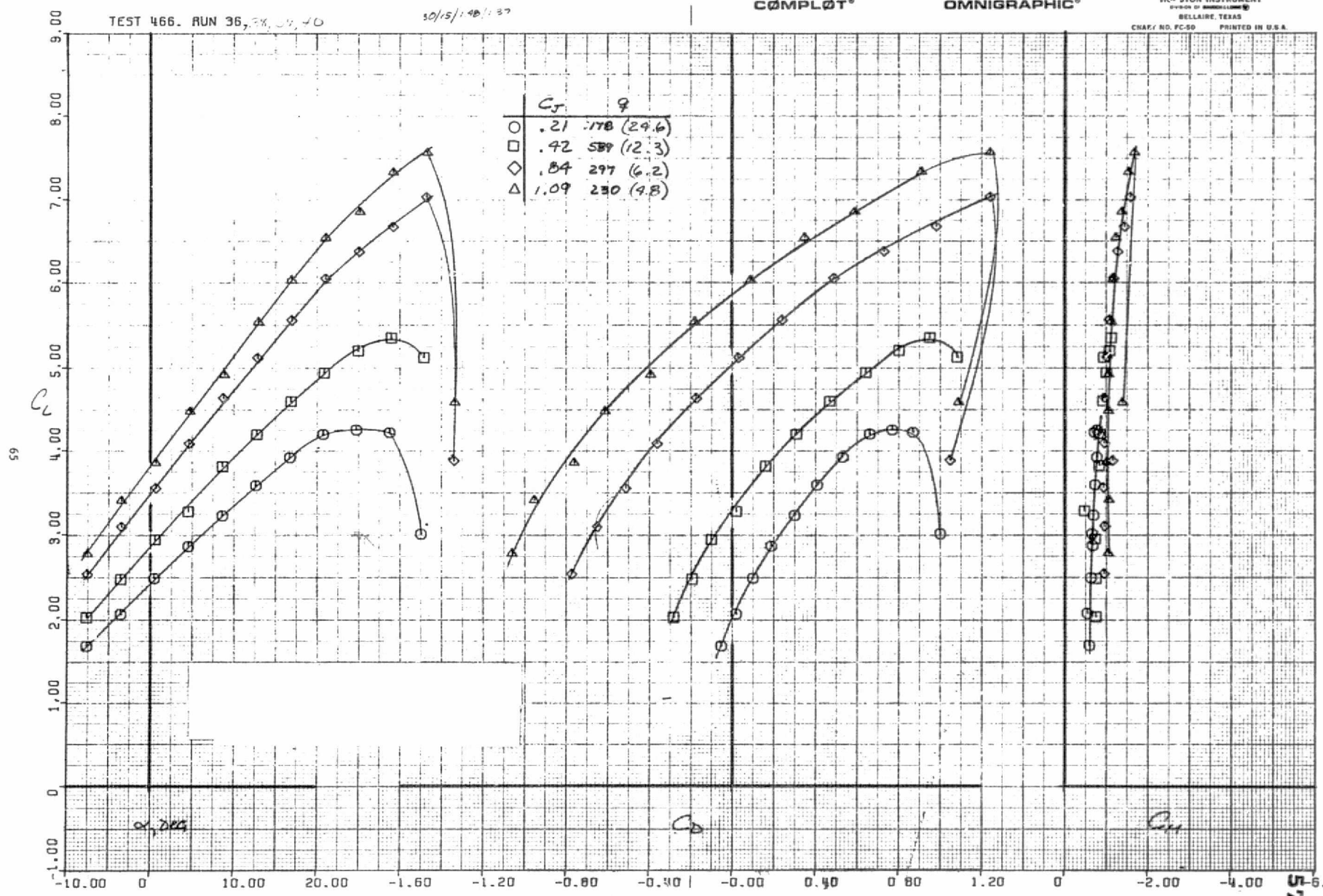
C_J	φ
○ .21	1178 (24.6)
□ .42	589 (12.3)
◇ .84	297 (6.2)
△ 1.09	230 (4.8)

(b) NPR = 1.48, A_3/A_2 = 1.37.

Figure 18.— Continued.
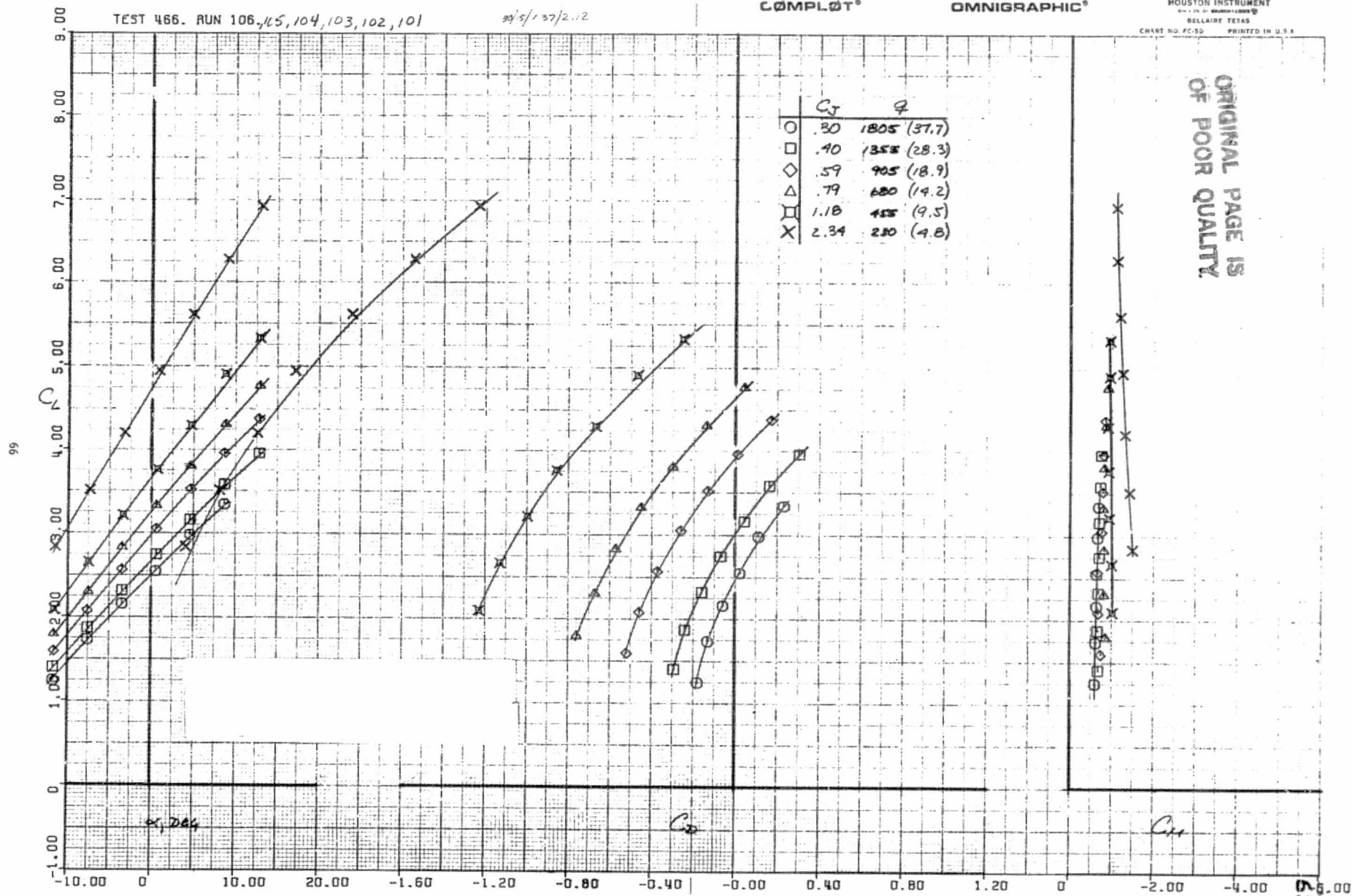
(c) NPR = 2.12, A_3/A_2 = 1.37.

Figure 18.- Continued.
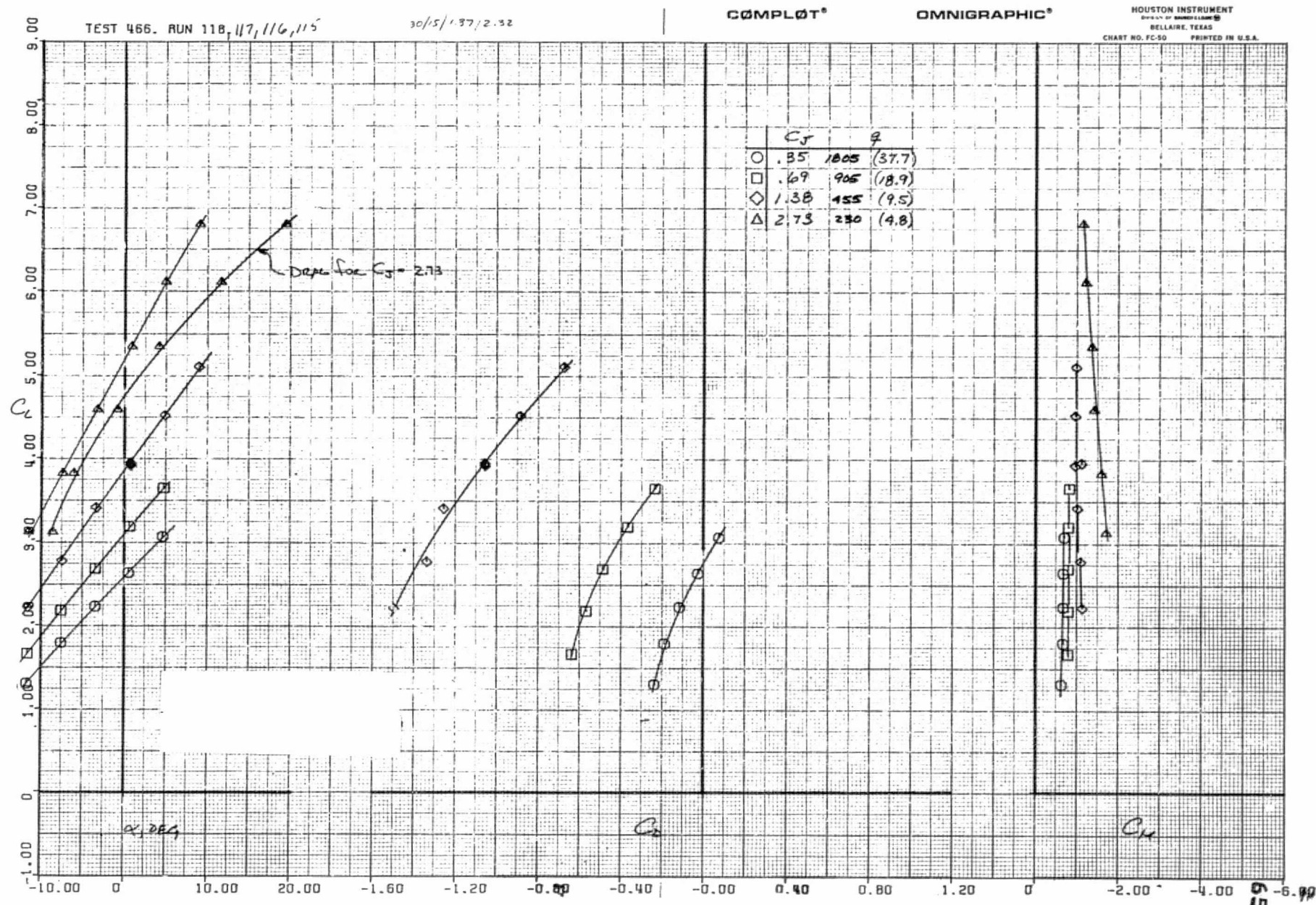
(d) NPR = 2.32, A_3/A_2 = 1.37.

Figure 18.- Continued.

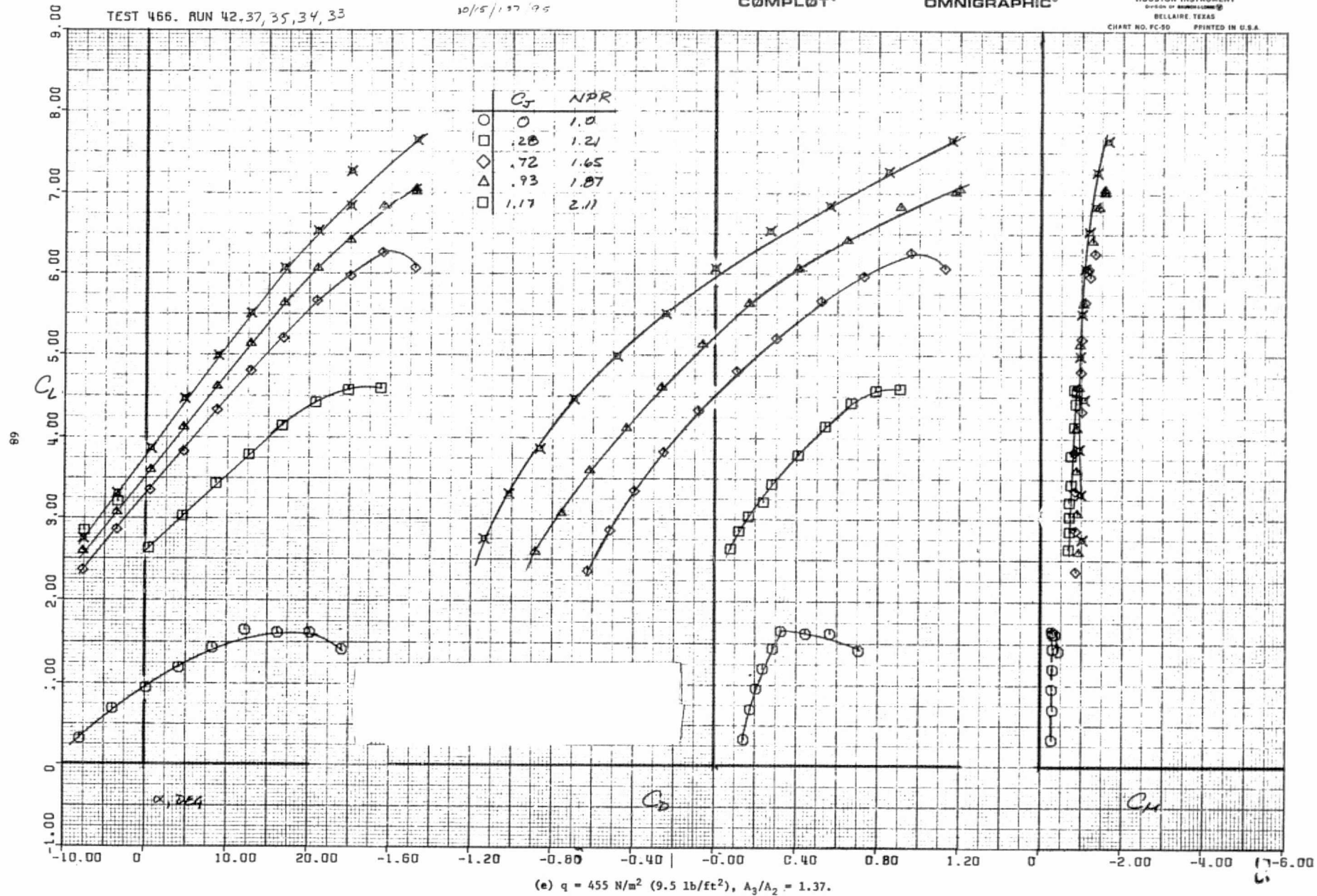(e) q = 455 N/m^2 (9.5 lb/ft^2), A$_3$/A$_2$ = 1.37.

Figure 18.- Continued.
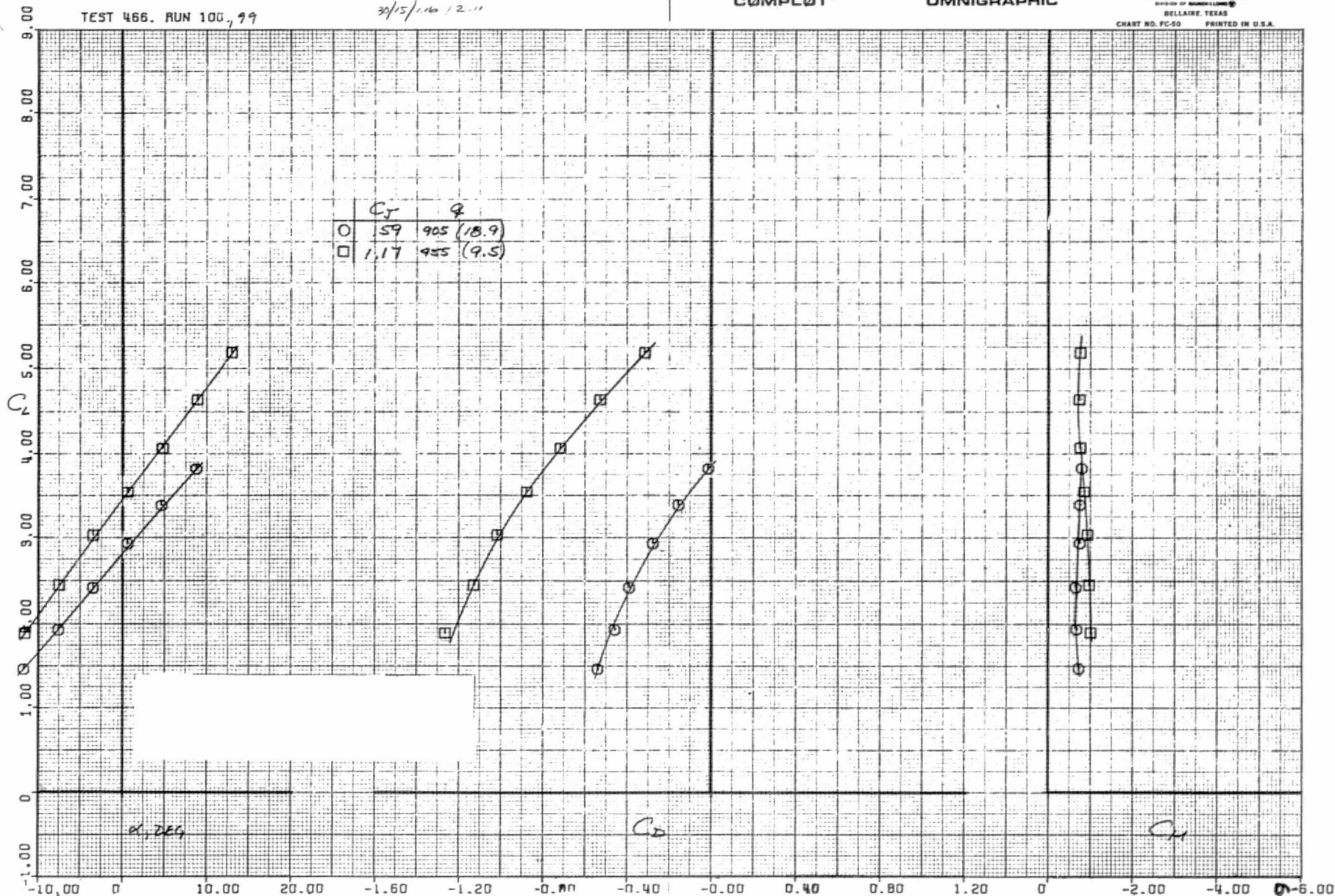
(f) NPR = 2.11, A_3/A_2 = 1.16.

Figure 18.- Continued.
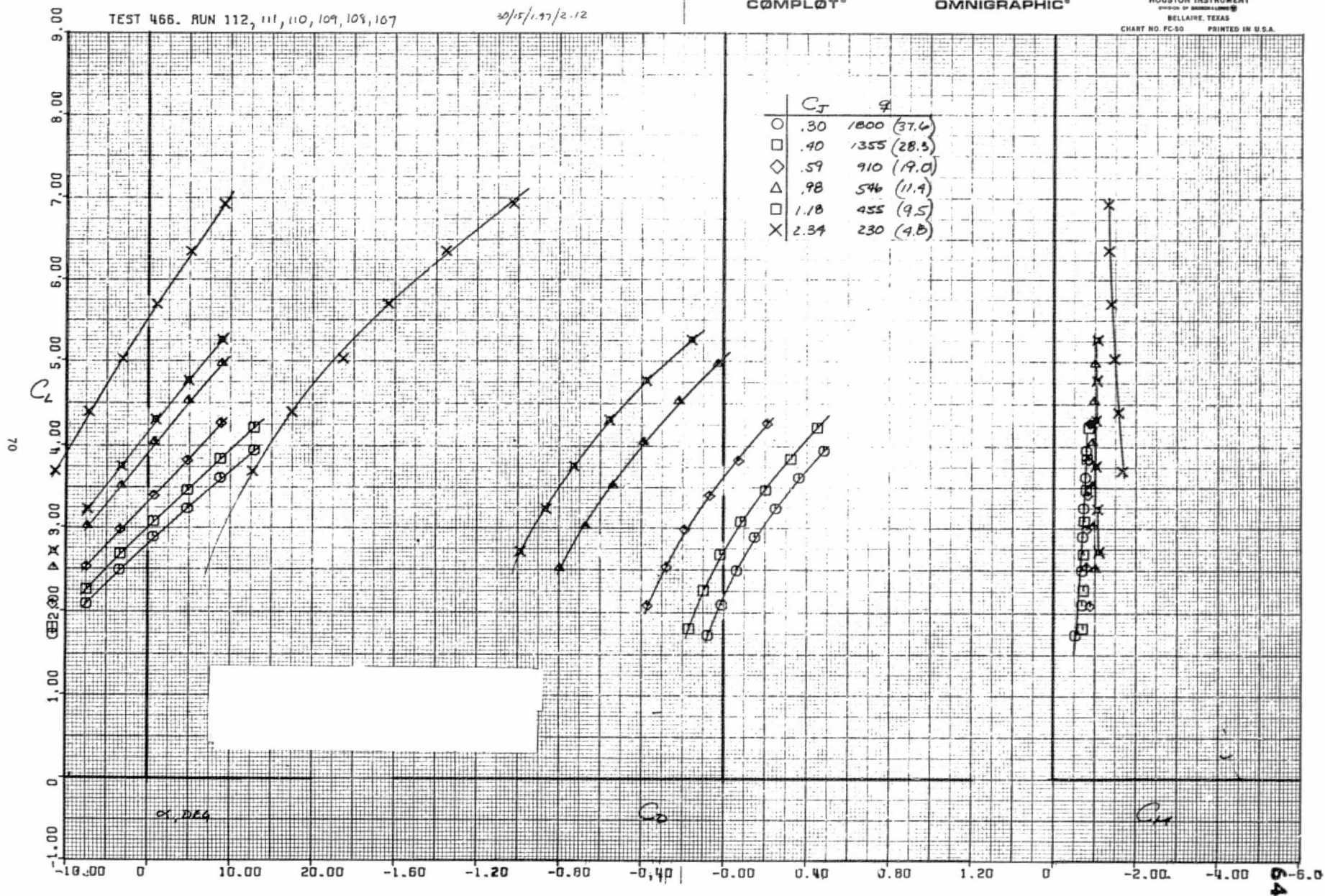
(g) NPR = 2.12, A_3/A_2 = 1.97.

Figure 18.- Concluded.

(a) NPR = 2.12.
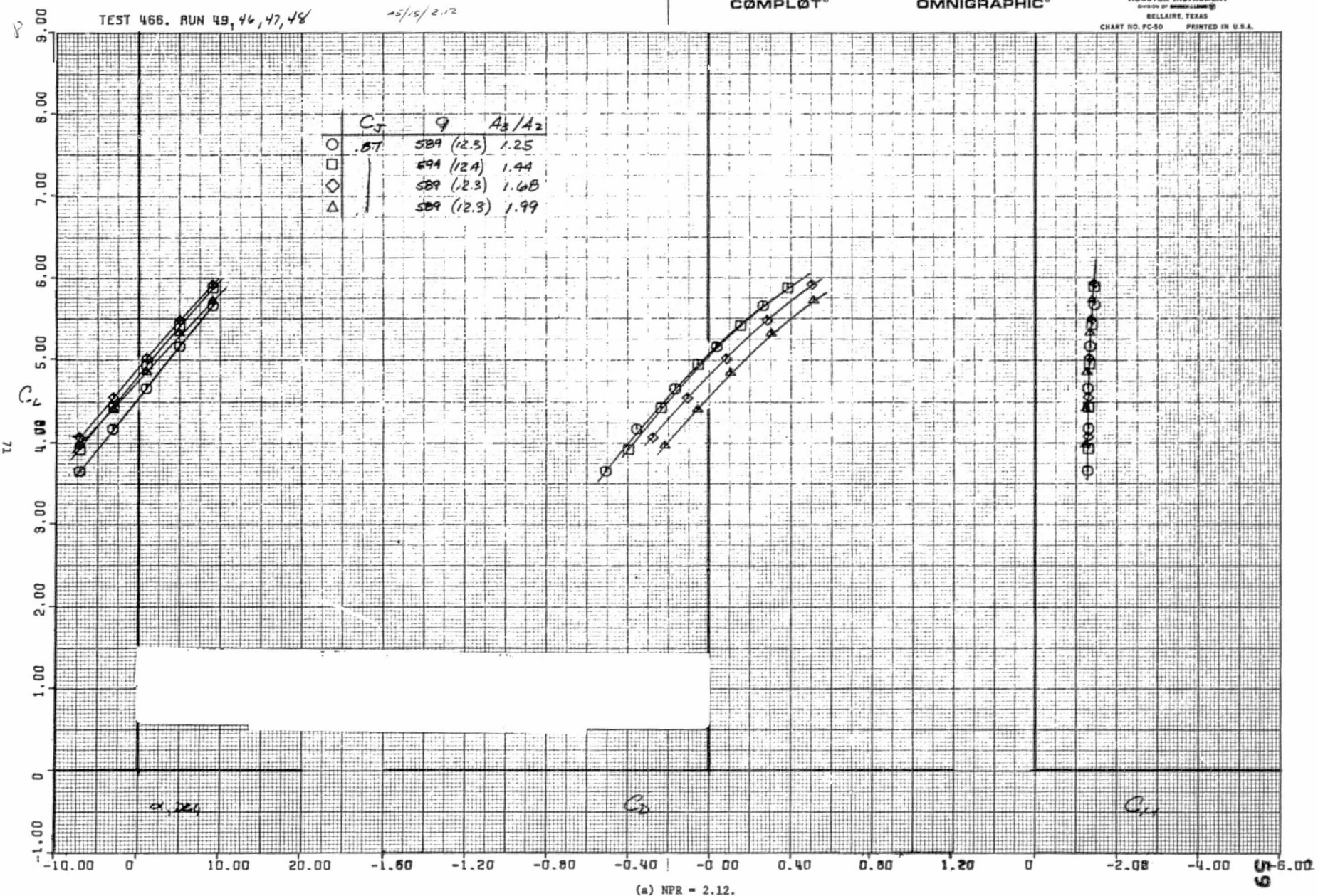
Figure 19.- The effect of C_J on the longitudinal characteristics of
the model, $\delta_f = 45°$

(b) NPR = 1.49, A_3/A_2 = 1.44.

Figure 19.- Continued.

COMPLØT®   OMNIGRAPHIC®   HOUSTON INSTRUMENT
BELLAIRE, TEXAS
CHART NO. FC-50   PRINTED IN U.S.A.

C_J	NPR
○ 0	1.0
□ .29	1.21
◇ .70	1.67
△ .90	1.88
⬡ 1.13	2.12

(c) $q = 455$ N/m² (9.5 lb/ft²), $A_3/A_2 = 1.44$.

Figure 19.- Concluded.

	C_J	q	A_8/A_2
○	.46	1173 (24.5)	1.31
□	.46	1173 (24.5)	1.58
◇	.46	1173 (24.5)	1.91
△	.92	589 (12.3)	1.31
⬡	.92	589 (12.3)	1.58
✕	.92	589 (12.3)	1.91
✳	.92	589 (12.3)	2.22

(a) NPR = 2.13
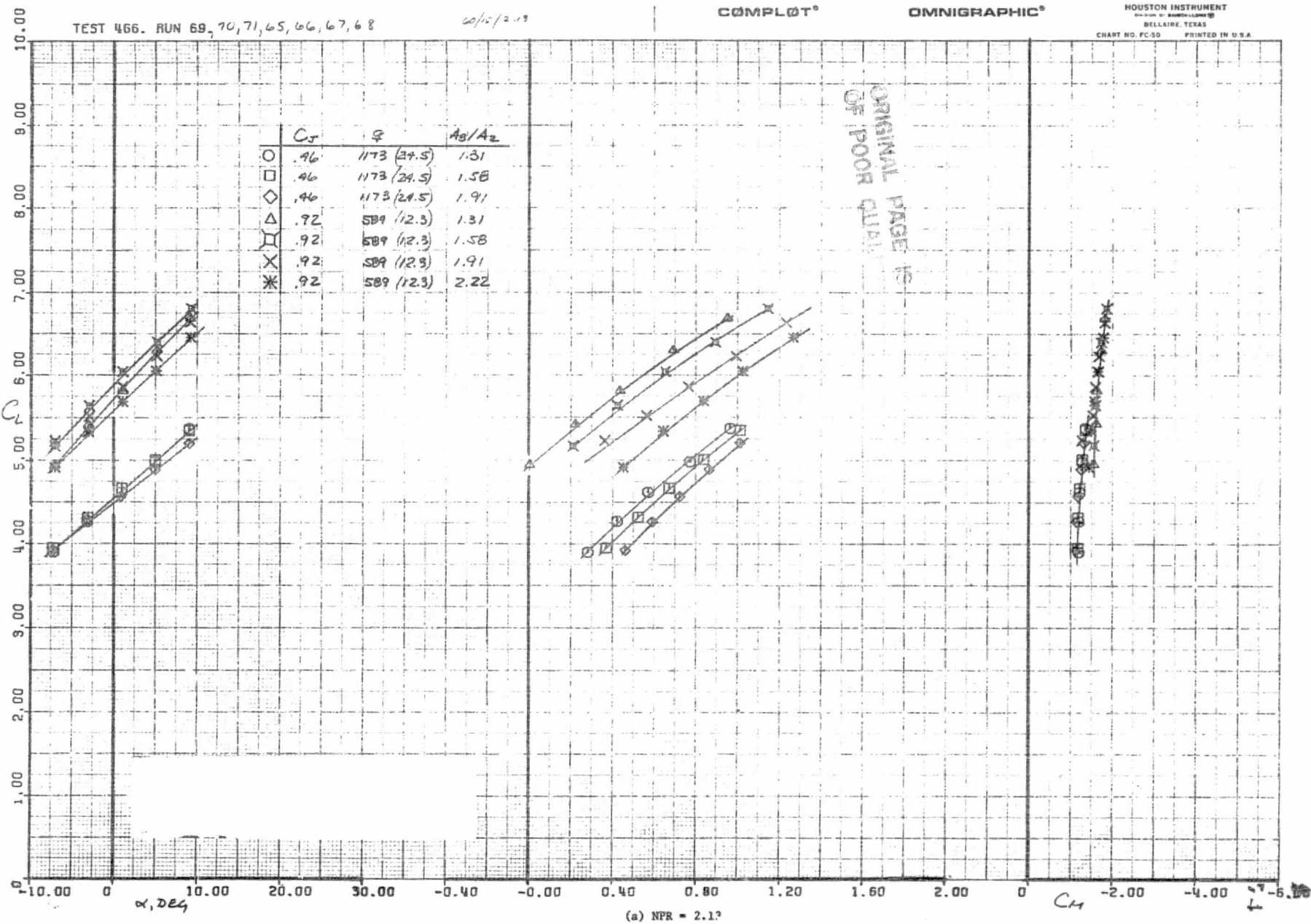
Figure 20.- The effect of C_J on the longitudinal characteristics of the model, $\delta_f = 60°$.

COMPLOT®   OMNIGRAPHIC®   HOUSTON INSTRUMENT
DIVISION OF BAUSCH & LOMB
BELLAIRE, TEXAS
CHART NO. FC-50   PRINTED IN U.S.A.

	C_J	q	
○	.22	1178	(24.6)
□	.31	814	(17)
◇	.47	546	(11.9)
△	.62	412	(8.6)
⬡	.93	273	(5.7)
✕	1.40	182	(3.8)
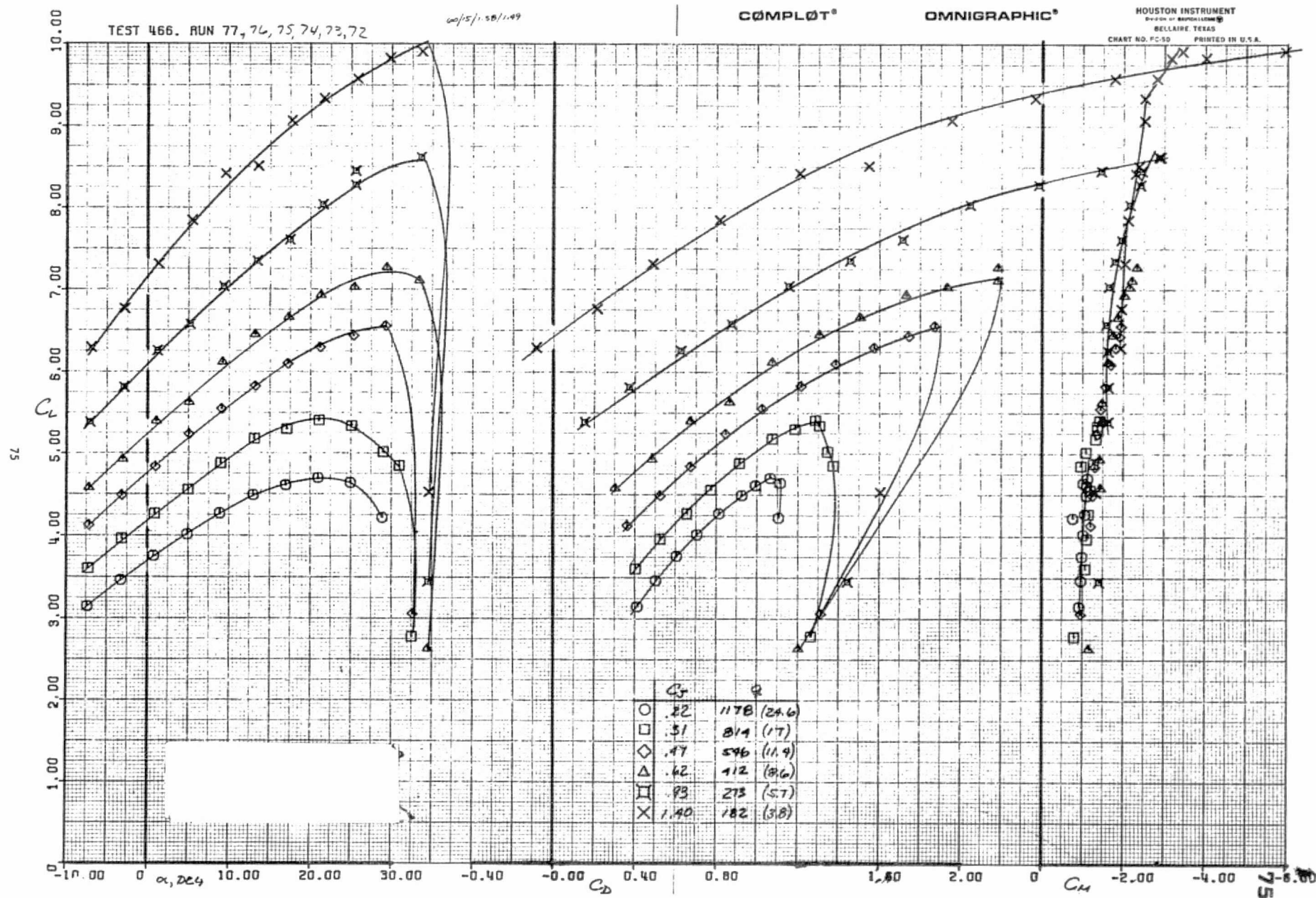
(b) NPR = 1.49, A_3/A_2 = 1.58.

Figure 20.- Concluded.

CØMPLØT® OMNIGRAPHIC®

HOUSTON INSTRUMENT
BELLAIRE, TEXAS
CHART NO. FC-50   PRINTED IN U.S.A.

	C_J	q		A_3/A_2
◯	.83	455	9.5	1.34
▢				1.64
◇				1.88
△				2.02
⊡	1.65	230	9.8	1.34
✕				1.64
✳				1.88
⋈				2.02
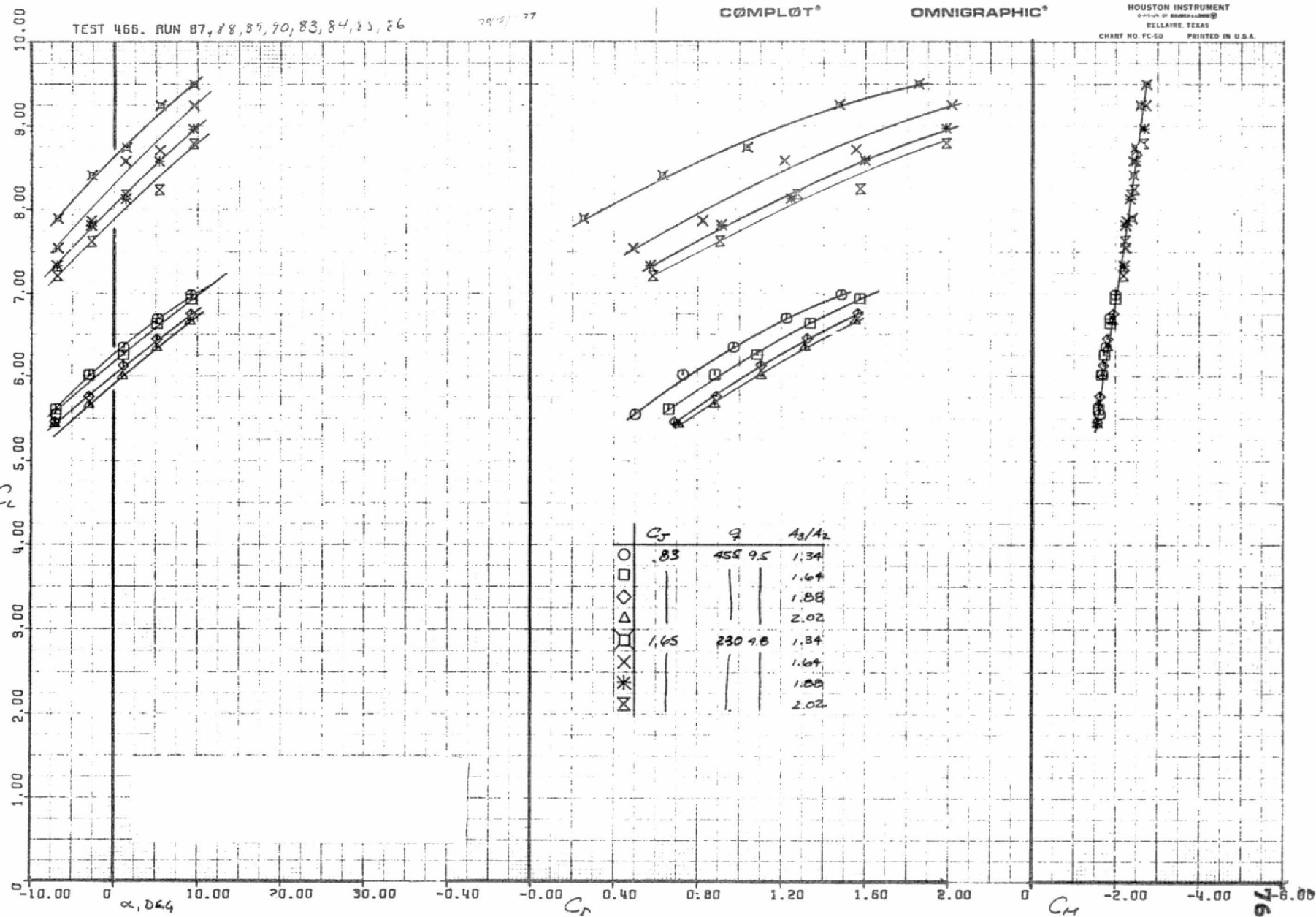
(a) NPR = 1.77.

Figure 21.- The effect of C_J on the longitudinal characteristics of
the model, $\delta_f = 70°$.

TEST 466. RUN 96, 95, 94, 93, 92, 91   70, 15 / 1.49 / 1.64   CØMPLØT®   OMNIGRAPHIC®   HOUSTON INSTRUMENT
DIVISION OF BAUSCH & LOMB
BELLAIRE, TEXAS
CHART NO. FC-50   PRINTED IN U.S.A.

	C_J	R	
O	.21	1178	(24.6)
□	.31	814	(17.0)
◇	.46	546	(11.4)
△	.61	412	(8.6)
⊞	.91	278	(5.8)
×	1.39	182	(3.8)
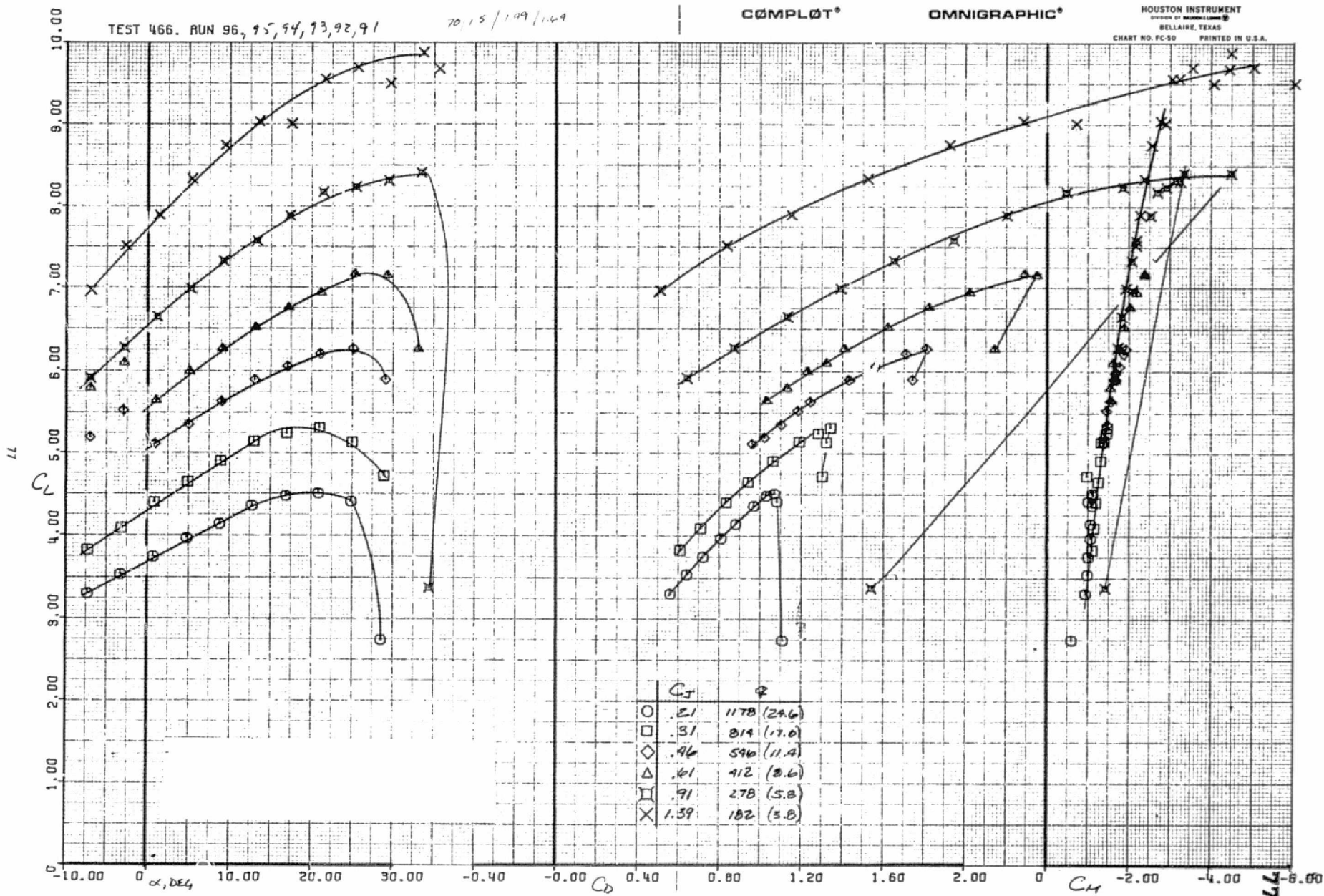
(b) NPR - 1.49, A_3/A_2 = 1.64.

Figure 21.- Concluded.

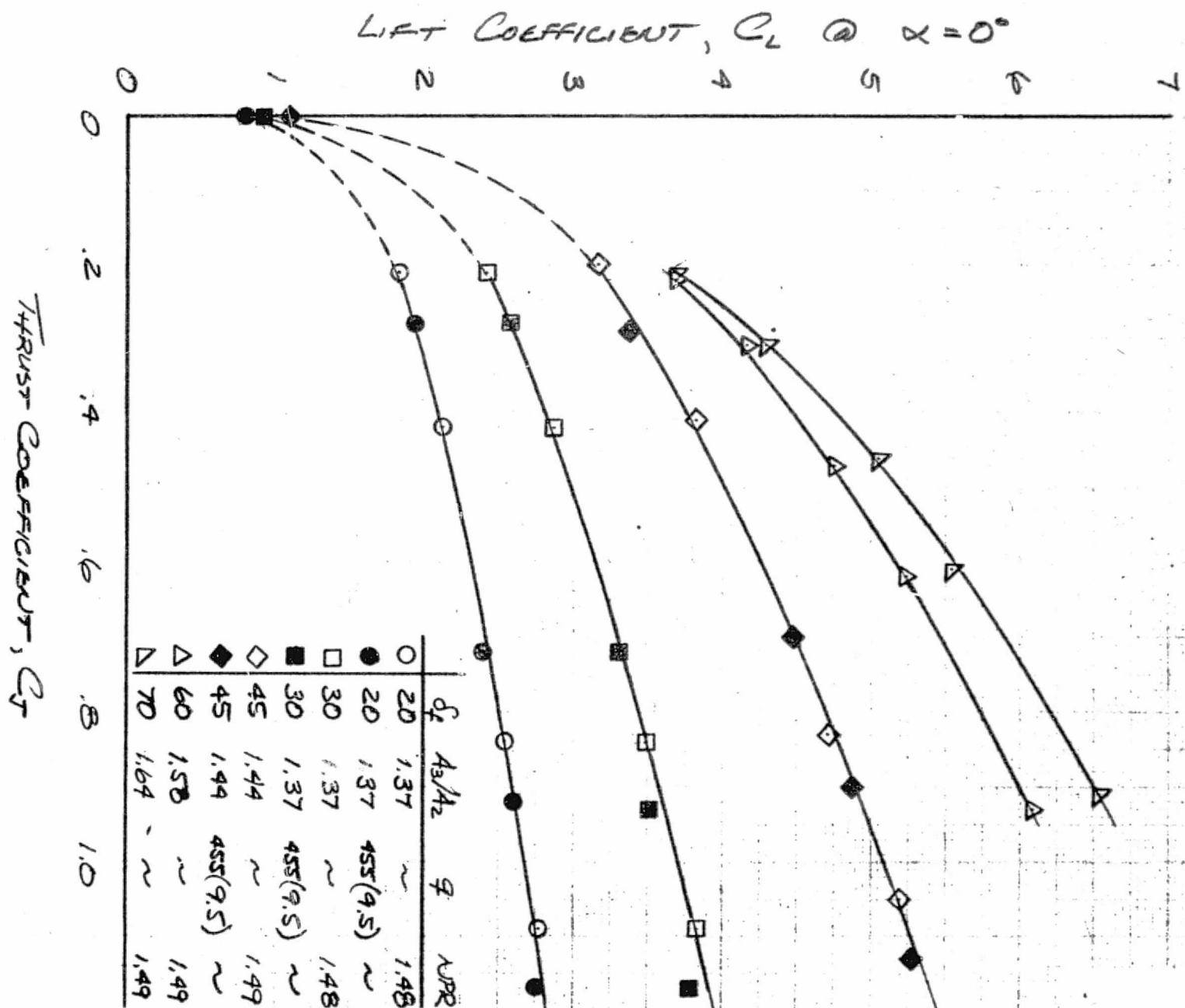|	δ_f	A_3/A_2	q	NPR
O	20	1.37	~	1.48
●	20	1.37	455(9.5)	~
□	30	1.37	~	1.48
■	30	1.37	455(9.5)	~
◇	45	1.44	~	1.49
◆	45	1.94	455(9.5)	~
△	60	1.58	~	1.49
▽	70	1.64	~	1.49

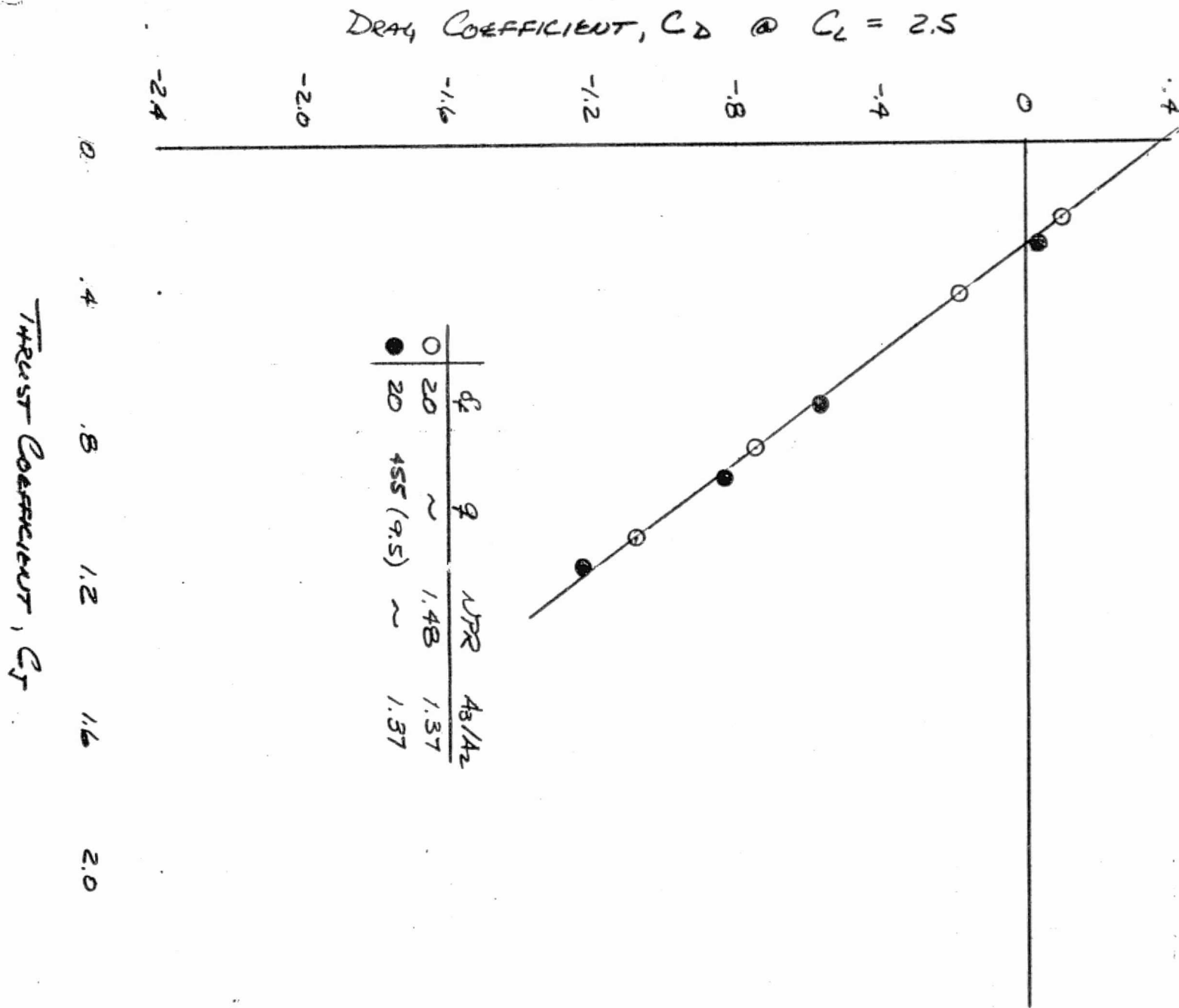Figure 22.- The effect of C_J and δ_f on the model lift at $\alpha = 0°$.

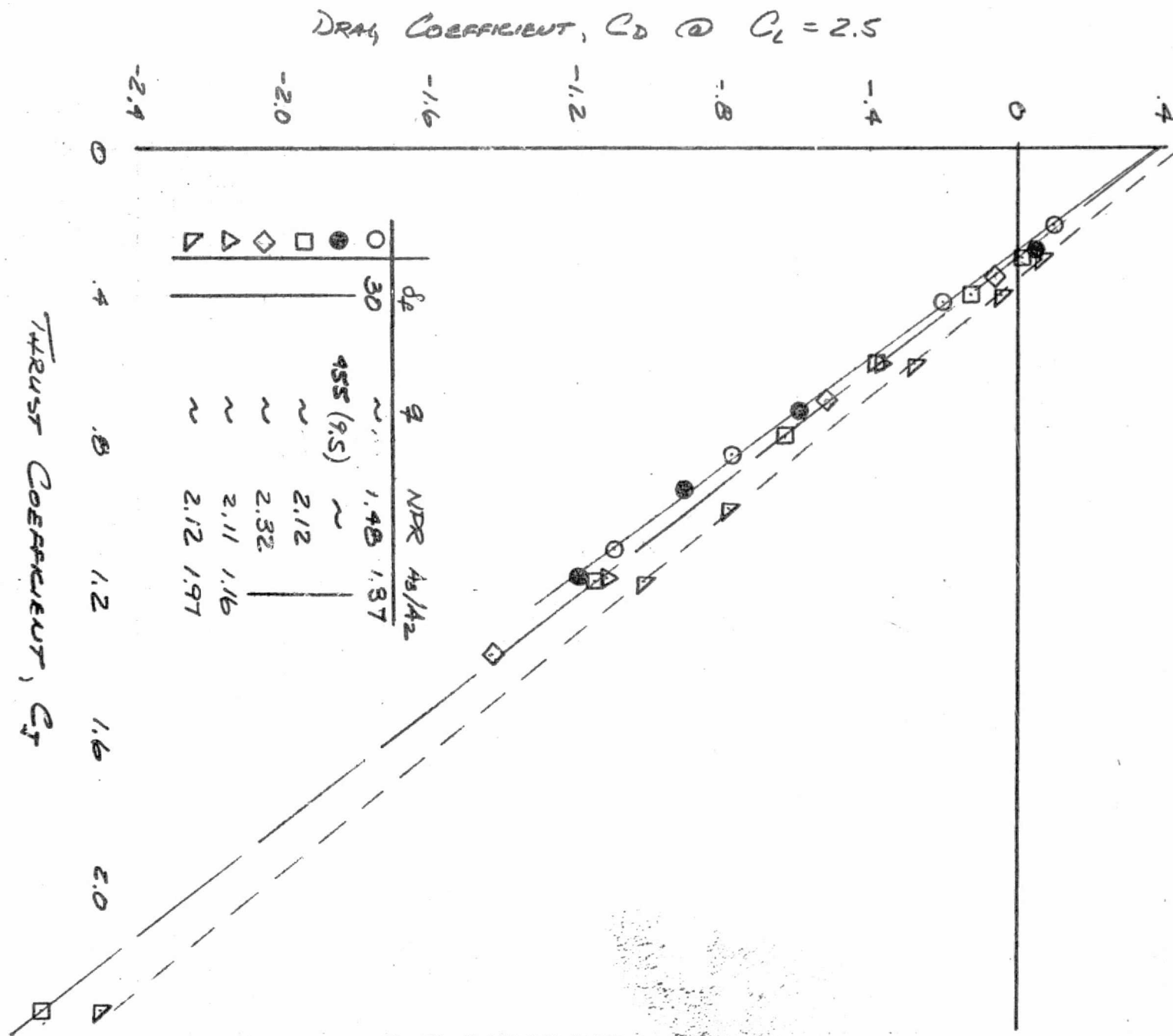Figure 23.- The effect of C_J on the model drag at C_L = 2.5, δ_f = 20°.

Figure 24.- The effect of C_J on the model drag at $C_L = 2.5$, $\delta_f = 30°$.

DRAG COEFFICIENT, C_D @ $C_L = 2.5$

THRUST COEFFICIENT, C_J

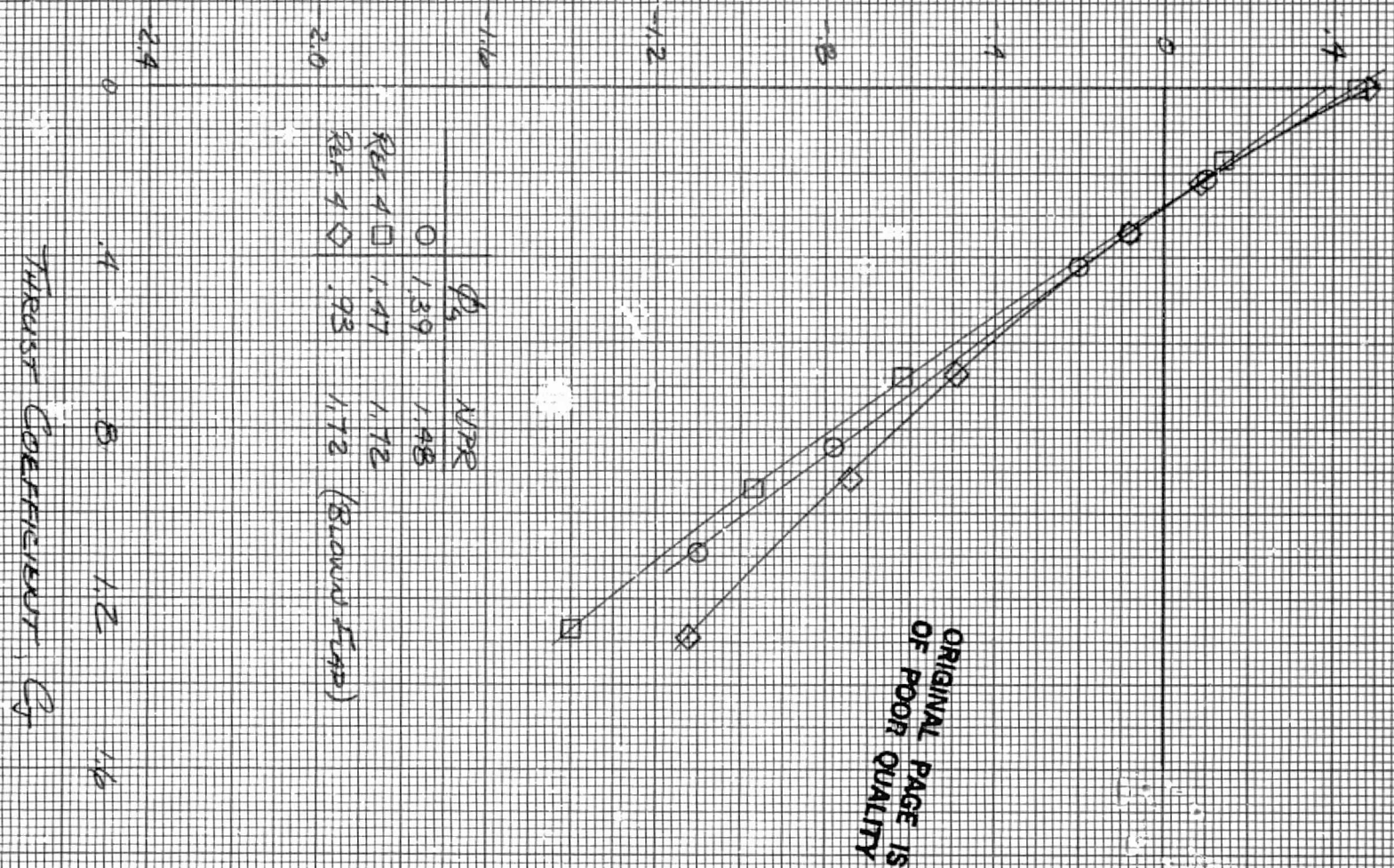|		C_J	NPR
Ref A	○	1.39	1.48
Ref A	□	1.47	1.72
Ref A	◇	.93	1.72 (Blown Flap)

81

Figure 25.- The effect of C_J on the model drag of several models,
$\delta_f = 30°$.